British
Geological Survey
NATURAL ENVIRONMENT RESEARCH COUNCIL

Petrography and stable isotope study of methane-derived authigenic carbonates (MDAC) from the Braemar Pockmark Area, North Sea

Mineralogy, Petrology and Microanalysis Facility Programme

Commissioned Report CR/13/078

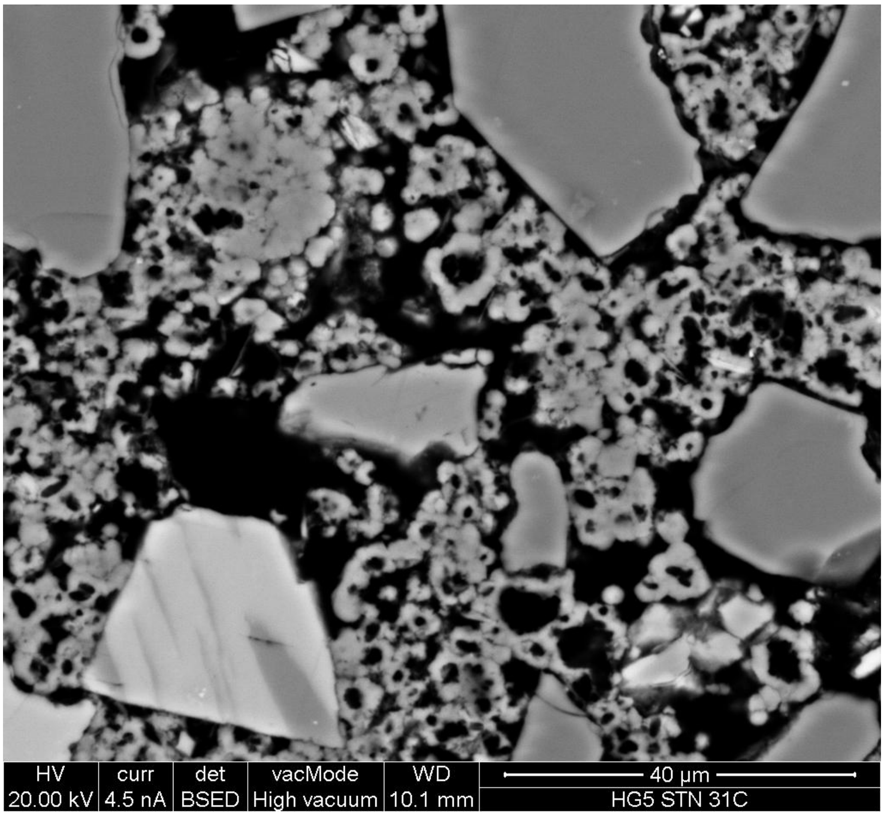

BRITISH GEOLOGICAL SURVEY

COMMISSIONED REPORT CR/13/078

Petrography and stable isotope study of methane-derived authigenic carbonates (MDAC) from the Braemar Pockmark Area, North Sea

A.E. Milodowski and H Sloane

Key words

MDAC, cold seep, methane oxidation, high-magnesian calcite, aragonite, dolomite, authigenic, Quaternary, Braemar, North Sea.

Front cover

BSEM image of microcellular fabric preserved within high-magnesium calcite forming intergranular cement between detrital quartz and K-feldspar sand grains in MDAC from site HG6 STN 31C in the Braemar Pockmark Area, North Sea.

Bibliographical reference

MILODOWSKI, A E AND SLOANE, H. 2013. Petrography and stable isotope study of methane-derived authigenic carbonates (MDAC) from the Braemar Pockmark Area, North Sea. *British Geological Survey Commissioned Report*, CR/13/078. 112pp.

Keyworth, Nottingham British Geological Survey 2013

BRITISH GEOLOGICAL SURVEY

The full range of our publications is available from BGS shops at Nottingham, Edinburgh, London and Cardiff (Welsh publications only) see contact details below or shop online at www.geologyshop.com

The London Information Office also maintains a reference collection of BGS publications, including maps, for consultation.

We publish an annual catalogue of our maps and other publications; this catalogue is available online or from any of the BGS shops.

The British Geological Survey carries out the geological survey of Great Britain and Northern Ireland (the latter as an agency service for the government of Northern Ireland), and of the surrounding continental shelf, as well as basic research projects. It also undertakes programmes of technical aid in geology in developing countries.

The British Geological Survey is a component body of the Natural Environment Research Council.

British Geological Survey offices

BGS Central Enquiries Desk
Tel 0115 936 3143 Fax 0115 936 3276
email enquiries@bgs.ac.uk

Kingsley Dunham Centre, Keyworth, Nottingham NG12 5GG
Tel 0115 936 3241 Fax 0115 936 3488
email sales@bgs.ac.uk

Murchison House, West Mains Road, Edinburgh EH9 3LA
Tel 0131 667 1000 Fax 0131 668 2683
email scotsales@bgs.ac.uk

London Information Office at the Natural History Museum (Earth Galleries), Exhibition Road, South Kensington, London SW7 2DE
Tel 020 7589 4090 Fax 020 7584 8270
Tel 020 7942 5344/45 email bgslondon@bgs.ac.uk

Columbus House, Greenmeadow Springs, Tongwynlais, Cardiff CF15 7NE
Tel 029 2052 1962 Fax 029 2052 1963

Maclean Building, Crowmarsh Gifford, Wallingford OX10 8BB
Tel 01491 838800 Fax 01491 692345

Geological Survey of Northern Ireland, Colby House, Stranmillis Court, Belfast BT9 5BF
Tel 028 9038 8462 Fax 028 9038 8461
www.bgs.ac.uk/gsni/

Parent Body

Natural Environment Research Council, Polaris House, North Star Avenue, Swindon SN2 1EU
Tel 01793 411500 Fax 01793 411501
www.nerc.ac.uk

Website www.bgs.ac.uk
Shop online at www.geologyshop.com

Foreword

This report is the published product of a study by the British Geological Survey (BGS) commissioned by Cefas under Cefas Purchase Order No. 20017984, and undertaken between 1 April 2013 and 31 July 2013. The purpose of the study was to undertake a petrographic and stable isotope investigation of samples of carbonate-cemented sediment recovered from the Braemar Pockmark Area of the North Sea, to evaluate their origin as possible methane-derived authigenic carbonate (MDAC) deposits. This report presents the results of the petrographic and stable isotope observations from the samples.

Acknowledgements

Dr David Long (BGS, Energy and Marine Geosciences Programme) is acknowledged for providing background information on the MDAC samples. Mr Daniel Parkes (BGS, Mineralogy and Petrology Facility) undertook the initial photography of the original MDAC samples. Mr John Fletcher (BGS, Thin Section Laboratory) is gratefully acknowledged for preparing the polished thin sections of the MDAC samples.

Contents

FIGURES

TABLES

Summary

This report describes the findings of a programme of work undertaken by the British Geological Survey (BGS) on behalf of the Centre for Environment, Fisheries & Aquaculture Science (Cefas) to characterise eleven samples of carbonate-cemented fine sandy and silty sediment, recovered by Cefas from the seabed in the Braemar Pockmark Area of the North Sea. The samples were collected from an area of active methane seeps, and the objective of this study was to characterise the origin and formation of carbonate-cemented sediment, and in particular to confirm whether or not the carbonate cementation is associated with the anaerobic oxidation of methane and sulphate reduction related to sub-seabed leakage of methane. The study will contribute to CEFAS's evaluation of the Braemar Pockmark as an area to be designated as an Offshore Special Area of Conservation (JNCC, 2008

Three end-member types of carbonate-cemented sediment have been differentiated using the mineralogy of their carbonate cements:

Aragonite-dominated cement, comprising: (i) early isopachous grain-coating aragonite fringes coating detrital grains; (ii) spheroidal aggregates of micritic or microcrystalline aragonite. These may coalesce to form a locally dense micritic 'crystal mush' matrix, and; (iii) coarse acicular aragonite overgrowths on molluscan shell fragments.

The aragonite is strontium-rich with up to 2 mole% $SrCO_3$ in solid-solution

The aragonite-cemented rock has been demonstrated to have formed later than the magnesian-calcite-cemented lithologies.

High-magnesium calcite-dominated cements, comprising: (i) early globular, spheroidal aggregates of very fine grained high-magnesium calcite coating detrital grains; (ii) "clots", or framboidal microbotryoidal aggregates of micritic or microcrystalline high-magnesium calcite. These micrite aggregates coalesce to form a locally dense micritic matrix; (iii) microcellular fabrics composed of magnesian calcite microcrystals that closely resemble fossilised and mineralised bacterial cells. Denser areas of cementation are formed as these microcellular structures coalesce and become more compacted.

The magnesian calcites typically have 10-35 mole% $MgCO_3$ in solid-solution.

Dolomite-dominated cements, comprising: (i) early grain-coating dolomite fringes formed of microcolloform globules; (ii) microcellular fabrics, comprising aggregates of dolomite similar to that observed in some of the magnesian-calcite-cemented samples and that closely resemble fossilised and mineralised bacterial cell.

The dolomite is a high-calcium dolomite which contains up to 10 mole% excess $CaCO_3$ relative to ideal stoichiometric dolomite.

Minor amounts of late-stage calcite replace both early micritic magnesian calcite and micritic dolomitic in some of the samples. This calcite is much lower in magnesium content than the original magnesian calcite that it replaces.

The recrystallisation of high-magnesian calcite and its partial replacement by lower magnesian calcite, is closely associated with minor late dolomite precipitation. The formation of this dolomite was probably promoted by the increased concentration of magnesium ions in the sediment porewater as a result of this replacement process, leading to localised minor dolomitisation of the carbonate sediment.

Petrographic observations also show that the micritic carbonate sediments were being reworked by benthic marine organisms, prior to lithification and then redeposited as sand-grade faecal pellets composed of micrite. Much of the evidence of burrowing preserved in these carbonate-cemented sediments was probably associated with this process. The petrographic evidence suggests that these micritic sediments were produced by and associated with abundant bacteria,

which probably provided the base of a food chain for larger, higher-order organisms prior to lithification of these sediments.

Stable isotope analyses show that the aragonite and magnesian calcite cements are highly depleted with respect to ^{13}C, with $\delta^{13}C_{PDB}$ values between -41 to -55 ‰. This is consistent with a diagenetic origin in which carbonate precipitation is related to methane oxidation, and is characteristic of MDAC deposits described previously from other areas. Therefore, this provides strong evidence to the hypothesis that the aragonite- and magnesian calcite-cemented sandstones and siltstones recovered from the Braemar Pockmark area of the North Sea represent MDAC.

In contrast, the dolomite cements (samples HG10 STN29A, HG10 STN29B and HG6 STN 31C) are characterised by $\delta^{13}C_{PDB}$ values between -33.0 and -18.0 $‰_{PDB}$, which are closer to that expected for carbonates produced during bacterial reduction processes. The dolomite cements in these samples are all very closely associated with the preservation of cellular fabrics that closely resemble mineralised bacterial structures, and with the syngenetic formation of early diagenetic framboidal pyrite. The formation of this micritic dolomite cement is therefore consistent with the early diagenetic dolomite precipitation within the sulphide-reduction zone close to the sediment surface, or with a significant input of carbonate/bicarbonate ions produced from bacterial sulphide reduction.

The observed $\delta^{18}O$ signature of the aragonite-cemented MDAC materials carbonate cements is broadly similar to the $\delta^{18}O$ of the aragonite cements predicted to be in equilibrium with seawater under present-day northern North Sea sea-bed temperatures (6 to 10 °C). Although some of the observed aragonite $\delta^{18}O$ values are slightly heavier than predicted, suggesting that they may have formed under slightly cooler conditions.

In contrast to the aragonite MDAC cements, the high-magnesium calcite MDAC cements are significantly heavier that that predicted to be in equilibrium with seawater at the present-day seabed (i.e. $\delta^{18}O$ is predicted to be between 1.4 to 2.4 $‰_{PDB}$ for calcite). Even allowing an increase in $\delta^{18}O$ for high magnesium calcite, these data suggest that carbonate cements have precipitated under significantly colder conditions than present-day (calculations suggest approximately 3 to 10°C colder), or from seawater with a significantly heavier $\delta^{18}O$ than SMOW. Both colder marine temperatures and ^{18}O-enriched marine water in the North Sea during the last glacial maximum could therefore have produced the heavy $\delta^{18}O$ observed in the magnesian calcite cements (and to a lesser extent, the aragonite cements) in these MDAC samples from the Braemar Pockmark area.

The more complex MDAC samples represented by HG2 STN 46B and HG2 STN 46C, in which magnesian-calcite cemented MDAC is superseded by aragonite –cemented MDAC indicates that in the area where these samples formed, there have been at least two distinct phases of MDAC formation: an earlier phase during cooler conditions (possibly during the last glacial maximum) when high-magnesian calcite was precipitated; and a later phase of MDAC formation under warmer conditions closer to present-day marine temperatures, when aragonite was precipitated.

The dolomitic carbonate cements are similarly heavier than expected with regard to $\delta^{18}O$ for precipitates from present day seawater. These too could have been formed during cooler marine temperatures than the present-day. However, the lighter $\delta^{13}C$ values suggests that these formed with a significant input of carbonate derived from the bacterial iron and sulphate reduction in the sediment, rather than dominantly from bacterial methane oxidation.

Virtually all of the carbonate-cemented sediment samples examined in this study display abraded and well-worn and rounded surfaces. This indicates that most of the pebble- to cobble-sized fragments are clasts of re-worked carbonate-cemented sediment that have eroded from their original sediment source. Therefore, they do represent in situ carbonate-cemented rocks. Observations show that the clasts have also been exposed to oxidising conditions on the sea floor during this process.

1 Introduction

1.1 GENERAL

The British Geological Survey (BGS) has been contracted by the Centre for Environment, Fisheries & Aquaculture Science (Cefas) to undertake a petrological and geochemical study of a suite of 11 samples of diagenetic, carbonate-cemented sediment ‘clasts’ recovered by Cefas from the Braemar Pockmark Area of the North Sea. The samples were collected from an area of active methane seeps (Hovland and Sommerville, 1985; Dando et al., 1991; Judd et al., 1994). The objective of this study is to characterise the origin and formation of carbonate-cemented sediment, and in particular to confirm whether or not the carbonate cementation is associated with the anaerobic oxidation of methane and sulphate reduction related to sub-seabed leakage of methane (cf. Jorgensen, 1992 and Judd, 2001). The study will contribute to CEFAS’s evaluation of the Braemar Pockmark as an area to be designated as an Offshore Special Area of Conservation (JNCC, 2008).

Methane seepages from the seabed of the North Sea may be give rise to increased local benthic production, with a richer fauna, as a result of the development of a bacteria-based food web (Hovland and Judd, 1988; Dando et al., 1991; Dando, 2001). The sediments in the Braemar Pockmark area are therefore considered to be of potentially important ecological significance, and there is a requirement to adequately document and characterise these features in order to develop appropriate conservation management plans for such habits in UK offshore waters. The structures consist of carbonate-cemented sediments that are believed to have a Methane-Derived Authigenic Carbonate (MDAC) origin.

1.2 SITE LOCATION AND GEOLOGICAL BACKGROUND

Pockmarks on seabed are common on the thick sediment deposits in the central part of the northern North Sea (Jansen 1976; Long 1986; Dando et al., 1991). They are believed to have been formed by the rapid expulsion of over-pressured fluid through the seabed, which displaced the fine muddy sediment to form characteristic craters and depressions (Judd et al., 1994; Hovland and Judd, 1988; Hovland and Talbot 1987; Dando et al., 1991; Judd, 2001). The escaping fluid may be a submarine release of groundwater from aquifer formations but in the majority of cases it is believed to be largely the release of methane gas that is responsible for the formation of these features. The gas may originate from the microbial decomposition of organic matter within the near-seabed sediments (fermentation zone) – referred to as ‘microbial’, ‘biogenic’ or ‘bacterial’ gas (Judd, 2001), from the dissociation of methane hydrates (e.g. Solheim and Elverhøi, 1993, referred to by Dando 2001), or by release of gas produced by the thermocatalytic destruction of kerogens deep within the sediments or shallow hydrocarbon reservoirs ('thermogenic' gas). Typically, the gas is primarily composed of methane (CH_4).

One such area of pockmarks occurs in the Braemar Field in U.K. Licence Block 16/03, the location of which is shown in Figure 1. It is situated about 240 km east of the Orkney Islands and 185 km off the northeast coast of Scotland (latitude N58°59'12" longitude E1°28'34") and the site has an area of 5.18 km^2 (JNCC, 2012). The general characteristics of the Braemar Pockmark are similar to those of the Scanner Pockmark about 80 km to the southwest but the carbonate structures in the Braemar site are more abundant and diverse in form compared to the Scanner site (JNCC, 2012). The pockmarks are shallow, ovoid, seabed depression, several meters wide, lying in a depth of approximately 120 m of water. The site is associated with methane leaking through the seabed, and the habitat created supports chemosynthetic organisms that feed off the bubbling methane gas.

The regional Quaternary geological succession has been described by Sjejrup et al. (1991) and Johnson et al., (1993), and is broadly similar to that encountered at the Scanner Pockmark site, which have been described in detail by Hovland and Somerville (1985), Long (1986), Dando et al. (1991), Judd et al. (1994), Dando (2001), Judd (2001) and JNCC (2008). The seabed surface sediments typically comprise a thick sequence of very soft multi-layered grey to greyish-brown clays and silts, with horizons of sandy sediments and rare small pebbles, representing glaciomarine deposits of late Weichselian to Holocene age. These overly Pleistocene sediments comprising: stiff, dark grey clays and silts of the reworked proximal glaciomarine deposits; and firm to hard dark grey to brownish-grey, muddy, pebbly sands or sandy muds (with rare shell fragments) deposited during the glacial-interglacial-glacial cycle from the Saalian to the Weichselian. These Pleistocene strata were subjected to ice-loading during the late Weichselian (Devensian) glaciation. As for the Scanner Pockmark site, the stress relief, reduction of sediment volume, and associated melting of ground ice during glacial retreat and unloading, is believed to have created instability, leading to the rapid release of the gas trapped and accumulated in permeable sediments beneath low-permeability layers in the underlying sediments resulting in the formation of pockmarks.

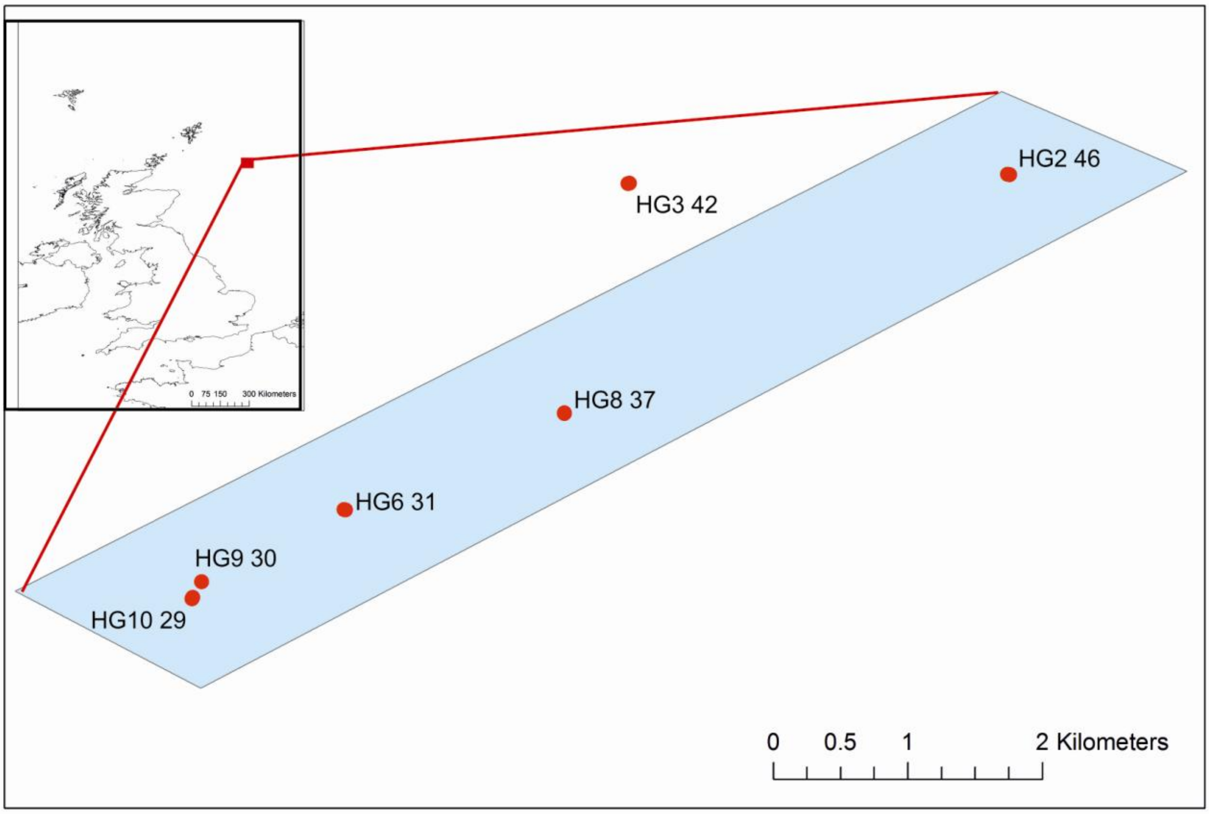

Figure 1. Location map of the Braemar Pockmark Offshore Special Area of Conservation Area in the northern North Sea (data provided by Cefas).

Active gas seepage occurs within the Braemar Pockmark at the present day. The Jurassic Kimmeridge Clay is the principal hydrocarbon source rock for several producing oil and gas fields in this area of the North Sea, and together with deeper Carboniferous coals could potentially provide a deep source of thermogenic methane within the region. In the case of the Scanner Pockmark, no methane accumulation was encountered in hydrocarbon exploration wells drilled nearby, suggesting that these rocks are not the source of methane in the Scanner Pockmark (Judd et al., 1994). The most likely source of methane for the Scanner Pockmark is thought be derived from the biogenic decomposition of lignite within the shallow Tertiary

Hordaland and Nordland Group strata underlying the area (Judd et al., 1994). This conclusion is supported by evidence from seismic profiles for gas accumulations in these strata (Andrews et al., 1990), together with the very light carbon isotope signature (-70 ‰$_{\mathrm{PDB}}$) of discharging methane samples collected from the Scanner Pockmark (Hovland and Irwin, 1989, cited by Judd et al., 1994) that indicates a bacterial (biogenic) methane source (Burke, 1992; Judd et al., 1994 Judd, 2001).

1.3 SAMPLES

Background details of the 11 samples of potential MDAC material from the Braemar Pockmark submitted provided by Cefas to the BGS for petrological and stable isotope analysis are summarised in Table 1). The samples were collected during the Braemar 2012 cruise. Each sample provided consisted of several “clasts” or “fragments” of carbonate cemented sediment. They were photographed and a visually-representative “clast” from each of the samples was subsequently selected for analysis. The mineralogical, petrographical and stable (oxygen and carbon) isotope characteristics of these samples are presented in this report.

Table 1. List of MDAC samples submitted for petrological and C and O stable isotope analysis

Sample number	Cruise	Description
HG2 STN 46B	Braemar 2012	Olive-grey and mid-grey, irregular, lenticular, abraded fragments of carbonate-cemented siltstone and fine sandstone, and tubular carbonate-cemented burrow fills in fine sandstone and siltstone, locally deeply bored or with calcareous serpulid / worm encrustations. Patchy iron oxyhydroxide-stained surfaces.
HG2 STN 46C	Braemar 2012	Olive-grey and dark-grey, irregular, lenticular, abraded fragments of carbonate-cemented siltstone and fine sandstone, and tubular carbonate-cemented burrow fills in fine sandstone and siltstone, locally bored or encrusted with calcareous serpulids. Patchy iron oxyhydroxide-stained surfaces.
HG3 STN 42B	Braemar 2012	Dark-grey, irregular and sub-equant fragments of carbonate-cemented siltstone and very fine sandstone. Generally highly abraded and well-rounded, with abundant surface borings.
HG3 STN 42C	Braemar 2012	Dark-grey, and light grey to cream-coloured, very fine sandstone and siltstone clasts. Well rounded and abraded with a few surface borings. Iron oxyhydroxide stained surfaces on some clasts and boring walls.
HG6 STN 31C	Braemar 2012	Pale buff-grey, with pale orange-brown stained surface. Irregular lenticular, platy and elongate tubular fragments of carbonate cemented siltstone to fine sandstone. Common deep surface borings.
HG8 STN 31B	Braemar 2012	Dark grey to olive-grey, irregular, elongate and platy, sub-rounded to moderately well-rounded and abraded fragments dominated by carbonate-cemented siltstone. |Some iron oxyhydroxide-stained surfaces. Locally bored.
HG8 STN 37B	Braemar 2012	Dark grey to olive-grey, irregular, elongate and platy, sub-rounded to moderately well-rounded and abraded fragments dominated by carbonate-cemented siltstone. Some strongly-stained, light-grey fragments permeated by buff-coloured iron oxyhydroxide staining.
HG8 STN 37C	Braemar 2012	Dark grey to olive-grey, irregular, elongate and platy, sub-rounded to moderately well-rounded and abraded fragments dominated by carbonate-cemented siltstone.
HG9 STN 30A	Braemar 2012	Irregular, lenticular, abraded and sub-rounded fragments of carbonate-cemented siltstone and fine sandstone, and tubular carbonate-cemented burrow fills in fine sandstone and siltstone, with surface borings. Some surfaces stained by pale buff-brown iron oxyhydroxide staining.
HG10 STN 29A	Braemar 2012	Dark grey, olive-grey and light-grey irregular, lenticular, abraded and sub-rounded fragments of carbonate-cemented sandstone and siltstone, with deep surface borings. Locally patchily-stained by iron oxyhydroxides.
HG10 STN 29B	Braemar 2012	Irregular fragments of mid- to dark-grey carbonate-cemented siltstone and fine sandstone. Abundant surface borings, angular and well-rounded abraded fragments. Locally patchily- to strongly-stained by pale orange-buff iron oxyhydroxides. Some borings stained by iron oxyhydroxide films.

2 Analytical methods

2.1 PETROGRAPHICAL ANALYSIS

2.1.1 Polished block section preparation

It was originally intended to prepare both 30 µm thick, epoxy-resin impregnated, polished thin sections for detailed petrographical analysis, and separate polished blocks for micro-drilling for stable isotope sub-sampling and analysis (cf. approach used previously by Milodowski et al., 2009). The polished blocks would have been prepared from the counterpart off-cuts of material used in preparation of the polished thin sections. However, on receipt of the samples it was observed that most of the samples were very fine grained micritic carbonate and siltstone. Consequently, a greater advantage was to be had in carrying out petrographical analysis directly on the polished blocks in order to be able to more carefully constrain subsequent sub-sampling of well-characterised material for stable isotope analysis of the carbonate mineral cements. Therefore, polished thin sections were not prepared and both petrographical characterisation and subsequent stable isotope micro-sampling were carried out directly on the polished block specimens.

Polished block sections for petrographical analysis were prepared from small blocks, between 20 to 35 mm in diameter that were sawn from the MDAC samples. The blocks were impregnated with epoxy-resin under vacuum in order to stabilise the material for polished section preparation. These resin-impregnated blocks were then sliced and polished to produce polished blocks approximately 8 mm thick. The polished blocks were finished by polishing with 0.45 µm diamond paste. These blocks were used for detailed petrographical analysis by backscattered scanning electron microscopy (BSEM) and subsequently, for micro-sampling by micro-drilling, for stable isotope analysis as described in Section 2.2.

2.1.2 Optical microscopy

The polished blocks were initially scanned, using a digital flatbed optical scanner, to provide reference images of the whole block section area. The polished blocks were then briefly examined in reflected light using a Zeiss Axioplan 2 petrological (polarising) microscope.

2.1.3 Cathodoluminescence microscopy

The polished blocks were examined by cathodoluminescence (CL) microscopy in order to differentiate different types and generations of carbonate cement, and the location of bioclastic carbonate detritus, on the basis of variations in luminescence characteristics. Mineralogical variations and subtle differences in minor and trace element chemistry within carbonate minerals can produce significant differences in luminescence characteristics when the mineral is irradiated with electrons (Marshall, 1988). In particular, this luminescence microscopy technique is very sensitive to small variations in iron (Fe^{2+}) and manganese (Mn^{2+}) content within calcite and dolomite, and is able to differentiate growth zoning and different mineral generations within these carbonate mineral cements.

CL analysis was performed using a Technosyn Model 8200 Mark II cold-cathode cathodoluminoscope stage mounted on a Nikon transmitted optical microscope, fitted with long working distance objective lenses. Images were captured using a bespoke Zeiss AxioCam MRc5 digital microscope camera.

2.1.4 Scanning electron microscopy and electron probe microanalysis

Backscattered scanning electron microscopy (BSEM) was used to make high-resolution petrographical observations of the polished sections. Image brightness in BSEM images is related to the average atomic number of the phases observed (Goldstein et al., 1981), and this therefore allows differentiation of the minerals observed in polished sections on the basis of the image brightness. Prior to BSEM examination, the polished surface of the section was made electrically conductive by coating with a thin layer of carbon (250Å thick) by vacuum evaporation of carbon.

BSEM analyses were carried out using a FEI QUANTA 600 environmental scanning electron microscope (ESEM) fitted with an Oxford Instruments INCA Energy 450 energy-dispersive X-ray microanalysis (EDXA) system with a 50 mm^2 Peltier-cooled (liquid nitrogen free) silicon drift detector (SSD) X-ray detector capable of operating at very high input X-ray count rates (up to ~10^6 counts per second). The ESEM was operated in conventional high vacuum mode, with a routine electron beam accelerating voltage of 20 kV which was reduced to between 10-20 kV where finer resolution was required, and beam probe currents of between 1.17 and 4.5 nA, and a working distance of 7-10 mm. Mineral/phase identification was aided by microchemical information obtained from simultaneous observation of semi-quantitative EDXA spectra recorded from features of interest.

Quantitative electron probe microanalysis (EPMA) of the carbonate cements observed in polished thin section was also undertaken by BSEM-EDXA. Quantitative EDXA electron probe microanalyses were performed using a 20 kV electron beam, nominal 4.5 nA beam current at an optimised working distance of 10 mm, to give a X-ray counting live-times of 30 seconds with dead-times of between 30 to 45%. EDXA data were acquired, processed and interpreted using the Oxford Energy INCA Suite Version 4.15 Issue 18d+SP3 (2009) software package. The EDXA system is capable of detecting elements from atomic number 4 (boron) to atomic number 92 (uranium), and has detection limits of the order of 0.2 to 0.5 wt. % for most common major elements.

Most of the carbonate cement fabrics observed were highly microporous, with the result that the electron probe volume included significant void space, resulting in low analytical totals. Furthermore, the carbonate cements were intimately admixed with, abundant fine grained detrital silicate clay mineral, quartz, feldspar and mica sediment particles, and occasionally authigenic pyrite. Consequently, many of the EPMA data obtained include a contribution from the entrained detrital silicate grains that could not be completely resolved from the carbonate mineral matrix by EPMA. However, most of the silicate mineral impurities contribute mainly Si, Al, K, Na, and occasionally Fe and S is contributed from pyrite. The EPMA data for Mg, Ca, Sr and Fe (where S was not present) are attributed here completely to the carbonate mineral chemistry. The carbonate mineral chemistry was therefore determined after calculating the theoretical carbonate (CO_3^{2-}) ion concentration by summation of the equivalent carbonate component associated with each metal cation, i.e.

$$Total\ CO_3^{2-} = \Sigma\ [equivalent\ CO_3^{2-}\ from\ Ca^{2+} + Mg^{2+} + Mn^{2+} + Fe^{2+} + Sr^{2+}]$$

The data were then normalised to 100 wt %, and the mineral stoichiometric structural formula calculated by determining the molar ratios of each cation component.

2.2 STABLE ISOTOPE ANALYSIS

Fifty-five sub-samples of MDAC were analysed to determine oxygen and carbon stable isotope ($\delta^{18}O$ and $\delta^{13}C$) composition of the carbonate components. The areas for micro-sampling were identified from optical scanning and BSEM images carried out previously on the resin impregnated polished blocks. This methodology has been very successfully used in previous studies to sample and analyse discrete generations of carbonate mineralisation in intergrown polymineralic or multi-generation carbonate cements (Milodowski et al., 2005).

Micro-sampling was undertaken using a tungsten-carbide micro-drill, whilst observing the block sample in reflected light under an optical microscope. The micro-drill was capable of drilling and recovering material from areas as small as ~0.1 mm. However, in order to obtain sufficient material for stable isotope analysis areas up to 3 mm diameter were drilled. In general, 5 subsamples were drilled for isotopic analysis from each of the 11 polished blocks prepared from the MDAC samples. The exceptions for this were for sample HG8 STN 37C where 4 subsamples were prepared, and sample HG8 STN 37B where 6 subsamples were prepared.

2.2.1 Small carbonate sample analysis method

All 55 subsamples were analysed for $\delta^{18}O$ and $\delta^{13}C$ using the 'small carbonate analysis method' using a fully-automated analytical system. 100-200 µg of micro-drilled powdered carbonate sample were placed in reaction vials on-line in an Isoprime gas-source mass spectrometer analysis system. The reaction vials were evacuated to remove atmospheric CO_2 and moisture, and phosphoric acid was then delivered to the vessels. The reaction between phosphoric acid and the carbonate mineral was carried out at 90 °C, and the resultant CO_2 produced was continuously collected by condensation using liquid nitrogen for the reaction time of 15 minutes and then delivered to the Isoprime gas-source mass spectrometer for analysis.

The resultant gas values were corrected using Craig's correction to adjust for small levels of the ^{17}O isotope, and reported with respect to the accepted Vienna Pee Dee Belemnite (vPDB) scale (McCrea, 1950; Rosenbaum and Shepherd, 1986). A further normalisation through the primary standard is also applied. These values were then corrected to the solid carbonate mineral using the appropriate fractionation factors for the different carbonate minerals at a temperature of 90 °C: for calcite a fractionation factor of 1.00798 was used; and for dolomite a fractional factor of 1.0087 was used. For aragonite the same fractionation factor as for calcite was used since it is similar to that of calcite within experimental error.

2.2.2 Classical carbonate analysis method

Because the Isoprime 'small carbonate sample' analysis method is designed primarily for the analysis of calcite and aragonite samples, a subset of dolomite samples were also analysed using the classical analysis method, to provide a cross-check on the reliability of the small carbonate analysis method for dolomite.

Between 6-10 mg of sample was loaded into sample reaction tubes and placed in reaction vessel containing 4-6 ml of anhydrous phosphoric acid. The vessels were then evacuated to $>1.0^{-4}$ mb to remove atmospheric carbon dioxide and moisture. The reaction vessels are then sealed and placed in a controlled temperature water bath at 55 °C and allowed to thermally equilibrate for approximately 30 minutes. Reaction with the phosphoric acid was carried out by introducing the acid into sample reaction tubes within the sealed, evacuated vessel. The vessels are intermittently agitated to maintain continuation of the reaction, and then left for 16 hours to ensure reaction has gone to completion.

The gas was cleaned up cryogenically by expanding it through an dry ice/acetone cold trap maintained at 90°C, and collected in clean dry collection vessels using liquid nitrogen. The vessels were then sealed and transferred to an Thermo MATT253 dual inlet gas source mass spectrometer for analysis.

The resultant gas values were corrected using Craig's correction to adjust for small levels of the ^{17}O isotope, and reported with respect to the accepted vPDB scale. A further normalisation through the primary standard was also applied. These values are then corrected to solid carbonate values using fractionation factor as described above (see Section 2.2.1).

3 Mineralogy and petrography

3.1 SAMPLE HG2 STN 46B

Sample HG2 STN 46B comprised a series of fragments of dark grey to light brownish grey carbonate-cemented fine sandstone and siltstone ranging in size from <10 mm to 120 mm diameter. The fragments are typically irregular in form, varying from rough plates to subrounded and sub-angular elongate forms that appear to be cemented burrow fills (Figure 2). Many of the fragments appeared to be abraded and rounded but the ends of the more elongate “cemented burrow-like” forms were commonly angular. The surfaces of the fragments commonly bored by marine organisms and several clasts were seen to be encrusted by white calcareous tubes secreted by serpulid worms(tube-worms).

Figure 2. Photograph showing the range of shapes and sizes of the fragments of carbonate cemented sandstone siltstone in sample HG2 STN 46B.

Sample HG2 STN 46B and HG2 STN 46C have the most complex mineralogy and fabric of all of the MDAC samples examined, with multiple generations of carbonate cement. The polished section prepared through a fragment of HG2 STN 46B is shown in Figure 3. It shows a lower layer of dark-grey carbonate cemented sediment separated by an irregular abraded and eroded surface, from an upper horizon of lighter grey carbonate sediment. The erosion surface is also penetrated by a large sub-vertical boring which passed downwards into a large and irregular chamber, and the boring and chamber are partially-filled by carbonate-cemented sand and silt. The upper carbonate-cemented horizon is also affected by borings. The erosion surface and the walls of the borings are stained by very finely-disseminated iron oxyhydroxide, indicating oxidation was associated with the erosion and burrowing activity.

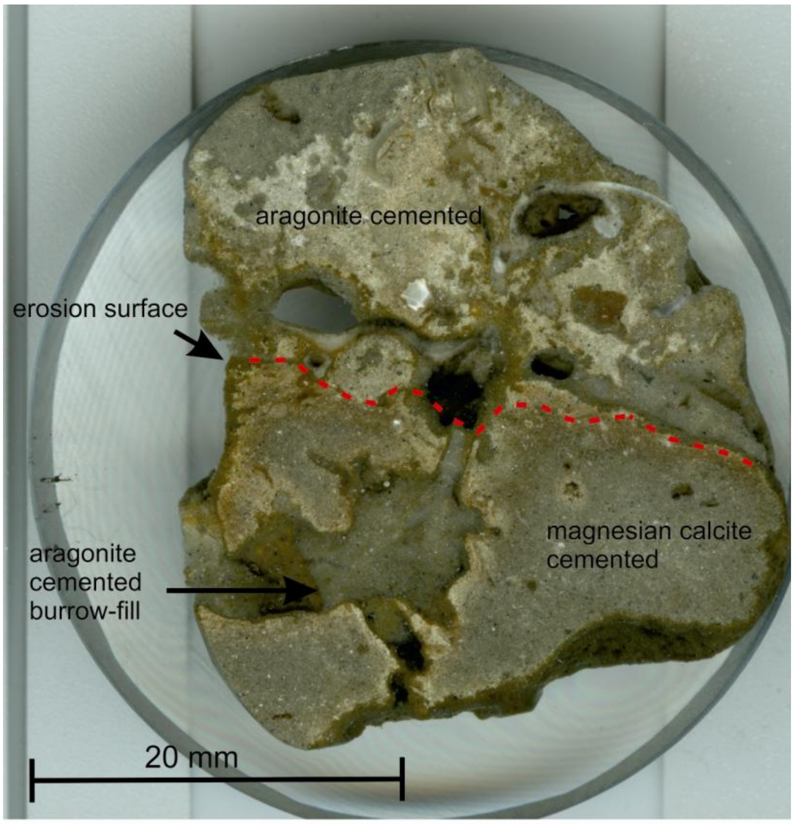

Figure 3. Polished section through a fragment of carbonate-cemented siltstone and sandstone. It shows grey aragonite-cemented siltstone-fine sandstone resting on an eroded surface of darker grey magnesian calcite-cemented siltstone-fine sandstone. Aragonite-cemented siltstone-fine sandstone fills burrows in the underlying magnesian calcite-cemented siltstone-fine sandstone. The erosion surface and the margins of the burrow walls are stained by orange-brown secondary iron oxyhydroxide. Sample HG2 STN 46B.

In thin section both carbonate-cemented horizons were seen to comprise moderately- to well-sorted very fine sandstone to siltstone, dominated by angular grains of detrital quartz (Figure 4 and Figure 5). Detrital K-feldspar, albite and muscovite are present in minor to trace amounts, and apatite, zircon, ilmenite and magnetite are also present as trace detrital components. Eroded fragments of aragonitic bivalve shells and foraminiferal tests, and large, well-rounded pelloidal carbonate grains (probably faecal pellets) are common in the upper carbonate-cemented sandstone layer. The shell fragments are commonly ‘riddled’ by fine borings typically ~10 µm in diameter and up to 200 um deep (see Figure 7). Both carbonate layers have an ‘open’, ‘expanded’ or uncompacted grain fabric, in which the detrital grains ‘float’ in a matrix of fine-grained carbonate cement, with relatively few simple point and long grain-to-grain contacts (Figure 4 and Figure 5). This indicates that the carbonate cementation occurred at, or close to, the surface of the sea bed and before any significant burial compaction, and the carbonate cements may in part have grown displacively in the sediment forcing the sand grains apart. Several of the detrital quartz grains display etching and corrosion by the carbonate cements (e.g. Figure 5, Figure 6 and Figure 7). BSEM-EDXA revealed that the lower layer is cemented by magnesian calcite but the upper layer is cemented by aragonite.

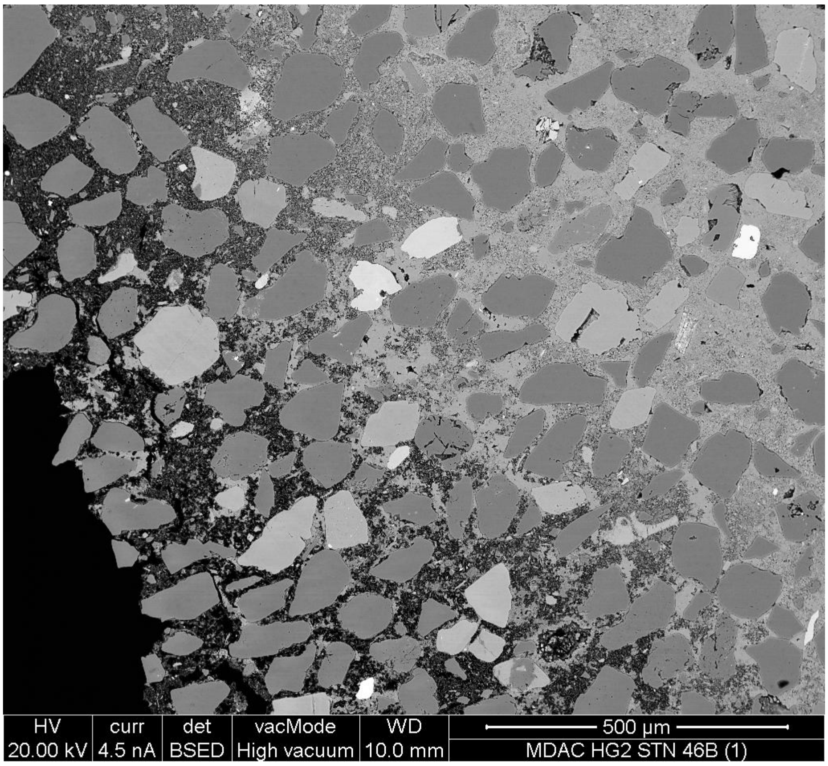

Figure 4. BSEM photomicrograph showing an uncompacted grain fabric in the lower, magnesian calcite-cemented sandstone (mid grey), with detrital grains of quartz (dark grey) and minor K-feldspar (light grey). The bottom left hand edge shows the weakly-cemented margin of a large burrow feature. Sample HG2 STN 46B.

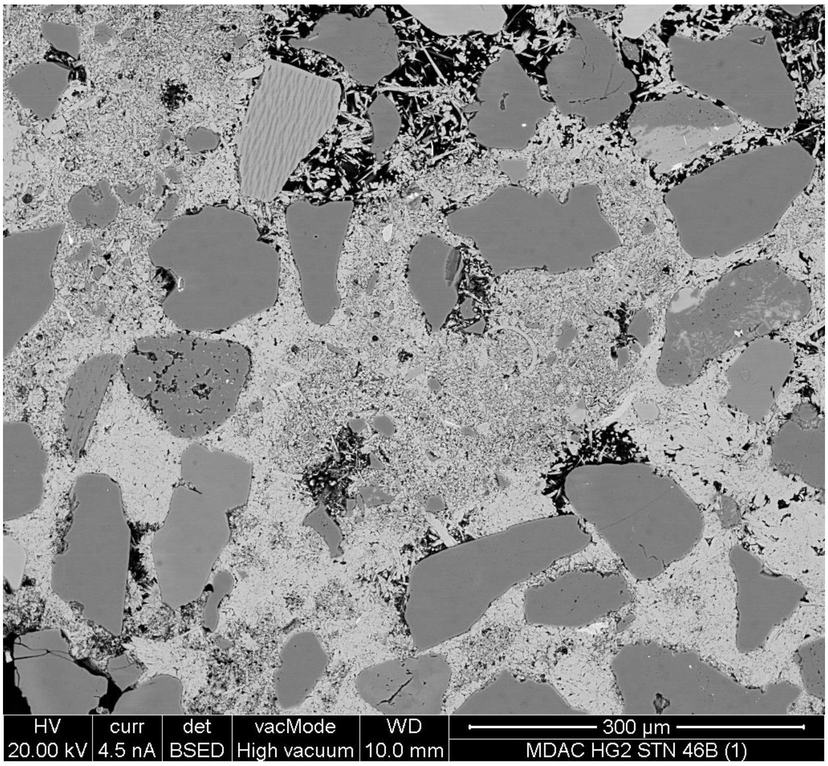

Figure 5. BSEM photomicrograph showing an uncompacted fabric of detrital grains of quartz (dark grey) and minor K-feldspar (mid-grey) in the lower, micro-porous aragonite-cemented sandstone (light-grey). The outline of large pelloidal carbonate grains can be seen in the centre and top left hand corner of the image. Sample HG2 STN 46B.

The aragonite cement is characterised by the growth of coarser acicular (needle-like) prismatic crystals up to 50 µm in length (Figure 6). Often the aragonite forms 'sheaf-like' crystal aggregates radiating 'sprays' of needles. The aragonite cement is locally very microporous in patches (Figure 7). Elsewhere, finer (1-5 µm diameter) and more equant-to-blocky aragonite crystals fill between the larger crystals to form patches of locally denser cement (Figure 6). This finer grained aragonite appears to be a later generation or the last stage of aragonite cementation.

The magnesian calcite cement is generally much finer grained and micritic in character, with little or no tendency to form euhedral crystals (Figure 8). It typically occurs as microcrystalline calcite that has nucleated within the matrix of the sediment, penetrating between the clay particles and displacively pushing apart the fine clay matrix material. It also replaces the clay matrix, producing 'feathery' like microstructures (Figure 8). Calcite crystallite size is usually less than 2 µm. However, more tightly-cemented parts of the carbonate-cemented clast show coarsening of the calcite by partial recrystallisation of the micritic calcite to form calcite microsparrite (Figure 9). Close to the contact with the overlying aragonite-cemented sandstone, small cavities and voids in the magnesian calcite-cemented matrix are sometimes lined or filled by small euhedral crystals of aragonite (Figure 8). The aragonite rests on the magnesian calcite surfaces and clearly post-dates the precipitation of the magnesian calcite.

Quantitative EPMA major element compositional data for the aragonite and magnesian calcite cements are presented in detail in Table 2. Their compositional variation, expressed in terms of molar proportions of $CaCO_3$-$MgCO_3$-$SrCO_3$, is summarised in Figure 10 and Figure 11.

The aragonite is strontium-bearing, with between 1 to 2 mole % $SrCO_3$ in solid-solution (Figure 10) within the aragonite crystal lattice (i.e. the structural formula of the aragonite can be represented as $Ca_{0.98-0.99}Sr_{0.02-0.01}CO_3$). Together with the prismatic morphology, the relatively high Sr content suggests that this carbonate cement is aragonite rather than calcite, since Sr is much more abundant in aragonite than in calcite (Deer et al., 1962a,b). This is because Sr is much more readily incorporated in the orthorhombic crystal structure of aragonite, which can form a partial solid-solution series with the end-member orthorhombic strontianite ($SrCO_3$).

Aragonite cement has been recorded previously by Judd (2005) in MDAC from the Mid Irish Sea, and needles of aragonite have also been described encrusting sand grains (similar to the pore-filling acicular aragonite described above) by Croker et al. (2005) from SEM observations of recovered from potential MDAC samples recovered in the Western Irish Sea. Similar acicular and "pelleted" aragonite fabrics have been observed in previous studies of MDAC from other areas (e.g. Hovland and Talbot, 1987; Jensen et al., 1992; Bohrmann et al., 1998; Peckmann et al., 2001; Muralidhar et al., 2006; Milodowski et al., 2009). Peckmann et al. (2001) report the formation of acicular Sr-rich aragonite cement, with between 8300-9500 ppm Sr, in MDAC associated with methane seeps from the Black Sea. The strontium content of the aragonite cements reported by Peckmann et al. (2001) and Milodowski et al. (2009) from the Mid Irish Sea is also of a similar order of magnitude to those we describe from the Braemar Pockmark area

The EPMA data for the magnesian calcite show it to contain between 13 to 23 mole % $MgCO_3$ in solid-solution (Figure 11) within the calcite lattice (i.e. the structural formula of the calcite can be represented as $Ca_{0.77-0.87}Mg_{0.23-0.13}CO_3$). Most analyses of the micritic calcite cluster towards the higher end of this range. However, SEM-EDXA observations indicate that the recrystallisation of the micrite to coarser microsparry calcite cement (Figure 9) produced calcite with a lower magnesium content. The composition of the calcite lies about third of the way along the compositional join between end-member calcite and 'ideal' dolomite. As such, these cements are at high-magnesian calcite end of the calcite ($CaCO_3$)-magnesite ($MgCO_3$) solid-solution series (cf. Deer et al., 1962a,b; Mackenzie et al., 1983). The composition is within the range of composition of magnesium calcite recorded from MDAC samples from elsewhere (Jensen et al., 1992). It is much more magnesian than calcite reported from some sites (e.g. Peckmann et al., 2001) but less magnesian than the calcites described previously by the authors from MDAC samples recovered from the Mid Irish Sea (Milodowski et al., 2009).

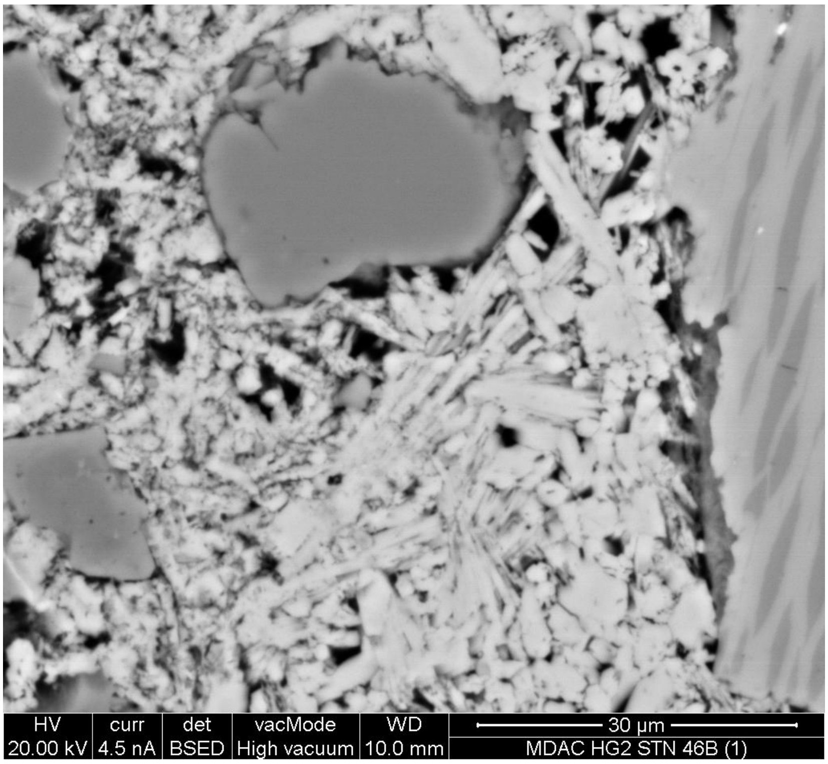

Figure 6. BSEM photomicrograph of the aragonite cement showing typical fabric of coarser acicular (needle-like) crystals with smaller, more equant and blocky aragonite crystals between. Detrital quartz (grey) and perthitic K-feldspar (right) display markedly etched and corroded grain boundaries. Sample HG2 STN 46B.

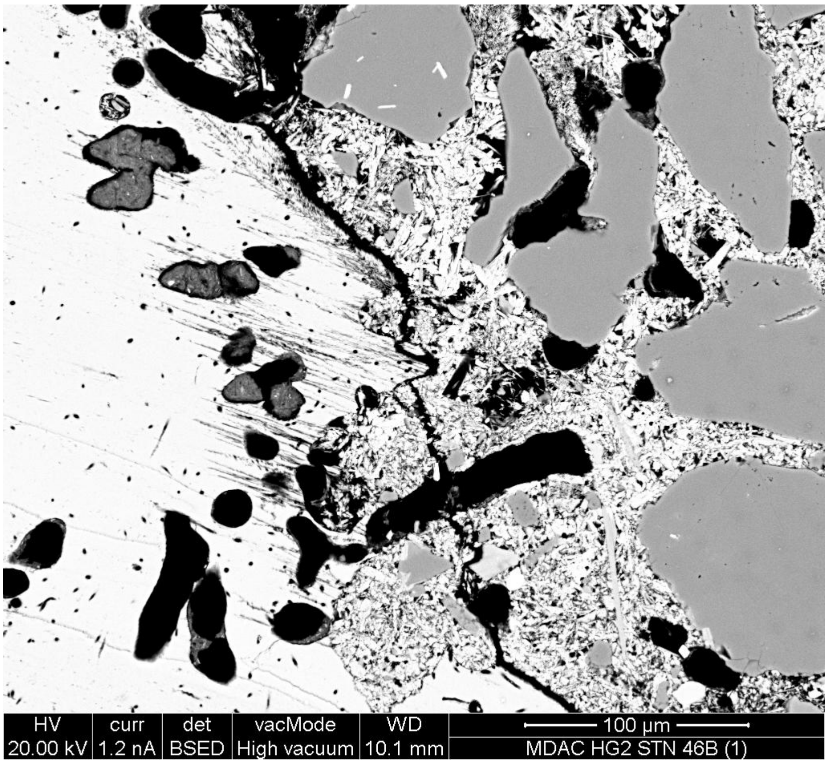

Figure 7. BSEM photomicrograph showing acicular microcrystalline aragonite (white) forming a highly microporous cement between etched detrital quartz grains (mid-grey). The edge of an aragonitic mollusc shell is seen at the left edge of the image, and displays fine porous micro-boring structures. Sample HG2 STN 46B.

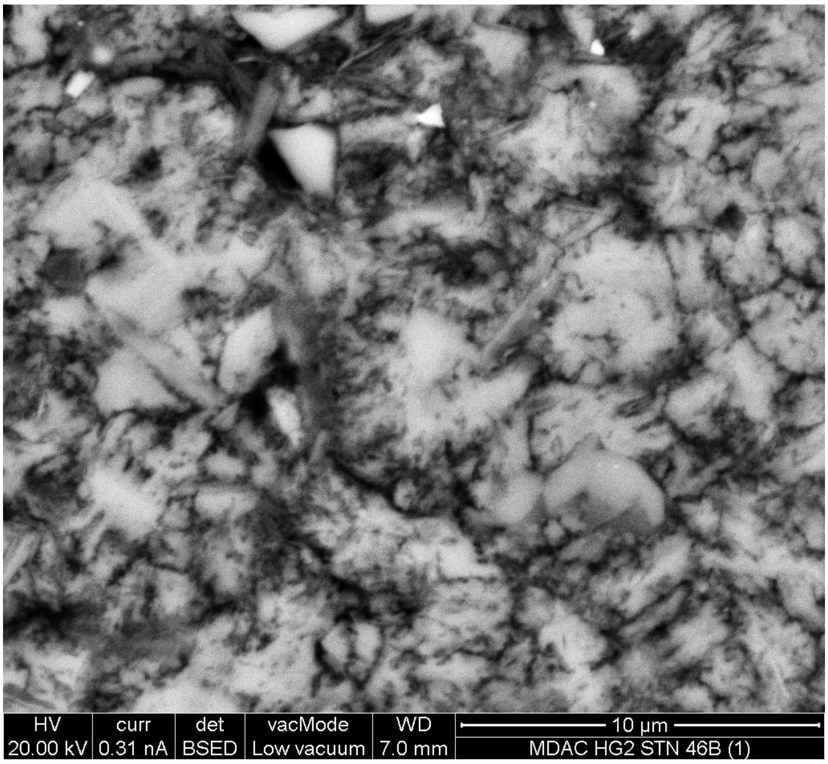

Figure 8. BSEM photomicrograph shows microporous micritic high-magnesian calcite cement, comprising anhedral micro-crystals (light grey) penetrating into, displacing and replacing interstitial clay matrix material (darker grey). Occasional coarser euhedral aragonite crystals (white) are seen within large voids in the matrix Sample HG2 STN 46B.

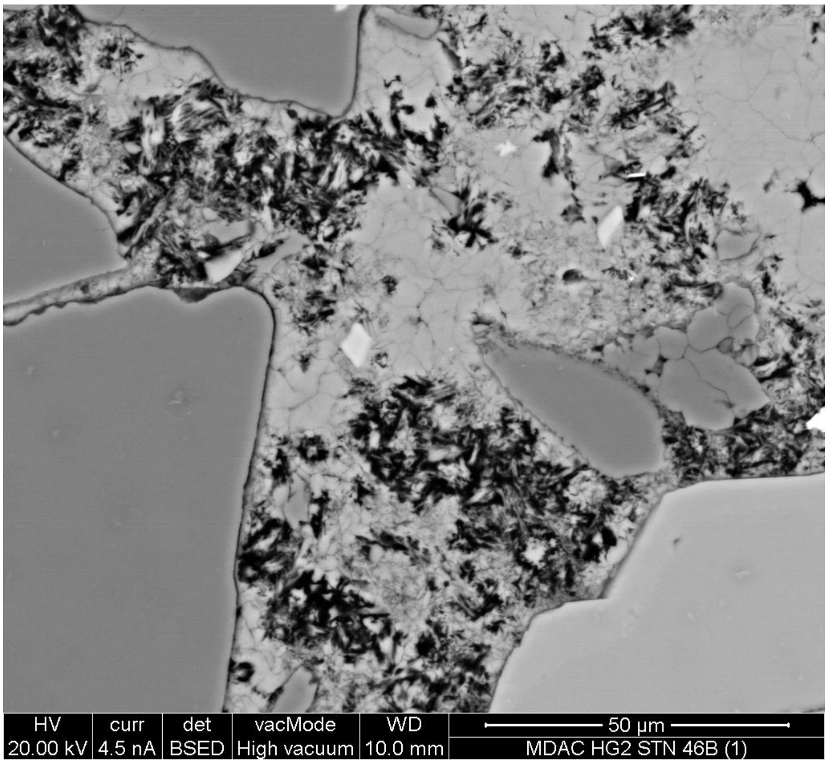

Figure 9. BSEM photomicrograph illustrating the recrystallisation and coarsening-up of the highly micro-porous, magnesian calcite micritic cement (dark) to denser, less-magnesian calcite microsparrite cement (mid-grey). The coarser microsparrite calcite eventually replaces the finer micritic matrix calcite. Sample HG2 STN 46B.

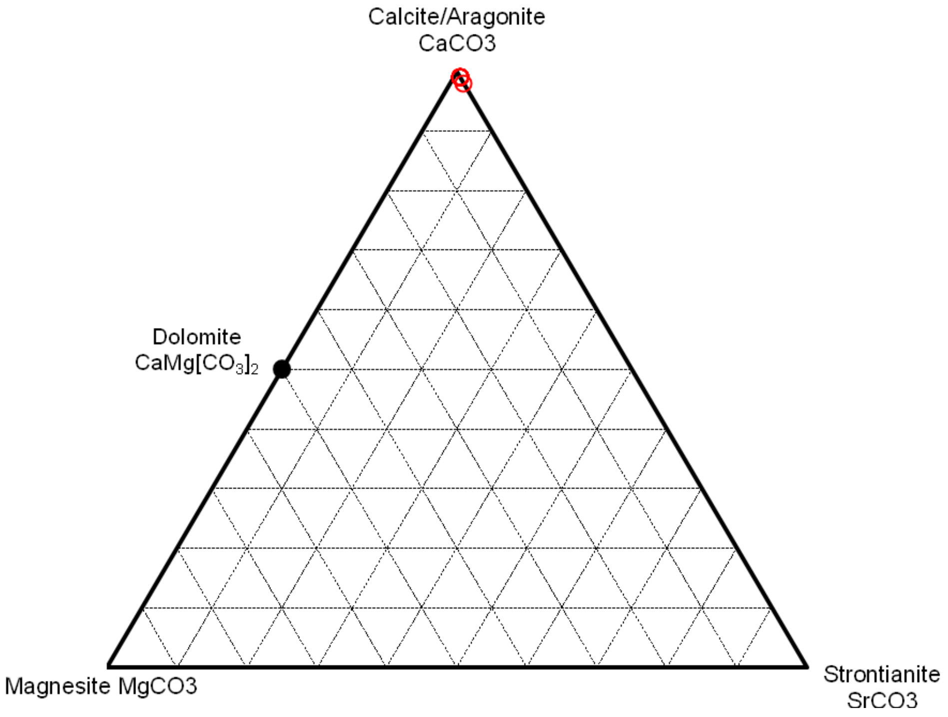

Figure 10. $CaCO_3$-$MgCO_3$-$SrCO_3$ molar ratio plot illustrating the composition of the acicular and dense aragonite cements (red circles) in MDAC sample HG2 STN 46B, relative to end-member carbonate minerals.

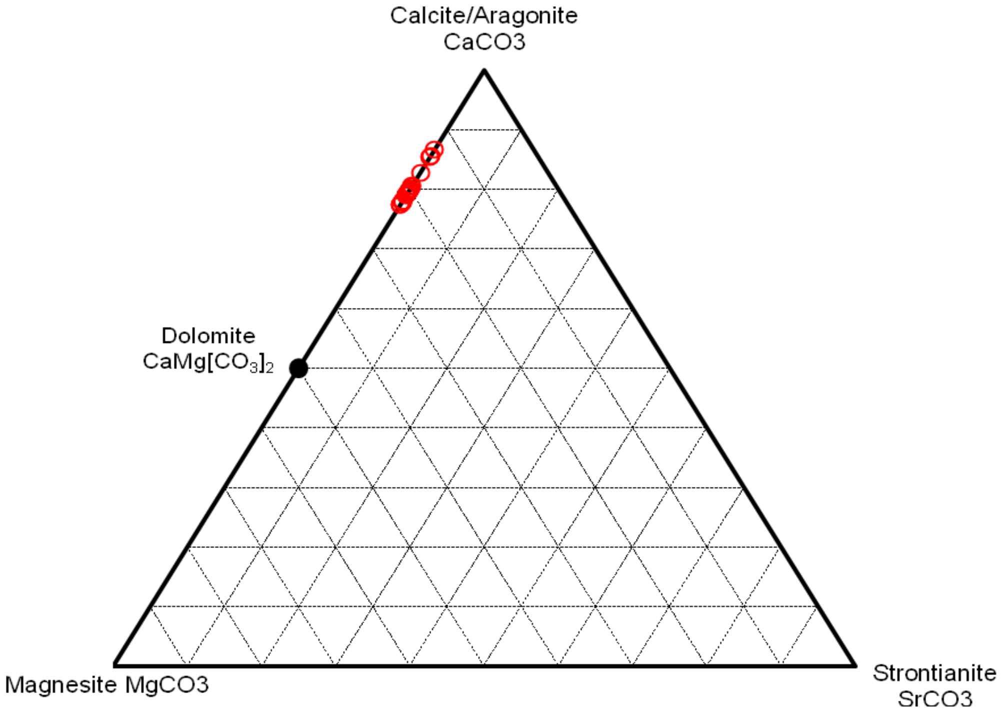

Figure 11. $CaCO_3$-$MgCO_3$-$SrCO_3$ molar ratio plot illustrating the composition of the partially recrystallised micritic high magnesian calcite cements (red circles) in MDAC sample HG2 STN 46B, relative to end-member carbonate minerals.

Table 2. Electron microprobe analyses of carbonate cements and other carbonate components in sample HG2 STN 46B.

No.	WEIGHT % OXIDE (normalised)							IONIC RATIO [normalised to 3 [O]						COMMENTS
	MgO	CaO	MnO	FeO	SrO	CO_2 (calc)	*Total wt%	Mg^{2+}	Ca^{2+}	Mn^{2+}	Fe^{2+}	Sr^{2+}	CO_3^{2-}	
1	0.00	54.83	0.00	0.00	1.51	43.66	100.00	0.00	0.99	0.00	0.00	0.01	1.00	Acicular aragonite
2	0.00	55.04	0.00	0.00	1.25	43.71	100.00	0.00	0.99	0.00	0.00	0.01	1.00	Acicular aragonite
3	0.00	55.15	0.00	0.00	1.10	43.74	100.00	0.00	0.99	0.00	0.00	0.01	1.00	Acicular aragonite
4	0.00	54.99	0.00	0.00	1.31	43.70	100.00	0.00	0.99	0.00	0.00	0.01	1.00	Acicular aragonite
5	0.00	54.97	0.00	0.00	1.33	43.70	100.00	0.00	0.99	0.00	0.00	0.01	1.00	Acicular aragonite
6	0.00	54.77	0.00	0.00	1.59	43.64	100.00	0.00	0.98	0.00	0.00	0.02	1.00	Acicular aragonite
7	0.00	54.94	0.00	0.00	1.37	43.69	100.00	0.00	0.99	0.00	0.00	0.01	1.00	Acicular aragonite
8	7.84	45.69	0.00	0.93	0.39	45.15	100.00	0.19	0.79	0.00	0.01	0.00	1.00	Micritic magnesian calcite, partially recrystallised to microsparrite
9	8.35	45.23	0.00	0.92	0.23	45.27	100.00	0.20	0.78	0.00	0.01	0.00	1.00	Micritic magnesian calcite, partially recrystallised to microsparrite
10	6.82	46.89	0.00	1.05	0.25	44.99	100.00	0.17	0.82	0.00	0.01	0.00	1.00	Micritic magnesian calcite, partially recrystallised to microsparrite
11	8.26	45.02	0.00	1.21	0.29	45.21	100.00	0.20	0.78	0.00	0.02	0.00	1.00	Micritic magnesian calcite, partially recrystallised to microsparrite
12	5.78	47.34	0.00	1.84	0.33	44.71	100.00	0.14	0.83	0.00	0.03	0.00	1.00	Micritic magnesian calcite, partially recrystallised to microsparrite
13	5.55	46.87	0.00	2.67	0.30	44.60	100.00	0.14	0.82	0.00	0.04	0.00	1.00	Micritic magnesian calcite, partially recrystallised to microsparrite
14	8.83	41.25	0.00	4.59	0.36	44.97	100.00	0.21	0.72	0.00	0.06	0.00	1.00	Micritic magnesian calcite, partially recrystallised to microsparrite
15	8.52	42.57	0.00	3.65	0.24	45.03	100.00	0.21	0.74	0.00	0.05	0.00	1.00	Micritic magnesian calcite, partially recrystallised to microsparrite
16	8.27	43.96	0.00	2.45	0.21	45.11	100.00	0.20	0.76	0.00	0.03	0.00	1.00	Micritic magnesian calcite, partially recrystallised to microsparrite
17	5.42	48.22	0.00	1.35	0.31	44.70	100.00	0.13	0.85	0.00	0.02	0.00	1.00	Micritic magnesian calcite, partially recrystallised to microsparrite

Note: ***** *Analytical totals were low (<90%) because the cements were very microporous. Therefore all data were normalised to 100%*

Table 2 (continued). Electron microprobe analyses of carbonate cements in sample HG2 STN 46B.

No.	WEIGHT % OXIDE (normalised)							IONIC RATIO [normalised to 3 [O]]						COMMENTS
	MgO	CaO	MnO	FeO	SrO	CO_2 (calc)	*Total wt%	Mg^{2+}	Ca^{2+}	Mn^{2+}	Fe^{2+}	Sr^{2+}	CO_3^{2-}	
18	9.27	44.96	0.00	0.00	0.26	45.51	100.00	0.22	0.78	0.00	0.00	0.00	1.00	Micritic magnesian calcite, partially recrystallised to microsparrite
19	9.27	45.17	0.00	0.00	0.00	45.56	100.00	0.22	0.78	0.00	0.00	0.00	1.00	Micritic magnesian calcite, partially recrystallised to microsparrite
20	8.64	45.69	0.00	0.00	0.28	45.40	100.00	0.21	0.79	0.00	0.00	0.00	1.00	Micritic magnesian calcite, partially recrystallised to microsparrite
21	8.39	46.20	0.00	0.00	0.00	45.41	100.00	0.20	0.80	0.00	0.00	0.00	1.00	Micritic magnesian calcite, partially recrystallised to microsparrite
22	9.10	44.12	0.00	1.38	0.00	45.40	100.00	0.22	0.76	0.00	0.02	0.00	1.00	Micritic magnesian calcite, partially recrystallised to microsparrite
23	8.09	45.68	0.00	0.96	0.00	45.26	100.00	0.20	0.79	0.00	0.01	0.00	1.00	Micritic magnesian calcite, partially recrystallised to microsparrite
24	9.10	45.10	0.00	0.30	0.00	45.50	100.00	0.22	0.78	0.00	0.00	0.00	1.00	Micritic magnesian calcite, partially recrystallised to microsparrite
25	7.64	44.57	0.00	2.78	0.00	45.01	100.00	0.19	0.78	0.00	0.04	0.00	1.00	Micritic magnesian calcite, partially recrystallised to microsparrite
26	8.94	45.56	0.00	0.00	0.00	45.50	100.00	0.21	0.79	0.00	0.00	0.00	1.00	Micritic magnesian calcite, partially recrystallised to microsparrite
27	9.01	45.25	0.00	0.00	0.28	45.46	100.00	0.22	0.78	0.00	0.00	0.00	1.00	Micritic magnesian calcite, partially recrystallised to microsparrite
28	8.01	44.45	0.00	2.08	0.40	45.06	100.00	0.19	0.77	0.00	0.03	0.00	1.00	Micritic magnesian calcite, partially recrystallised to microsparrite
29	0.00	55.12	0.00	0.00	1.15	43.73	100.00	0.00	0.99	0.00	0.00	0.01	1.00	Dense aragonite-cemented boring
30	0.00	55.05	0.00	0.00	1.24	43.71	100.00	0.00	0.99	0.00	0.00	0.01	1.00	Dense aragonite-cemented boring
31	0.00	55.09	0.00	0.00	1.19	43.73	100.00	0.00	0.99	0.00	0.00	0.01	1.00	Dense aragonite-cemented boring
32	0.00	55.05	0.00	0.00	1.24	43.71	100.00	0.00	0.99	0.00	0.00	0.01	1.00	Dense aragonite-cemented boring
33	0.00	55.07	0.00	0.00	1.21	43.72	100.00	0.00	0.99	0.00	0.00	0.01	1.00	Dense aragonite-cemented boring

Note: **Analytical totals were low (<95%) because the cements were very microporous. Therefore all data were normalised to 100%*

Table 2 (continued). Electron microprobe analyses of carbonate cements in sample HG2 STN 46B.

No.	WEIGHT % OXIDE (normalised)							IONIC RATIO [normalised to 3 [O]						COMMENTS
	MgO	CaO	MnO	FeO	SrO	CO_2 (calc)	*Total wt%	Mg^{2+}	Ca^{2+}	Mn^{2+}	Fe^{2+}	Sr^{2+}	CO_3^{2-}	
34	0.00	55.01	0.00	0.00	1.28	43.71	100.00	0.00	0.99	0.00	0.00	0.01	1.00	Dense aragonite-cemented boring
35	0.00	54.89	0.00	0.15	1.26	43.70	100.00	0.00	0.99	0.00	0.00	0.01	1.00	Dense aragonite-cemented boring
36	0.00	55.00	0.00	0.00	1.29	43.70	100.00	0.00	0.99	0.00	0.00	0.01	1.00	Dense aragonite-cemented boring
37	0.00	55.07	0.00	0.00	1.21	43.72	100.00	0.00	0.99	0.00	0.00	0.01	1.00	Dense aragonite-cemented boring
38	0.00	55.10	0.00	0.00	1.17	43.73	100.00	0.00	0.99	0.00	0.00	0.01	1.00	Dense aragonite-cemented boring

***Note:* *Analytical totals were low (<95%) because the cements were very microporous. Therefore all data were normalised to 100%**

The interface between the high-magnesian calcite-cemented sandstone layer and the overlying aragonite-cemented sandstone horizon is very sharp (Figure 12). Similarly, the burrow walls and contacts between the aragonite-cemented sandstone fill in the sub-vertical burrow and the high-magnesian calcite-cemented host sandstone are also very sharp (Figure 13). Although the aragonite-mineralised fabrics cut across the magnesian calcite, there is little or no permeation of aragonite into the adjacent magnesian calcite-cemented matrix of the host sediment. However, BSEM observations suggest that the magnesian calcite-cemented sandstone immediately in contact with the aragonite-cemented sediment, is slightly more microporous within narrow zones (<100 µm wide) immediately beneath the contacts between the two sediment types evident from the presence of darker zones beneath the contact areas revealed in BSEM imaging (Figure 12 and Figure 13). This may indicate that there has been some dissolution and leaching of the magnesian calcite-cemented sandstone prior to the deposition of the overlying aragonite-cemented sediment layer and associated infilling of burrows by aragonite-cemented sediment.

High-resolution BSEM petrography revealed the presence of authigenic pyrite disseminated throughout the carbonate-cemented sediment. In contrast to some of the other samples examined from the Braemar Pockmark, the pyrite is not framboidal. Instead it occurs as very fine grained (<2 µm) isolated and scattered crystals intimately associated (and probably coeval) with the micritic high-magnesian calcite. Both the sediment beneath the erosional contact surface, and the walls of the burrows, in the magnesian calcite-cemented sandstone are stained orange-brown to a depth of 1-2 mm (Figure 3). BSEM-EDXA observations show that this is due to the partial oxidation and alteration of pyrite to finely-disseminated secondary iron oxide (probably iron oxyhydroxide). Many of the other fragments of carbonate-cemented clasts recovered from this sampling location in the Braemar Pockmark displayed faint staining of their surfaces by iron oxyhydroxide (Figure 2), which is probably of similar origin.

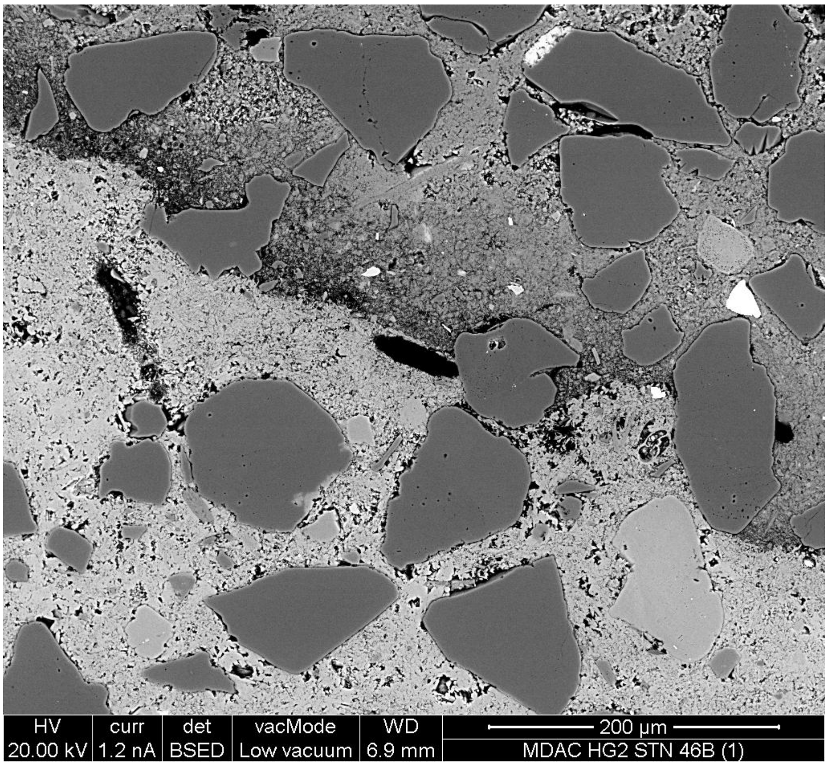

Figure 12. BSEM photomicrograph showing the sharp interface between aragonite- (white) and magnesian calcite (mid grey) cemented sandstone layers. Both sandstones display uncompacted detrital quartz (dark grey) and minor K-feldspar (light grey). Some quartz grains are etched and corroded by the carbonate cements. The orientation of this image is inverted relative to the orientation shown in Figure 3. Sample HG2 STN 46B.

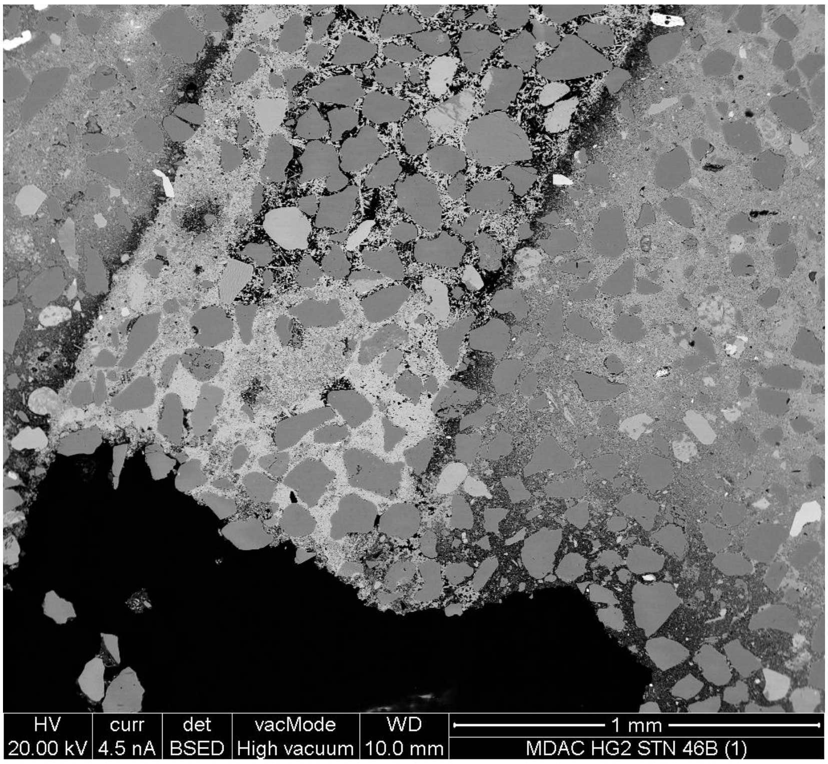

Figure 13. BSEM photomicrograph of a burrow filled by fine sand cemented by acicular aragonite (white), within fine sand cemented by high-magnesian calcite (mid-grey). The burrow walls are sharply-defined with a very narrow fringe of more porous sandstone (darker). Sample HG2 STN 46B.

The petrographic observations show that this carbonate-cemented sediment has a complex history. The sharply defined walls to the burrows of marine macrofauna that are preserved in the magnesian calcite-cemented sediment testify that the sediment must have been reasonably competent and rigid prior to the deposition of later sediment that infilled these structures and which was subsequently cemented by aragonite. However, the sediment must still have been reasonably soft enough to allow burrowing organisms to penetrate into the sediment. The finer-scale boring microstructures seen on the surfaces of the carbonate-cemented clasts are generally not sediment-filled or cemented by aragonite, and probably post-date both magnesian calcite and aragonite precipitation, and were clearly produced after complete lithification of the sediment. The observations also indicate that there was a hiatus in carbonate precipitation between the precipitation of magnesian calcite and the precipitation of later aragonite, during which sediment erosion and burrowing activity occurred. During this time the sea bed and sediment surface environment must have been oxic, since this erosion and burrowing was accompanied by oxidation of pyrite in the near-surface of the sediment and in the walls of burrows. The sequence of sedimentary and post-depositional diagenetic events can be summarised as follows:

1. Deposition of very fine sand and silt sediment;
2. Bioturbation;
3. Precipitation of micritic high-magnesian calcite within the near-surface of the sediment, simultaneously associated with iron and sulphate reduction in the anoxic sediment and the precipitation of fine authigenic pyrite;
4. Partial recrystallisation of micritic high-magnesian calcite to fine grained lower magnesian calcite, probably accompanied by partial lithification of the sediment;

5. Erosion and burrowing of the partially lithified sediment, associated with the development of oxic seabed conditions accompanied by oxidation of pyrite in the near-surface of the sediment;
6. Renewed deposition of fine sand and silt sediment;
7. Precipitation of aragonite within the near-surface of the sediment and lithification;
8. Erosion of the aragonite-magnesian calcite-cemented sediment, with local transport and abrasion of the eroded clasts of carbonate-cemented sandstone and siltstone.

3.2 SAMPLE HG2 STN 46C

Sample HG2 STN 46C is mineralogically similar to HG2 STN 46B and contains both aragonite and magnesian calcite cements. The sample comprised a series of fragments of dark grey to light brownish grey carbonate-cemented fine sandstone and siltstone ranging in size from <5 mm to 50 mm diameter. The fragments were typically irregular in form, varying from lenticular-to-platy and moderately well-rounded clasts, to elongate tubular forms some of which appear to be partially hollow and may represent carbonate-cemented sediment-filled burrow structures (Figure 14). As in HG2 STN 46B, the surfaces of the fragments are commonly bored by marine organisms and some of the larger platy clasts were seen to be encrusted by white calcareous tubes secreted by serpulid worms. Some of the clast surfaces are weakly oxidised and stained by iron oxyhydroxide.

Figure 14. Photograph showing the range of shapes and sizes of the fragments of carbonate cemented sandstone and siltstone in sample HG2 STN 46C. Many fragments are moderately well rounded, and some are encrusted with calcareous serpulid tubes. Elongated tubular fragments of carbonate cemented siltstone are also present.

The polished section prepared through a fragment of HG2 STN 46C is shown in Figure 15. It has a central 'core' represented by a very well-rounded and abraded clast of dark-grey magnesian calcite-cemented fine sandstone to siltstone, which is enclosed within a matrix of lighter buff-grey-coloured aragonite-cemented very shelly fine sandstone. The host shelly fragments of the host sediment are dominated by molluscan shell fragments up to 8 mm in length, and are well-sorted and have a strong bedding-parallel alignment. However, bioclasts also include some microporous echinoid spines and formaminiferal tests (e.g. Figure 16). Both the magnesian calcite-cemented sandstone 'core clast' and the enclosing aragonite-cemented shelly sandstone display uncompacted or 'expanded' grain fabrics (Figure 16 and Figure 17), which indicates the carbonate cements must have formed in the near-surface of the sediment before any significant burial and compaction.

The enclosing shelly sediment contains some burrows up to 3 mm diameter that are partially filled with similar aragonite-cemented sediment. The magnesian calcite-cement 'core clast' contains an empty cavity up to 4 mm in diameter that may represent a boring by a marine macro-organism. The molluscan shell fragments are typically riddled by the very fine borings of marine organisms.

The outer margin of the 'core' clast and the enclosing host shelly sandstone are stained by traces of finely-disseminated iron oxyhydroxide which imparts a buff colour to the rock. Some of the bioclasts are more heavily impregnated by orange-brown iron oxyhydroxide (Figure 15).

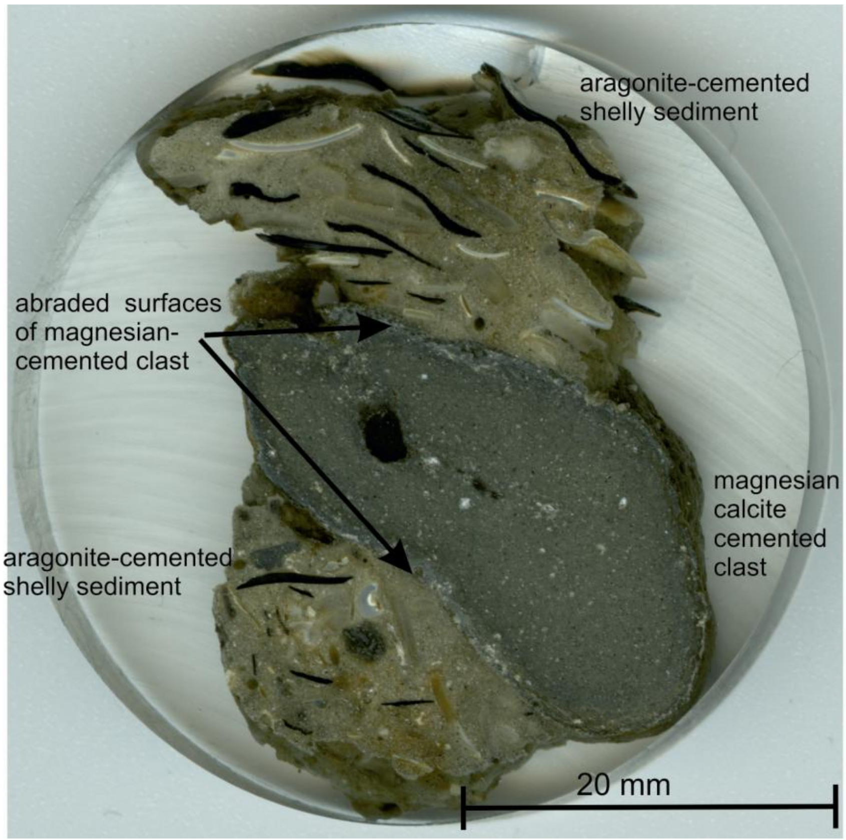

Figure 15. Polished section through a fragment of carbonate-cemented siltstone and sandstone. It shows a central 'core' comprising a well-rounded and abraded clast of dark-grey magnesian calcite-cemented fine sandstone to siltstone, enclosed within a matrix of lighter buff-grey-coloured aragonite-cemented very shelly fine sandstone The magnesian calcite-cemented core has a large empty boring. The aragonite-cemented siltstone-fine sandstone contains large burrows partially-filled with similar sediment to the host rock. The aragonitic sediment and surfaces of the core clast are stained by orange-brown by finely-disseminated secondary iron oxyhydroxide. Sample HG2 STN 46C.

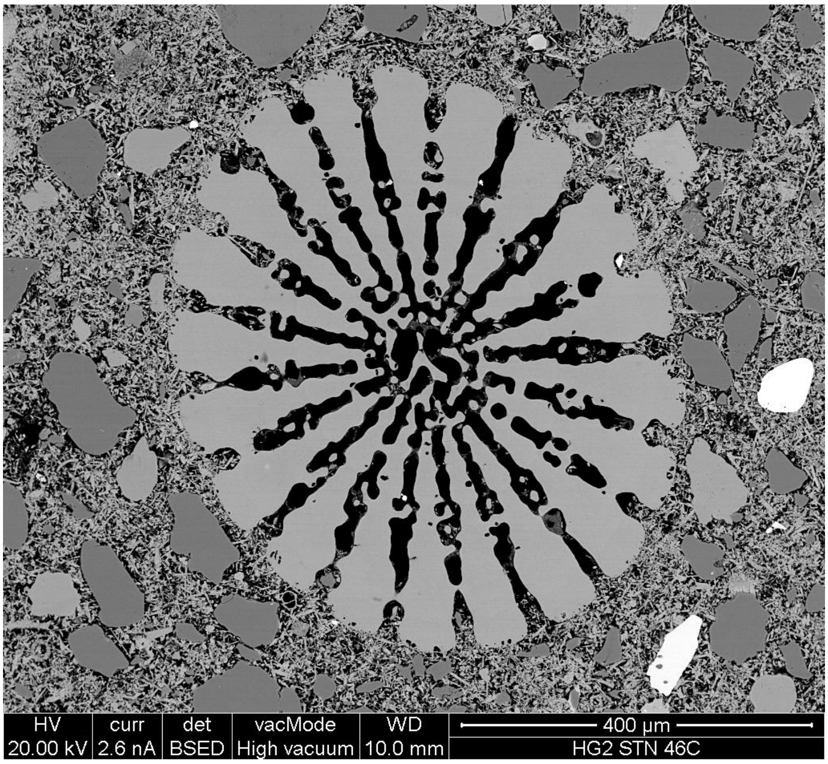

Figure 16. BSEM photomicrograph of a cross-section through an echinoid spine showing the detail of its internal structure. The spine sits within a matrix of fine sandstone comprising uncompacted and corroded detrital quartz and K-feldspar grains, cemented by interstitial pore-filling microporous acicular aragonite. Sample HG2 STN 46C.

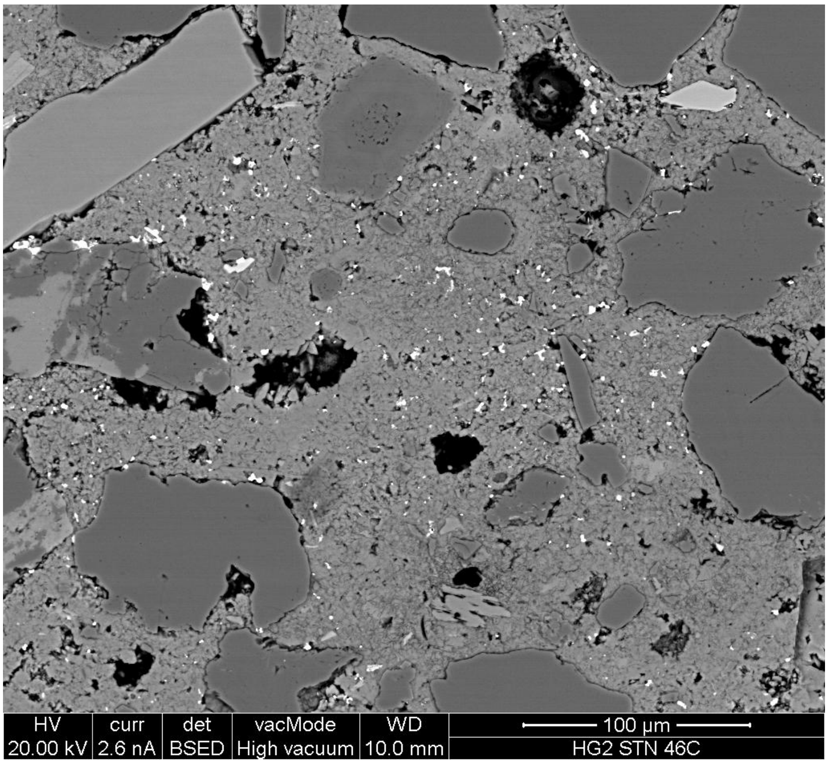

Figure 17. BSEM photomicrograph showing uncompacted detrital grain fabric of corroded angular detrital quartz (mid-grey) and quartz-K-feldspar lithic grains, ‘floating’ in a matrix of interstitial micritic magnesian calcite. Abundant fine grained pyrite (white) is disseminated throughout the micrite matrix. Sample HG2 STN 46C.

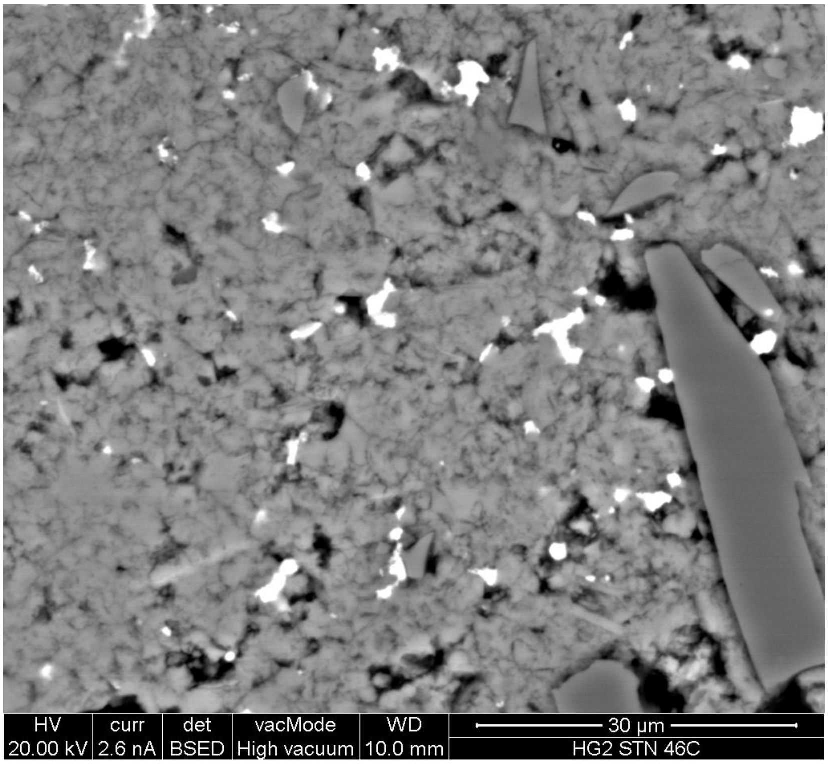

Figure 18. BSEM photomicrograph of micritic magnesian calcite cement within 'core clast'. The calcite comprises 'globular aggregates' of microcrystalline calcite (light grey) with fine interstitial pyrite (white) between the calcite aggregates. Sample HG2 STN 46C.

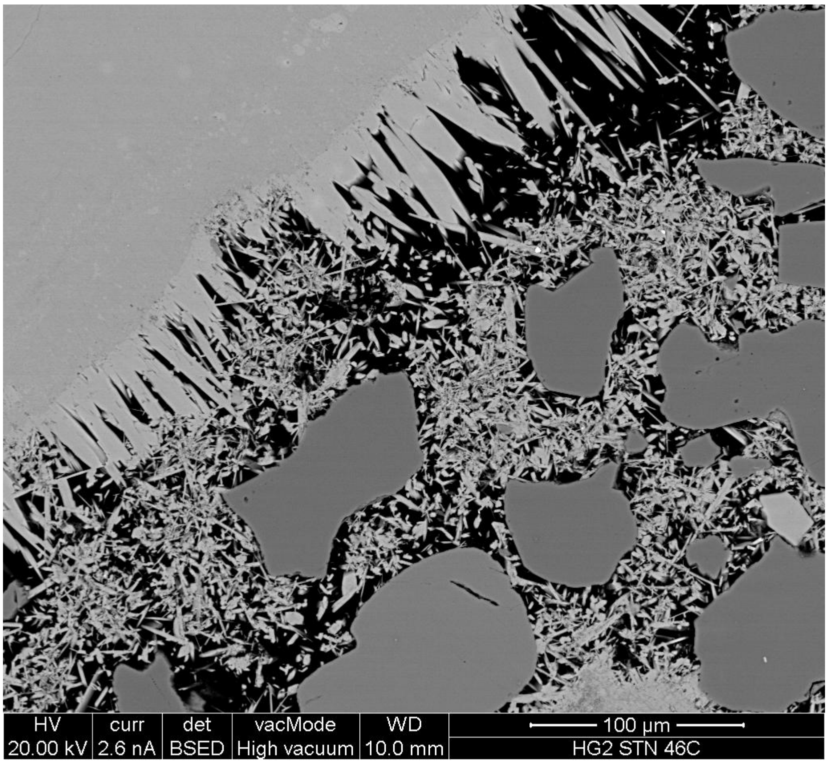

Figure 19. BSEM photomicrograph showing fibrous to acicular aragonite cement forming a microporous interstitial cement in sandstone. Coarser needles of aragonite can be seen to form syntaxially-orientated overgrowths on the surface of a fragment of mollusc shell (top left of image). Sample HG2 STN 46C.

The micritic magnesian calcite cement of the 'core clast' consists of globular aggregates up to 10 μm in diameter, made up of very fine (<2 μm) crystallites of calcite (Figure 18). This forms a relatively tightly-cemented sandstone fabric (Figure 17 and Figure 18). Locally, patches of the micritic magnesian calcite have partially recrystallised and coarsened up. EDXA shows that this later calcite is much lower in magnesium. Abundant fine authigenic pyrite occurs interstitially partly filling the residual microporosity between the micrite aggregates (Figure 18). As in HG2 STN 46C the pyrite in this carbonate-cemented sediment is not framboidal, which contrasts with the framboidal pyrite generally found in most of the other samples of carbonate-cemented sediment from the Braemar Pockmark area. The abundance of fine pyrite probably accounts for the dark grey colour of the 'core clast'.

The aragonite cement in the shelly sandstone host rock comprises fine acicular or acute prismatic crystal aggregates of aragonite filling the intergranular porosity (Figure 16 and Figure 19). The aragonite crystals are loosely-packed, and as result the cement is highly microporous (Figure 16 and Figure 19). In addition to the fine-grained pore-filling aragonite, much coarser needle-like crystals of aragonite have formed as syntaxial overgrowths on the outer surfaces of many of mollusc shell detritus (Figure 19). The pore-filling acicular aragonite must have precipitated later than the coarse aragonite overgrowths on mollusc shells, since it was seen to fill between the earlier aragonite overgrowth crystals (Figure 19).

Quantitative EPMA major element compositional data for the aragonite and magnesian calcite cements are presented in detail in Table 3. Their compositional variation, expressed in terms of molar proportions of $CaCO_3$-$MgCO_3$-$SrCO_3$, is summarised in Figure 20.

The aragonite cement is strontium-bearing, with between 1 to 2 mole % $SrCO_3$ in solid-solution (Figure 20) within the aragonite crystal lattice (i.e. the structural formula of the aragonite can be represented as $Ca_{0.98-0.99}Sr_{0.02-0.01}CO_3$). The prismatic morphology of the crystals, coupled with the relatively high Sr content identify this carbonate cement as aragonite rather than calcite, since Sr is much more abundant in aragonite than in calcite (Deer et al., 1962a,b). This is because Sr is much more readily incorporated in the orthorhombic crystal structure of aragonite, which can form a partial solid-solution series with the end-member orthorhombic strontianite ($SrCO_3$). However, some analyses indicate the presence of up to 3 mole % $MgCO_3$ in some aragonite crystals. The chemistry of the aragonite in the shell fragments is different in that it is generally low in strontium (Figure 20). The aragonite cement is very similar to that described from sample HG2 STN 46B and found previously in other MDAC sediments elsewhere (see Section 3.1).

The EPMA data for the micritic magnesian calcite show it to contain between 14 to 21 mole % $MgCO_3$ in solid-solution (Figure 20) within the calcite lattice (i.e. the structural formula of the calcite can be represented as $Ca_{0.79-0.86}Mg_{0.21-0.14}CO_3$). Most analyses of the micritic calcite cluster towards the higher end of this range and are similar to the micritic calcite cement found in sample HG2 STN 46B. As such, these cements are at high-magnesian calcite end of the calcite ($CaCO_3$)-magnesite ($MgCO_3$) solid-solution series (cf. Deer et al., 1962a,b; Mackenzie et al., 1983). However, SEM-EDXA observations indicate that the recrystallisation of the micrite to coarser microsparry calcite cement produced calcite with a lower magnesium content (Figure 20) with about 5 mole % $MgCO_3$ in sold solution (i.e. $Ca_{0.95}Mg_{0.05}CO_3$).

The petrographic observations show that this carbonate-cemented sediment has a complex history similar to that of sample HG2 STN 46B (see Section 3.1). The preservation of an abraded and worn clast of magnesian calcite-cemented sediment as a pebble within the aragonite-cemented shelly sandstone indicate that there was a hiatus in carbonate precipitation between the precipitation of magnesian calcite and the precipitation of later aragonite. It shows that the magnesian calcite-cemented sediment must have been well-lithified, and then eroded prior to the deposition of aragonite-cemented sandstone. The finer-scale boring microstructures seen on the surfaces of the carbonate-cemented clasts are generally not sediment-filled or cemented by aragonite, and probably post-date both magnesian calcite and aragonite precipitation, and were clearly produced after complete lithification of the sediment. The aragonite-cemented rock has also been abraded and worn, indicating that a second phase of erosion occurred after aragonite precipitation. During this time the sea bed and sediment surface environment must also have been oxic, since this erosion and burrowing was accompanied by oxidation of pyrite in the near-surface of the sediment and in the walls of borings on the surfaces of the clasts of carbonate-cemented sediment. The sequence of sedimentary and post-depositional diagenetic events can be summarised as follows:

1. Deposition of very fine sand and silt sediment;
2. Bioturbation;
3. Precipitation of micritic high-magnesian calcite within the near-surface of the sediment, simultaneously associated with iron and sulphate reduction in the anoxic sediment and the precipitation of fine authigenic pyrite;
4. Partial recrystallisation of micritic high-magnesian calcite to fine grained lower magnesian calcite, associated with further lithification of the sediment;
5. Erosion and burrowing of the lithified high-magnesian calcite cemented rock, and current rolling and abrasion of eroded clasts;
6. Renewed deposition of fine sand and abundant shelly detritus;
7. Precipitation of aragonite within the near-surface of the sediment and lithification. Initially aragonite formed overgrowths seeded on aragonitic shell fragments but subsequently, aragonite cement precipitated as an intergranular cement in the sediment;
8. Erosion of the aragonite-magnesian calcite-cemented sediment, with local transport and abrasion of the eroded clasts of carbonate-cemented sandstone and siltstone, and oxidation of pyrite to form finely disseminated iron oxyhydroxide now staining the clasts.

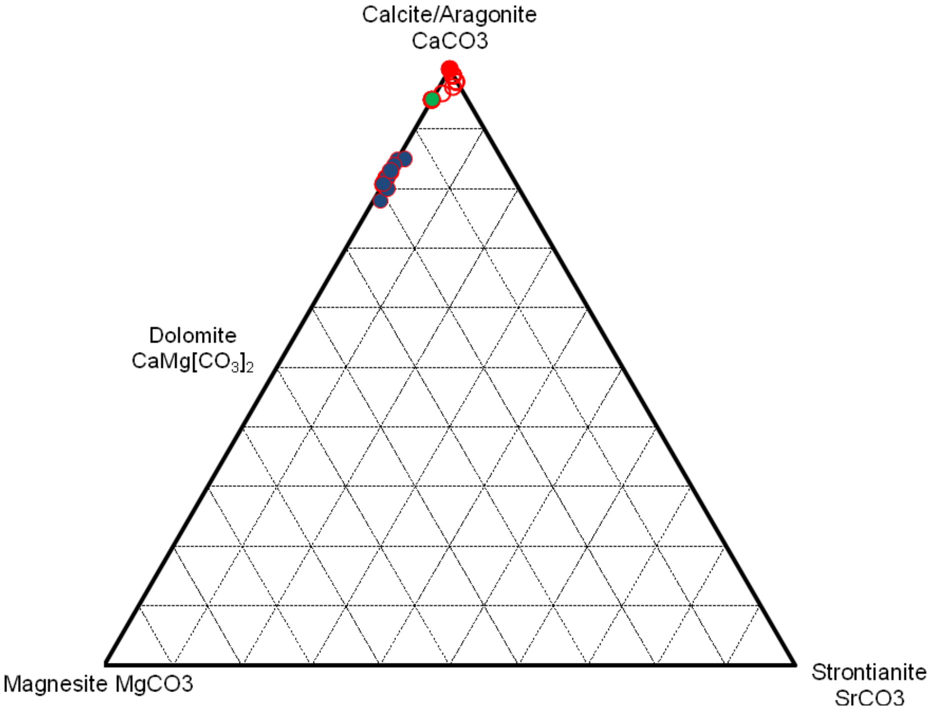

Figure 20. $CaCO_3$-$MgCO_3$-$SrCO_3$ molar ratio plot illustrating the composition of the aragonitic bivalve shells (solid red circles), acicular aragonite cement (open red circles), and micritic high-magnesian calcite in (solid blue circles) and later coarser magnesian calcite replacing micritic calcite (slid green circles). MDAC sample HG2 STN 46C, relative to end-member carbonate minerals.

Table 3. Electron microprobe analyses of carbonate cements in sample HG2 STN 46C.

No.	WEIGHT % OXIDE (normalised)							IONIC RATIO [normalised to 3 [O]						COMMENTS
	MgO	CaO	MnO	FeO	SrO	CO_2 (calc)	*Total wt%	Mg^{2+}	Ca^{2+}	Mn^{2+}	Fe^{2+}	Sr^{2+}	CO_3^{2-}	
1	7.68	47.03	0.00	0.00	0.00	45.29	100.00	0.19	0.81	0.00	0.00	0.00	1.00	Micritic magnesian calcite, partially recrystallised to microsparrite
2	7.05	47.29	0.00	0.53	0.00	45.13	100.00	0.17	0.82	0.00	0.01	0.00	1.00	Micritic magnesian calcite, partially recrystallised to microsparrite
3	7.77	46.11	0.00	0.90	0.00	45.21	100.00	0.19	0.80	0.00	0.01	0.00	1.00	Micritic magnesian calcite, partially recrystallised to microsparrite
4	6.19	48.31	0.00	0.53	0.00	44.98	100.00	0.15	0.84	0.00	0.01	0.00	1.00	Micritic magnesian calcite, partially recrystallised to microsparrite
5	7.93	46.35	0.00	0.43	0.00	45.29	100.00	0.19	0.80	0.00	0.01	0.00	1.00	Micritic magnesian calcite, partially recrystallised to microsparrite
6	7.55	46.96	0.00	0.25	0.00	45.24	100.00	0.18	0.81	0.00	0.00	0.00	1.00	Micritic magnesian calcite, partially recrystallised to microsparrite
7	7.44	46.66	0.00	0.73	0.00	45.17	100.00	0.18	0.81	0.00	0.01	0.00	1.00	Micritic magnesian calcite, partially recrystallised to microsparrite
8	7.34	47.25	0.00	0.20	0.00	45.21	100.00	0.18	0.82	0.00	0.00	0.00	1.00	Micritic magnesian calcite, partially recrystallised to microsparrite
9	8.77	44.89	0.00	0.71	0.27	45.35	100.00	0.21	0.78	0.00	0.00	0.01	1.00	Micritic magnesian calcite, partially recrystallised to microsparrite
10	8.02	45.87	0.00	0.54	0.36	45.22	100.00	0.19	0.80	0.00	0.00	0.01	1.00	Micritic magnesian calcite, partially recrystallised to microsparrite
11	5.84	48.68	0.00	0.56	0.00	44.92	100.00	0.14	0.85	0.00	0.00	0.01	1.00	Micritic magnesian calcite, partially recrystallised to microsparrite
12	8.06	46.22	0.00	0.19	0.25	45.28	100.00	0.19	0.80	0.00	0.00	0.00	1.00	Micritic magnesian calcite, partially recrystallised to microsparrite
13	6.53	48.18	0.00	0.00	0.25	45.04	100.00	0.16	0.84	0.00	0.00	0.00	1.00	Micritic magnesian calcite, partially recrystallised to microsparrite

Note: ******Analytical totals were low (<90%) because the cements were very microporous. Therefore all data were normalised to 100%*

Table 3 (continued). Electron microprobe analyses of carbonate cements in sample HG2 STN 46C.

No.	WEIGHT % OXIDE (normalised)							IONIC RATIO [normalised to 3 [O]]						COMMENTS
	MgO	CaO	MnO	FeO	SrO	CO_2 (calc)	*Total wt%	Mg^{2+}	Ca^{2+}	Mn^{2+}	Fe^{2+}	Sr^{2+}	CO_3^{2-}	
14	6.89	47.59	0.00	0.17	0.27	45.08	100.00	0.17	0.83	0.00	0.00	0.00	1.00	Micritic magnesian calcite, partially recrystallised to microsparrite
15	0.00	54.91	0.00	0.23	1.14	43.71	100.00	0.00	0.99	0.00	0.00	0.01	1.00	Aragonite pore-filling cement
16	0.00	54.71	0.00	0.17	1.47	43.65	100.00	0.00	0.98	0.00	0.00	0.01	1.00	Aragonite pore-filling cement
17	0.00	55.06	0.00	0.00	1.22	43.72	100.00	0.00	0.99	0.00	0.00	0.01	1.00	Aragonite pore-filling cement
18	0.00	54.61	0.00	0.21	1.55	43.63	100.00	0.00	0.98	0.00	0.00	0.02	1.00	Aragonite pore-filling cement
19	0.00	54.91	0.00	0.19	1.20	43.70	100.00	0.00	0.99	0.00	0.00	0.01	1.00	Aragonite pore-filling cement
20	1.20	53.21	0.00	0.31	1.44	43.85	100.00	0.03	0.95	0.00	0.00	0.01	1.00	Aragonite pore-filling cement
21	0.00	54.99	0.00	0.15	1.13	43.72	100.00	0.00	0.99	0.00	0.00	0.01	1.00	Aragonite pore-filling cement
22	0.39	53.89	0.00	0.40	1.66	43.66	100.00	0.01	0.97	0.00	0.01	0.02	1.00	Aragonite pore-filling cement
23	0.00	54.57	0.00	0.00	1.84	43.59	100.00	0.00	0.98	0.00	0.00	0.02	1.00	Aragonite pore-filling cement
24	0.00	54.17	0.00	0.33	1.96	43.54	100.00	0.00	0.98	0.00	0.00	0.02	1.00	Aragonite pore-filling cement
25	0.00	55.91	0.00	0.00	0.15	43.93	100.00	0.00	1.00	0.00	0.00	0.00	1.00	Aragonite shell
26	0.00	55.63	0.00	0.00	0.51	43.86	100.00	0.00	1.00	0.00	0.00	0.00	1.00	Aragonite shell
27	0.00	55.60	0.00	0.00	0.55	43.85	100.00	0.00	0.99	0.00	0.00	0.01	1.00	Aragonite shell
28	0.00	55.57	0.00	0.00	0.59	43.85	100.00	0.00	0.99	0.00	0.00	0.01	1.00	Aragonite shell
29	0.00	55.70	0.00	0.00	0.42	43.88	100.00	0.00	1.00	0.00	0.00	0.00	1.00	Aragonite shell
30	0.00	55.10	0.00	0.00	1.18	43.73	100.00	0.00	0.99	0.00	0.00	0.01	1.00	Aragonite cement overgrowth on shell
31	0.00	54.98	0.00	0.00	1.32	43.70	100.00	0.00	0.99	0.00	0.00	0.01	1.00	Aragonite cement overgrowth on shell
32	0.00	54.94	0.00	0.00	1.37	43.69	100.00	0.00	0.99	0.00	0.00	0.01	1.00	Aragonite cement overgrowth on shell
33	0.00	55.16	0.00	0.00	1.10	43.74	100.00	0.00	0.99	0.00	0.00	0.01	1.00	Aragonite cement overgrowth on shell
34	0.00	54.82	0.00	0.00	1.52	43.66	100.00	0.00	0.99	0.00	0.00	0.01	1.00	Aragonite cement overgrowth on shell

Note: **Analytical totals were low (<95%) because the cements were very microporous. Therefore all data were normalised to 100%*

Table 3 (continued). Electron microprobe analyses of carbonate cements in sample HG2 STN 46C.

No.	WEIGHT % OXIDE (normalised)							IONIC RATIO [normalised to 3 [O]						COMMENTS
	MgO	CaO	MnO	FeO	SrO	CO_2 (calc)	*Total wt%	Mg^{2+}	Ca^{2+}	Mn^{2+}	Fe^{2+}	Sr^{2+}	CO_3^{2-}	
35	0.00	54.70	0.00	0.00	1.67	43.63	100.00	0.00	0.98	0.00	0.00	0.02	1.00	Aragonite cement overgrowth on shell
36	0.00	54.94	0.00	0.00	1.37	43.69	100.00	0.00	0.99	0.00	0.00	0.01	1.00	Aragonite cement overgrowth on shell
37	0.00	54.79	0.00	0.00	1.56	43.65	100.00	0.00	0.98	0.00	0.00	0.02	1.00	Aragonite cement overgrowth on shell
38	2.06	53.43	0.00	0.00	0.24	44.27	100.00	0.05	0.95	0.00	0.00	0.00	1.00	Coarse magnesium calcite
39	1.93	53.52	0.00	0.00	0.31	44.23	100.00	0.05	0.95	0.00	0.00	0.00	1.00	Coarse magnesium calcite
40	2.13	53.24	0.00	0.00	0.37	44.26	100.00	0.05	0.94	0.00	0.00	0.00	1.00	Coarse magnesium calcite
41	1.87	53.62	0.00	0.00	0.27	44.23	100.00	0.05	0.95	0.00	0.00	0.00	1.00	Coarse magnesium calcite
42	1.98	53.46	0.00	0.00	0.33	44.24	100.00	0.05	0.95	0.00	0.00	0.00	1.00	Coarse magnesium calcite
43	2.01	53.41	0.00	0.00	0.33	44.24	100.00	0.05	0.95	0.00	0.00	0.00	1.00	Coarse magnesium calcite

Note: *****_Analytical totals were low (<95%) because the cements were very microporous. Therefore all data were normalised to 100%_

3.3 SAMPLE HG3 STN 42B

Sample HG3 STN 42B comprised a series of fragments of dark grey to light brownish grey carbonate-cemented fine sandstone and siltstone ranging in size from 5 mm to 70 mm diameter. The fragments were typically irregular in form, including lenticular, platy, branching and elongate forms. Some of these may represent carbonate-cemented sediment-filled burrow structures (Figure 21). Most of the clasts appear to be abraded and moderately well-rounded. Their surfaces are commonly bored by marine organisms and some of the clast surfaces are weakly oxidised and stained by orange-brown films of iron oxyhydroxide.

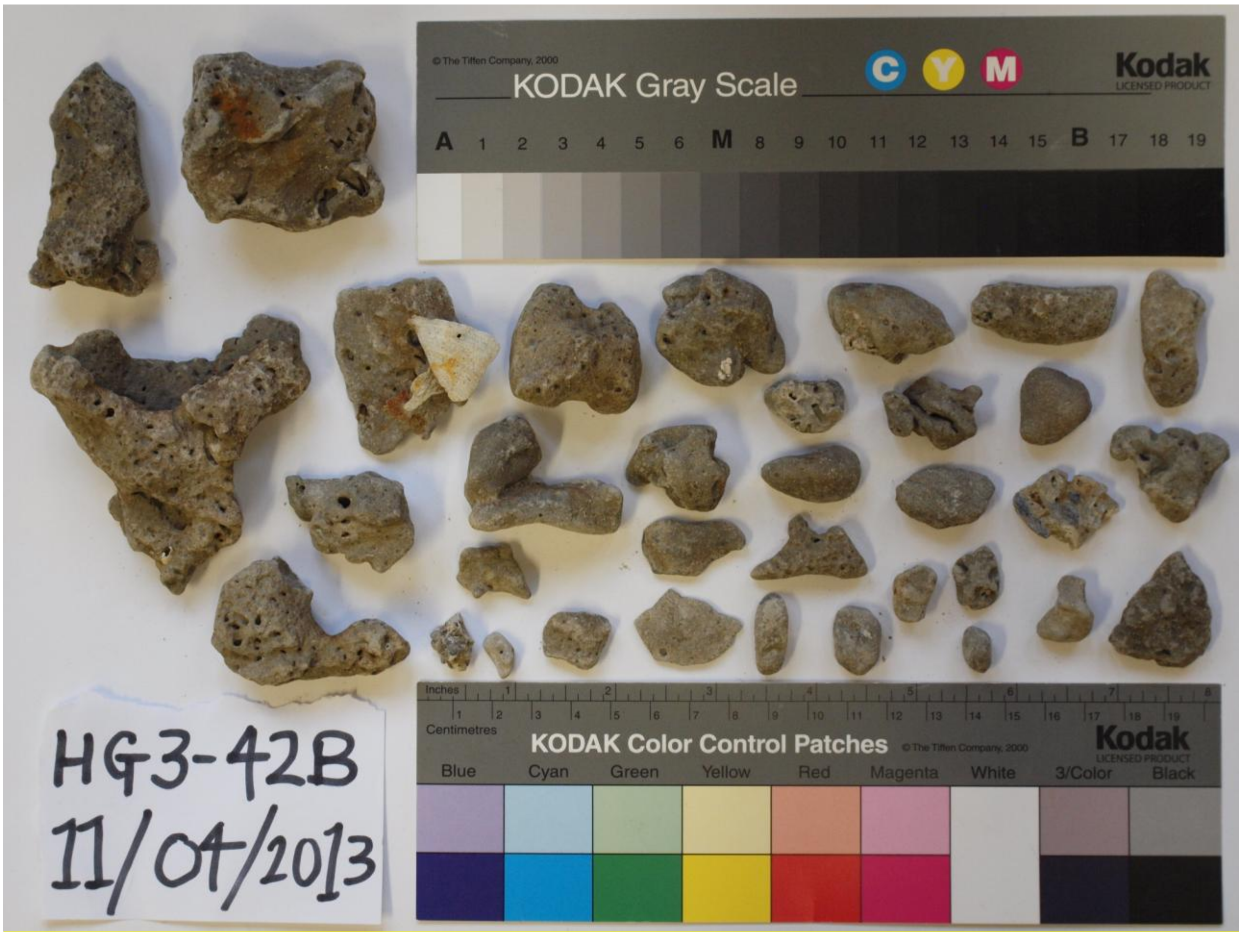

Figure 21. Photograph showing the range of shapes and sizes of the fragments of carbonate cemented sandstone and siltstone in sample HG3 STN 42B. Many fragments are moderately well rounded, and most display open borings by marine organisms.

The polished section prepared through a fragment of HG3 STN 42B is shown in Figure 22. In section this fragment was seen to have a disturbed fabric comprising convoluted laminae of weakly-cemented microporous sandstone preserved or isolated within more tightly-cemented sandstone. Detailed petrographic examination shows that the well-cemented sandstone has also been suffered synsedimentary disruption with localised brecciation and re-cementation of the fragmented rock (Figure 23). This clast is a fine grained sandstone with detrital components comprising mainly of angular to sub-angular sand-grade quartz, with minor K-feldspar, plagioclase and occasional muscovite. Minor clay-grade illite, kaolinite and possibly chlorite are also present. The matrix of the sandstone is predominantly micritic high-magnesian calcite. Detrital quartz grains locally display minor etching or corrosion. The detrital muscovite has been altered with leaching and exfoliation of the grains along their basal cleavage. The mica alteration occurred prior to cementation since the micritic magnesian calcite enclosed exfoliated grains and penetrates along the exfoliated mica cleavage (illustrated in Figure 24).

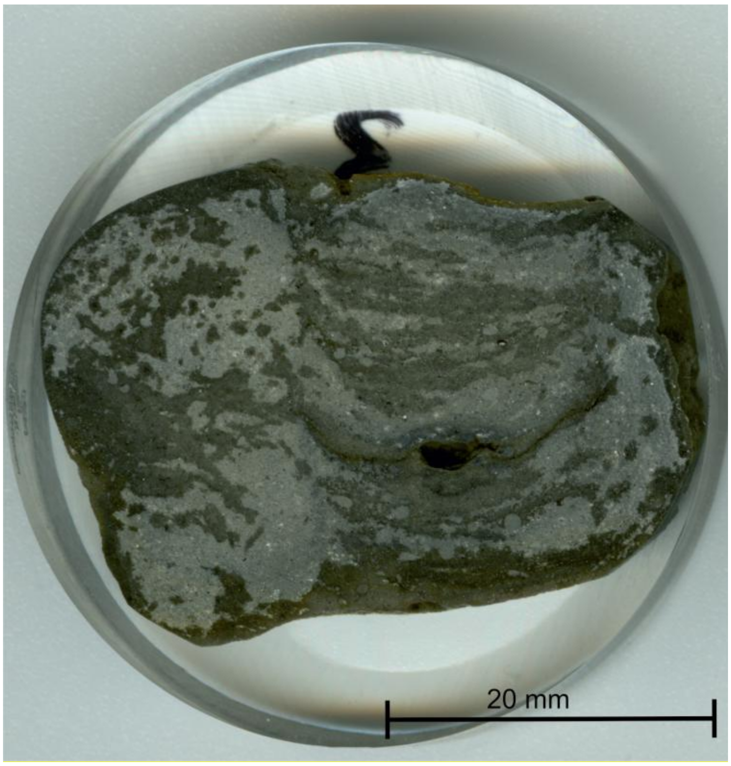

Figure 22. Polished section through a fragment of dominantly magnesian calcite-cemented fine sandstone. It shows contorted laminae of weakly-cemented microporous sandstone (darker areas) and patches of more tightly-cemented sandstone (light grey). A large burrow with iron oxyhydroxide stained surfaces can be seen near the centre of the of the section. Sample HG3 STN 42B.

The tightly-cemented and weakly-cemented sandstone both display very uncompacted grain fabric with only minimal, simple grain contacts (Figure 23 to Figure 26). The grains appear to ‘float’ within the micrite matrix, indicating that cementation occurred at or close to sediment surface and before significant sediment burial. In polished section, the well-cemented parts of the sandstone also display, relatively large intergranular areas 100-200 μm in diameter that are occupied by micritic calcite cement (e.g. Figure 25). These are ‘oversized’ compared to the detrital silicate grain size of the rock, and represent pelloidal grains composed of micritic high magnesian calcite with dispersed fine quartz silt and clay minerals. These pelloidal grains are generally rounded, and encased within subsequent pore-filling micrite, and some may possibly be faecal pellets suggesting that the micritic carbonate precipitation was syndepositional, and was being bioturbated and reworked by benthic marine organisms during deposition.

The micritic magnesian calcite in both the tightly-cemented areas and very porous weakly cemented-areas is very similar in character. It typically comprises small ‘globular’ aggregates of micritic high-magnesian calcite up to 10-50 μm in diameter, often surrounded by a rim of coarser microsparry magnesian calcite (Figure 27). Within the more porous sandstone, this micritic magnesian calcite forms colloform fringes coating and encrusting the detrital sand grains (Figure 26), and weakly binding the sand grains together. The microsparry calcite overgrowth on the micritic carbonate locally developed a more complex fabric, with colloform banding consisting of an initial layer of low-magnesian calcite coated by a subsequent layer of high-magnesian calcite (Figure 28). Some of the micritic magnesian calcite is also recrystallised and patchily replaced and overprinted by microcrystalline low-magnesian calcite (Figure 28).

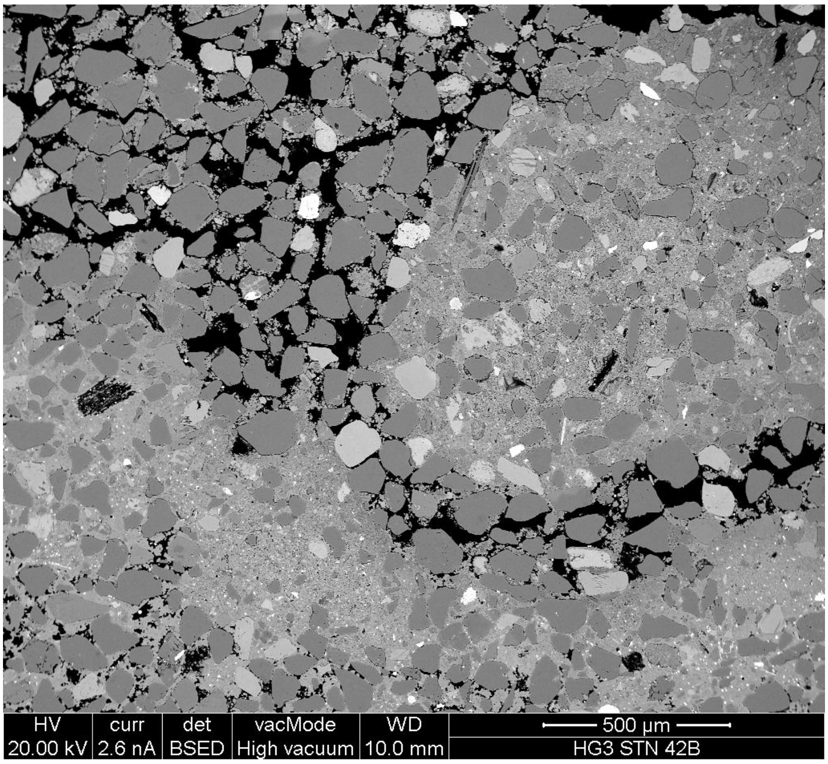

Figure 23. BSEM photomicrograph of fragmented and brecciated sandstone cemented by micritic magnesian calcite, with weakly-cemented porous sand filling between the fragments of cemented rock. Sample HG3 STN 42B.

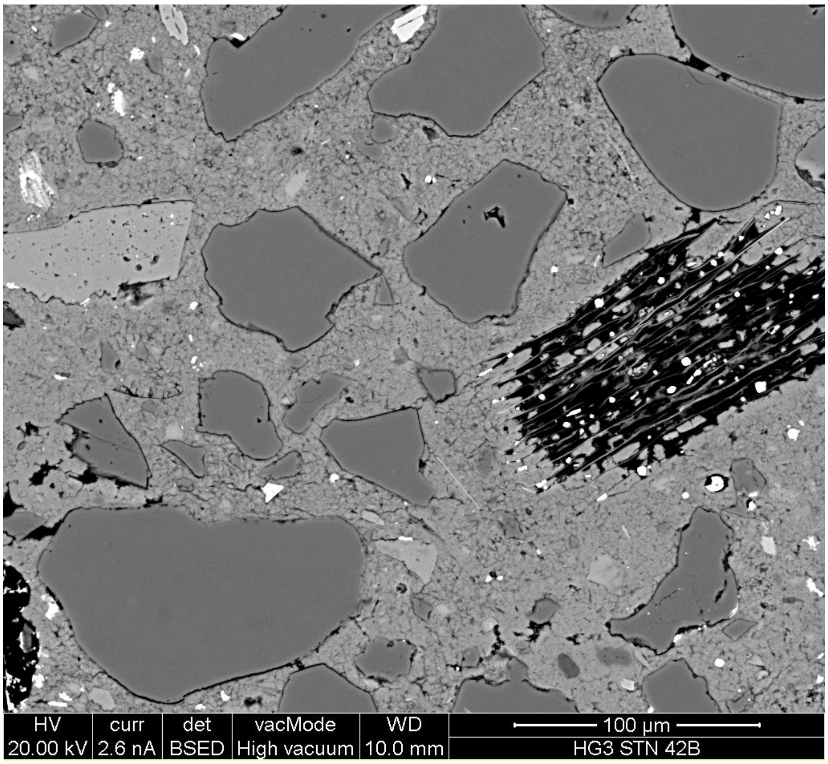

Figure 24. BSEM photomicrograph showing uncompacted grain fabric of detrital quartz (mid-grey) ‘floating’ in a matrix of micritic magnesian calcite cement (light-grey). A detrital muscovite grain has been exfoliated and subsequently enclosed within the calcite. Pyrite microcrystals (white) have precipitated along the exfoliated cleavage. Sample HG3 STN 42B.

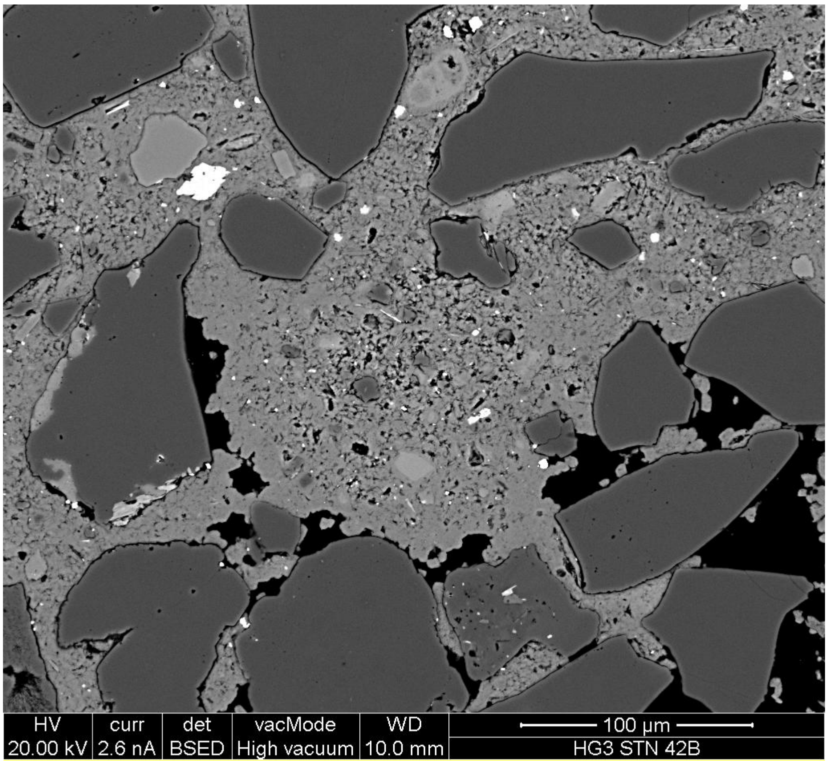

Figure 25. BSEM photomicrograph showing uncompacted grain fabric with detrital quartz (dark grey) 'floating' in a matrix of micritic magnesian calcite cement (light grey). The 'oversized' area of micritic calcite in the centre of the image represents pelloidal carbonate grain. Sample HG3 STN 42B.

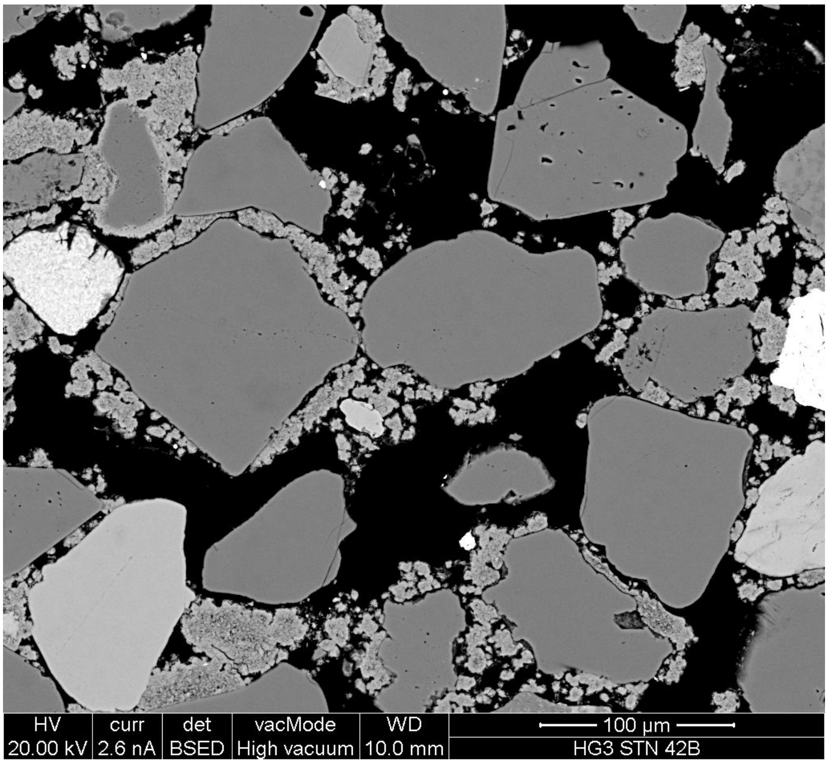

Figure 26. BSEM photomicrograph of a porous sandstone region, showing uncompacted detrital grains of quartz (mid-grey) and K-feldspar (white), weakly cemented by thin colloform fringes of micritic magnesian calcite. Sample HG3 STN 42B.

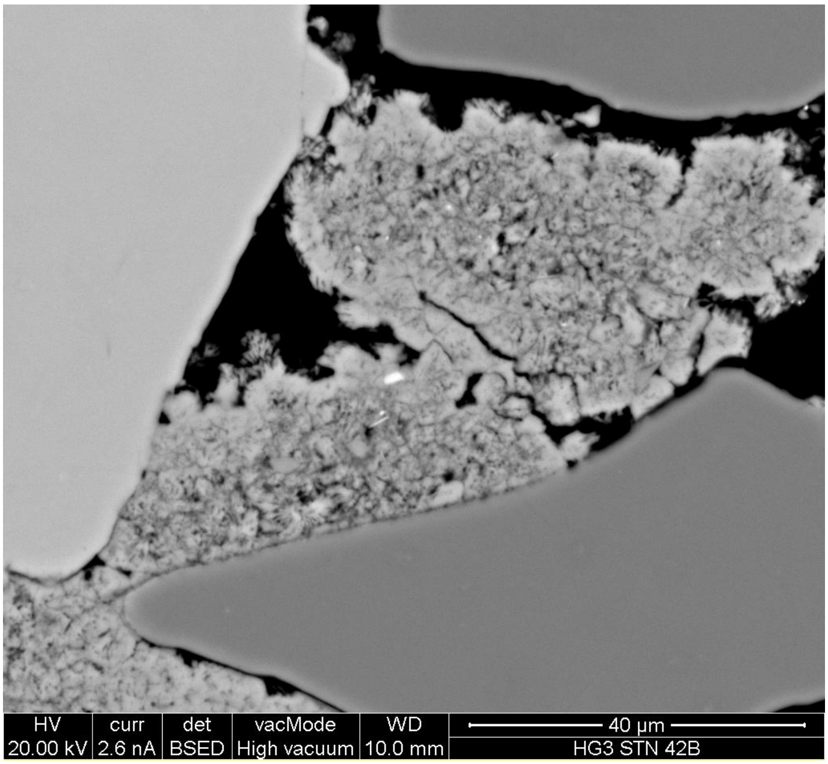

Figure 27. BSEM photomicrograph showing typical micritic carbonate cement comprising small ‘globular’ aggregates of micritic high-magnesian calcite surrounded by a rim of coarser microsparry magnesian calcite. Sample HG3 STN 42B.

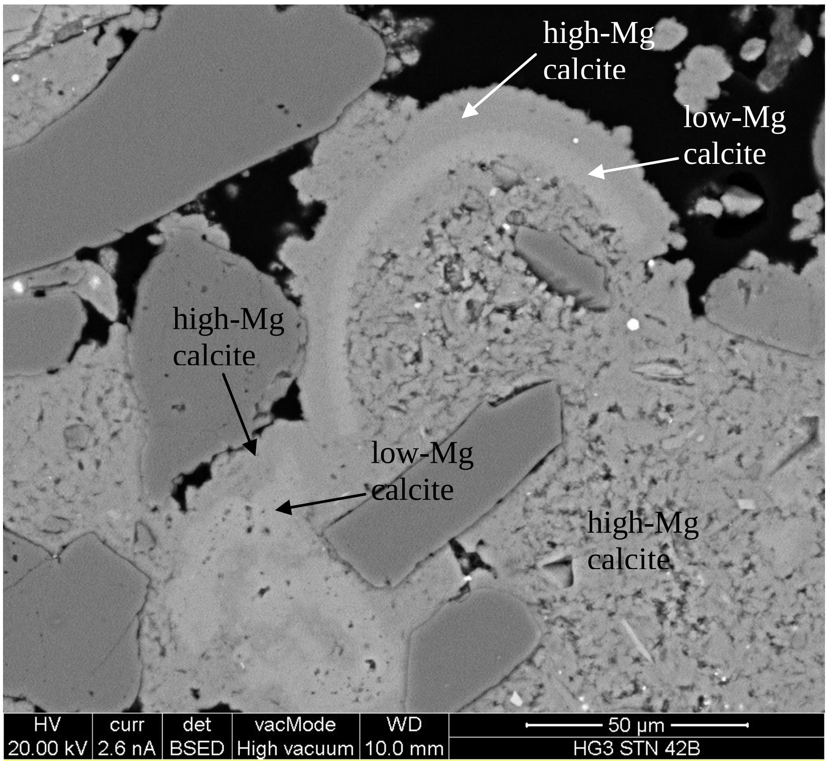

Figure 28. BSEM photomicrograph showing ‘globular’ aggregates or ‘pelloids’ of micritic high-magnesian calcite surrounded by a microcolloform rim of later calcite cement comprising an initial band of low-magnesian calcite subsequently overgrown by high-magnesian calcite. Some ‘globular’ aggregate cores display patchy replacement of high-magnesian calcite by microsparry low-magnesian calcite. Sample HG3 STN 42B.

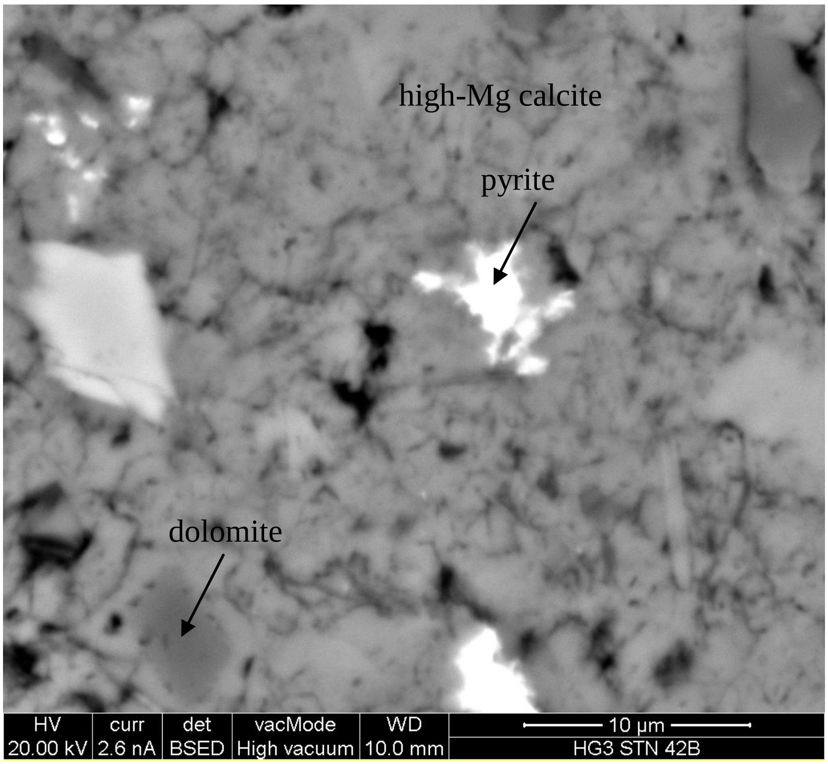

Figure 29. BSEM photomicrograph showing fine microstructure within the micritic high-magnesian calcite matrix. The micritic carbonate comprises small spheroidal or 'framboidal' aggregates of fibrous microcrystals, often nucleated around a 'hollow core'. Pyrite has precipitated within the interstitial microporosity, and very small dolomite crystals are encased within the micritic calcite. Sample HG3 STN 42B.

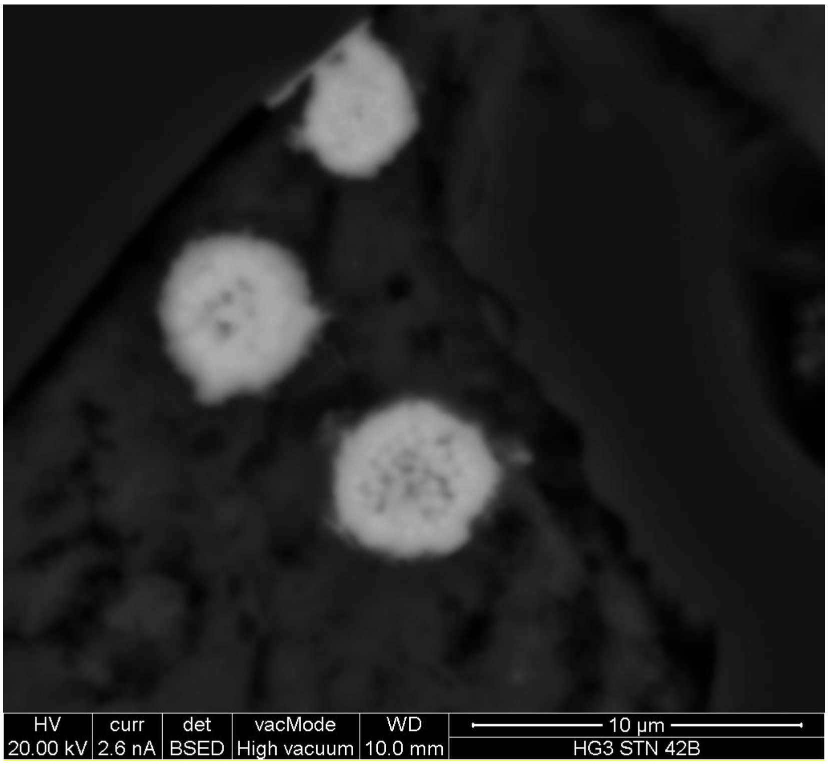

Figure 30. BSEM photomicrograph showing framboidal pyrite within a micritic high-magnesian calcite matrix. HG3 STN 42B.

High-resolution BSEM observations of the micritic high magnesian calcite matrix revealed an even finer microstructure comprised of fine spheroidal or ‘framboidal’ aggregates of fibrous microcrystals of high-magnesian, often nucleated around a ‘hollow centre (Figure 29). Similar textures have been described previously from dolomitic MDAC from the Mid Irish Sea (Milodowski et al., 2009), and closely resemble mineralised and fossilised bacterial cell fabrics described in the literature (e.g. Martill and Wilby, 1994; Wilby and Whyte, 1995). Therefore this microfabric might indicate that the magnesian calcite seen in this sample from the Braemar Pockmark may also be similarly of microbial origin.

A minor amount of dolomite is closely associated with the micritic magnesian calcite. The dolomite occurs as tiny idiomorphic (i.e. euhedral) rhomb crystals disseminated within the micrite matrix. Its position within the sequence of carbonate cements is unclear. It may partially replace some of the high magnesian calcite but is also seen to be encrusted by subsequent high-magnesian calcite (Figure 29).

Authigenic pyrite is common in this sample, and is closely associated with the micritic magnesian calcite. Pyrite occurs as minor microcrystalline fills within the interstitial microporosity in the micrite (Figure 29). It also occurs as framboidal pyrite (Figure 30), which is characteristic of low-temperature and early diagenetic sulphide formation within the sulphide reduction zone of marine sediments (Berner, 1969; 1980; Rickard, 1970; 1975; Sweeney & Kaplan, 1973). Some of this pyrite has been oxidised to iron oxide or oxyhydroxide near the surfaces of the carbonate-cemented sandstone ‘clast’. This secondary iron oxide accounts for the orange and red-brown staining seen on these carbonate-cemented rock fragments.

Electron microprobe analyses of the calcite and dolomite cement are presented in Table 4. These data are summarised in Figure 31 in terms of molar proportions of end-member $CaCO_3$-$MgCO_3$-$FeCO_3$. These data show that the early ‘globular, micritic magnesian calcite aggregates and the colloform magnesian calcite overgrowth cements are high-magnesian calcites with most analyses showing between 18 to 24 mole % $MgCO_3$ in solid-solution (Figure 31) within the calcite lattice (i.e. the structural formula of the calcite can be represented as $Ca_{0.76\text{-}0.82}Mg_{0.24\text{-}0.18}CO_3$). Most analyses of the micritic calcite cluster towards the higher end of this range and are similar to the micritic calcite cement found in the other Braemar Pockmark samples. However, SEM-EDXA observations indicate that the recrystallisation of the micrite to coarser microsparry calcite and colloform microsparry calcite cement overgrowths produced a relatively-low magnesium calcite (Figure 31) with between 1-5 mole % $MgCO_3$ in sold solution (i.e. $Ca_{0.95\text{-}0.99}Mg_{0.05\text{-}0.01}CO_3$). The recrystallisation of the early-formed high-magnesian calcite and its partial replacement by a less magnesian calcite will potentially have liberated magnesium into the porewaters of the sediment. This may then have promoted the formation of the small amount of dolomite closely associated with these calcite cements.

The EPMA data show that the dolomite associated with the micritic calcite is calcium-rich (composition of $Ca_{0.53\text{-}0.55}Mg_{0.47\text{-}0.45}CO_3$), with 3-5 mole% Ca in excess of the ideal stoichiometry for dolomite $Ca_{0.5}Mg_{0.5}CO_3$. This is very similar to the excess Ca dolomites (average composition $Ca_{0.53}Mg_{0.47}CO_3$) described by Jensen et al. (1992) from MDAC deposits in the Kattegat off the coast of Denmark. The presence of a significant excess in Ca in dolomite at low temperature may indicate that the dolomite is relatively poorly ordered and/or metastable, and may have precipitated rapidly (Vahrenkamp and Swart, 1994) possibly forming via a “protodolomite” precursor (cf. Deer et al., 1992).

The sequence of sedimentary and post-depositional diagenetic events recorded from sample HG3 STN 42B can be summarised as follows:

1. Deposition of fine sand and silt sediment;
2. Microbial precipitation of micritic high-magnesian calcite within the near-surface of the sediment, simultaneously accompanied by the precipitation of authigenic pyrite associated with iron and sulphate reduction in sediment.

3. Syndepositional bioturbation and reworking of the micritic magnesian calcite-rich sand prior to lithification;
4. Ongoing microbial precipitation of micritic high-magnesian calcite and partial lithification, followed by disruptive brecciation of more lithified parts of the sandstone. This disruption may possibly be the result of gas build-up within the sediment and its sudden release;
5. Further microbial precipitation of micritic high-magnesian calcite and lithification;
6. Partial recrystallisation, replacement and overgrowth of micritic high-magnesian calcite by lower magnesian calcite. The magnesium released to the porewaters during this process may have given rise to very minor dolomitisation of the early micritic calcite;
7. Erosion of the lithified carbonate-cemented sandstone, with abrasion of eroded clasts. Boring of the clast surfaces by marine biota, and oxidation of pyrite near the clast surface. This indicates that the sea bed environment was oxic at this time.

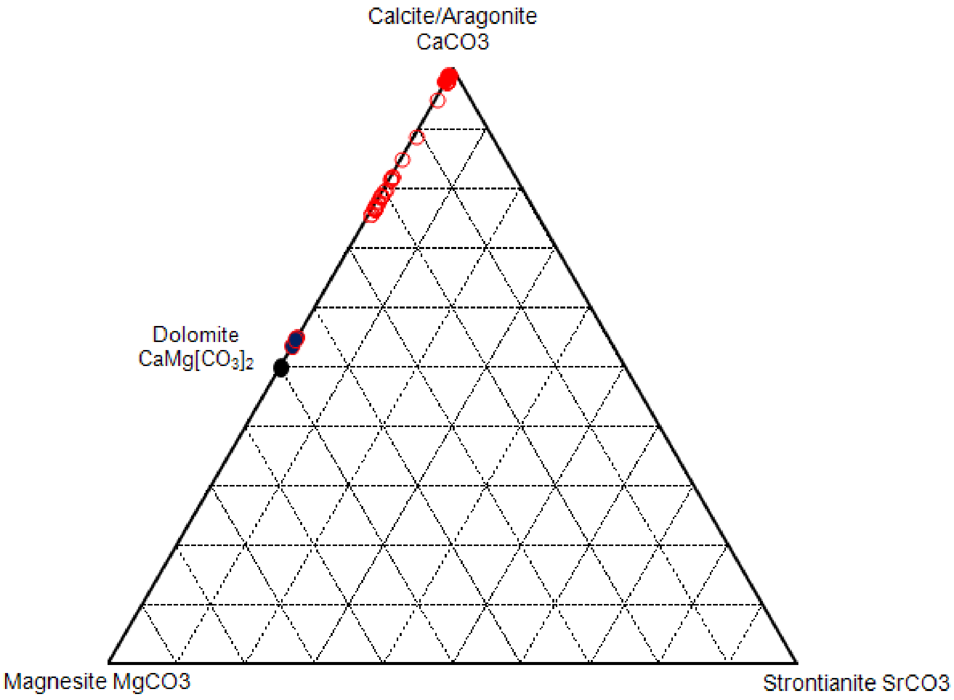

Figure 31. $CaCO_3$-$MgCO_3$-$SrCO_3$ molar ratio plot illustrating the composition of the micritic and colloform high-magnesian calcite (open red circles), recrystallised micritic calcite (solid red circles) and dolomite microspar (solid blue circles). MDAC sample HG3 STN 42B, relative to end-member carbonate minerals.

Table 4. Electron microprobe analyses of carbonate cements in sample HG3 STN 42B.

No.	WEIGHT % OXIDE (normalised)							IONIC RATIO [normalised to 3 [O]						COMMENTS
	MgO	CaO	MnO	FeO	SrO	CO_2 (calc)	*Total wt%	Mg^{2+}	Ca^{2+}	Mn^{2+}	Fe^{2+}	Sr^{2+}	CO_3^{2-}	
1	9.70	44.24	0.00	0.22	0.28	45.56	100.00	0.23	0.76	0.00	0.00	0.00	1.00	Micritic high magnesian calcite
2	8.82	45.65	0.00	0.06	0.00	45.48	100.00	0.21	0.79	0.00	0.00	0.00	1.00	Micritic high magnesian calcite
3	9.84	44.13	0.00	0.24	0.20	45.59	100.00	0.24	0.76	0.00	0.00	0.00	1.00	Micritic high magnesian calcite
4	9.79	44.14	0.00	0.17	0.33	45.57	100.00	0.23	0.76	0.00	0.00	0.00	1.00	Micritic high magnesian calcite
5	9.04	45.20	0.00	0.27	0.00	45.49	100.00	0.22	0.78	0.00	0.00	0.00	1.00	Micritic high magnesian calcite
6	9.45	44.42	0.00	0.41	0.22	45.51	100.00	0.23	0.77	0.00	0.01	0.00	1.00	Micritic high magnesian calcite
7	9.75	44.05	0.00	0.62	0.00	45.58	100.00	0.23	0.76	0.00	0.01	0.00	1.00	Micritic high magnesian calcite
8	8.53	45.26	0.00	0.54	0.37	45.31	100.00	0.21	0.78	0.00	0.01	0.00	1.00	Micritic high magnesian calcite
9	9.96	43.49	0.00	0.61	0.39	45.54	100.00	0.24	0.75	0.00	0.01	0.00	1.00	Micritic high magnesian calcite
10	9.61	44.17	0.00	0.56	0.11	45.54	100.00	0.23	0.76	0.00	0.01	0.00	1.00	Micritic high magnesian calcite
11	6.02	48.66	0.00	0.35	0.00	44.97	100.00	0.15	0.85	0.00	0.00	0.00	1.00	Micritic high magnesian calcite
12	9.26	43.44	0.00	1.93	0.00	45.37	100.00	0.22	0.75	0.00	0.03	0.00	1.00	Micritic high magnesian calcite
13	9.10	44.79	0.00	0.64	0.00	45.47	100.00	0.22	0.77	0.00	0.01	0.00	1.00	Micritic high magnesian calcite
14	4.31	50.72	0.00	0.30	0.00	44.68	100.00	0.11	0.89	0.00	0.00	0.00	1.00	Micritic high magnesian calcite
15	8.85	45.05	0.00	0.67	0.00	45.42	100.00	0.21	0.78	0.00	0.01	0.00	1.00	Micritic high magnesian calcite
16	7.64	46.50	0.00	0.65	0.00	45.22	100.00	0.18	0.81	0.00	0.01	0.00	1.00	Micritic high magnesian calcite
17	7.53	46.10	0.00	1.22	0.00	45.14	100.00	0.18	0.80	0.00	0.02	0.00	1.00	Micritic high magnesian calcite
18	19.25	32.96	0.00	0.57	0.00	47.22	100.00	0.45	0.55	0.00	0.01	0.00	1.00	Dolomite microspar within micritic calcite
19	19.79	32.03	0.00	0.90	0.00	47.28	100.00	0.46	0.53	0.00	0.01	0.00	1.00	Dolomite microspar within micritic calcite
20	19.30	32.70	0.00	0.79	0.00	47.21	100.00	0.45	0.54	0.00	0.01	0.00	1.00	Dolomite microspar within micritic calcite

Note: **Analytical totals were low (<90%) because the cements were very microporous. Therefore all data were normalised to 100%*

Table 4 (continued). **Electron microprobe analyses of carbonate cements in sample HG3 STN 42B.**

No.	WEIGHT % OXIDE (normalised)							IONIC RATIO [normalised to 3 [O]						COMMENTS
	MgO	**CaO**	**MnO**	**FeO**	**SrO**	**CO_2 (calc)**	***Total wt%**	**Mg^{2+}**	**Ca^{2+}**	**Mn^{2+}**	**Fe^{2+}**	**Sr^{2+}**	**CO_3^{2-}**	
21	8.66	45.36	0.00	0.58	0.00	45.40	100.00	0.21	0.78	0.00	0.01	0.00	1.00	Colloform high magnesian calcite
22	8.40	46.20	0.00	0.00	0.00	45.41	100.00	0.20	0.80	0.00	0.00	0.00	1.00	Colloform high magnesian calcite
23	8.38	45.95	0.00	0.29	0.00	45.38	100.00	0.20	0.79	0.00	0.00	0.00	1.00	Colloform high magnesian calcite
24	7.61	47.12	0.00	0.00	0.00	45.27	100.00	0.18	0.82	0.00	0.00	0.00	1.00	Colloform high magnesian calcite
25	7.56	47.18	0.00	0.00	0.00	45.26	100.00	0.18	0.82	0.00	0.00	0.00	1.00	Colloform high magnesian calcite
26	0.68	55.24	0.00	0.00	0.00	44.08	100.00	0.02	0.98	0.00	0.00	0.00	1.00	Recrystallised colloform low-magnesian calcite
27	0.61	55.32	0.00	0.00	0.00	44.07	100.00	0.02	0.98	0.00	0.00	0.00	1.00	Recrystallised colloform low-magnesian calcite
28	0.81	55.09	0.00	0.00	0.00	44.10	100.00	0.02	0.98	0.00	0.00	0.00	1.00	Recrystallised colloform low-magnesian calcite
29	2.13	53.54	0.00	0.00	0.00	44.33	100.00	0.05	0.95	0.00	0.00	0.00	1.00	Recrystallised colloform low-magnesian calcite
30	0.66	55.26	0.00	0.00	0.00	44.08	100.00	0.02	0.98	0.00	0.00	0.00	1.00	Recrystallised colloform low-magnesian calcite
31	8.68	45.59	0.00	0.30	0.00	45.43	100.00	0.21	0.79	0.00	0.00	0.00	1.00	Colloform high magnesian calcite
32	7.67	47.04	0.00	0.00	0.00	45.28	100.00	0.18	0.82	0.00	0.00	0.00	1.00	Colloform high magnesian calcite
33	8.75	45.78	0.00	0.00	0.00	45.47	100.00	0.21	0.79	0.00	0.00	0.00	1.00	Colloform high magnesian calcite
34	9.41	44.78	0.00	0.26	0.00	45.56	100.00	0.23	0.77	0.00	0.00	0.00	1.00	Colloform high magnesian calcite
35	9.44	44.12	0.00	0.93	0.00	45.50	100.00	0.23	0.76	0.00	0.01	0.00	1.00	Colloform high magnesian calcite
36	0.77	55.13	0.00	0.00	0.00	44.10	100.00	0.02	0.98	0.00	0.00	0.00	1.00	Colloform low-magnesian calcite
37	0.85	55.04	0.00	0.00	0.00	44.11	100.00	0.02	0.98	0.00	0.00	0.00	1.00	Colloform low-magnesian calcite
38	0.54	55.41	0.00	0.00	0.00	44.06	100.00	0.01	0.99	0.00	0.00	0.00	1.00	Colloform low-magnesian calcite
39	0.80	55.10	0.00	0.00	0.00	44.10	100.00	0.02	0.98	0.00	0.00	0.00	1.00	Colloform low-magnesian calcite
40	0.32	55.44	0.00	0.24	0.00	44.00	100.00	0.01	0.99	0.00	0.00	0.00	1.00	Colloform low-magnesian calcite

***Note:* *Analytical totals were low (<95%) because the cements were very microporous. Therefore all data were normalised to 100%**

3.4 SAMPLE HG3 STN 42C

Sample HG3 STN 42C comprised a series of very well-rounded pebble-like clasts of light brownish grey carbonate-cemented fine sandstone ranging in size from 10 mm to 35 mm diameter (Figure 32). The fragments were seen to be pitted and bored by marine organisms. The features of this sample are very similar to those observed in HG3 STN 42B.

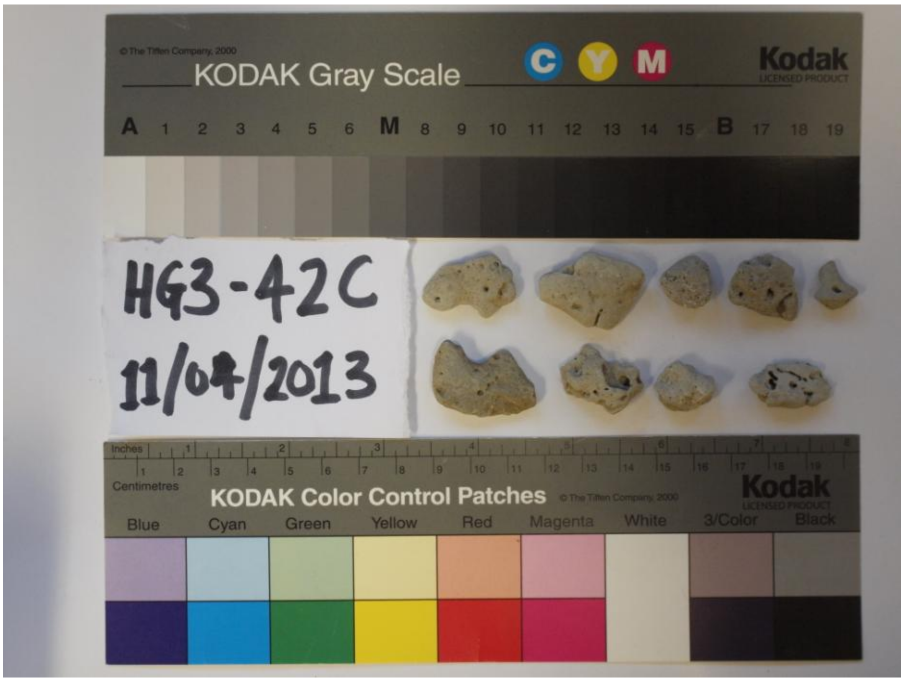

Figure 32. Photograph showing the range of shapes and sizes of the fragments of carbonate cemented sandstone in sample HG3 STN 42C. Many fragments are moderately well rounded, and most display open borings by marine organisms.

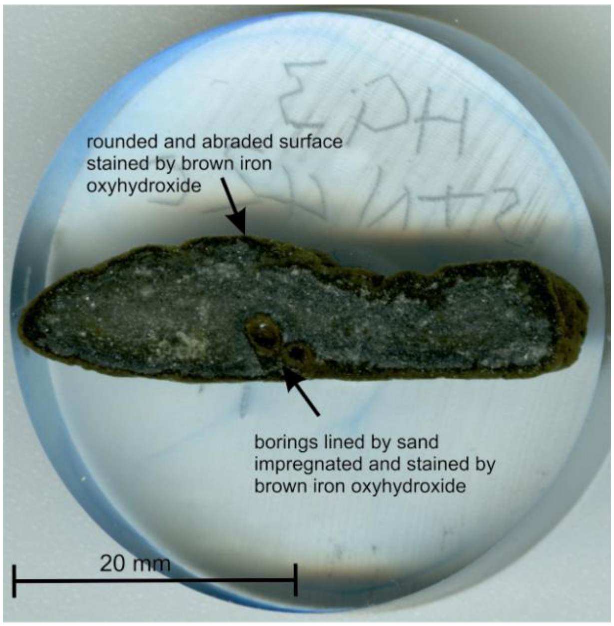

Figure 33. Polished section through a clast of magnesian calcite-cemented fine sandstone. It shows the outer edges of the clast are coated with sand stained by iron oxyhydroxide. Large borings produced by marine organisms are also evident. Sample HG3 STN 42B.

In polished section the carbonate cemented sandstone is seen to be dark grey (Figure 33). This is due to the presence of probable organic matter and abundant very fine-grained authigenic pyrite, disseminated throughout the matrix of the rock. The sandstone mineralogy and petrography of this sample are similar to that described from sample HG3 STN 42B (see Section 3.3). The rock is fine-grained sandstone, with sub-angular to angular detrital sand grains composed mainly of quartz, with subordinate detrital feldspar, and with a minor clay matrix composed of illite, kaolinite and possible chlorite (Figure 34). Rare rounded glauconite grains, coated in films of pyrite are also present. The clay mineral identification is based solely on BSEM-EDXA observations and would require detailed X-ray-diffraction analysis to positively identify the clay mineralogy. The sandstone is tightly-cemented by an intergranular matrix of micritic high-magnesian calcite (Figure 34). The rock has a very uncompacted grain fabric with only minimal and simple grain contacts (Figure 34), and detrital grains appear to ‘float’ within the micrite matrix, indicating that cementation occurred at or close to sediment surface and before sediment significant burial. As seen in sample HG3 STN 42B (see Section 3.3), are significant proportion of the micritic carbonate occupies over-sized volumes relative to the grain size of the detrital silicates, and represents micritic carbonate re-worked as pelloids. Some of these are probably faecal pellets.

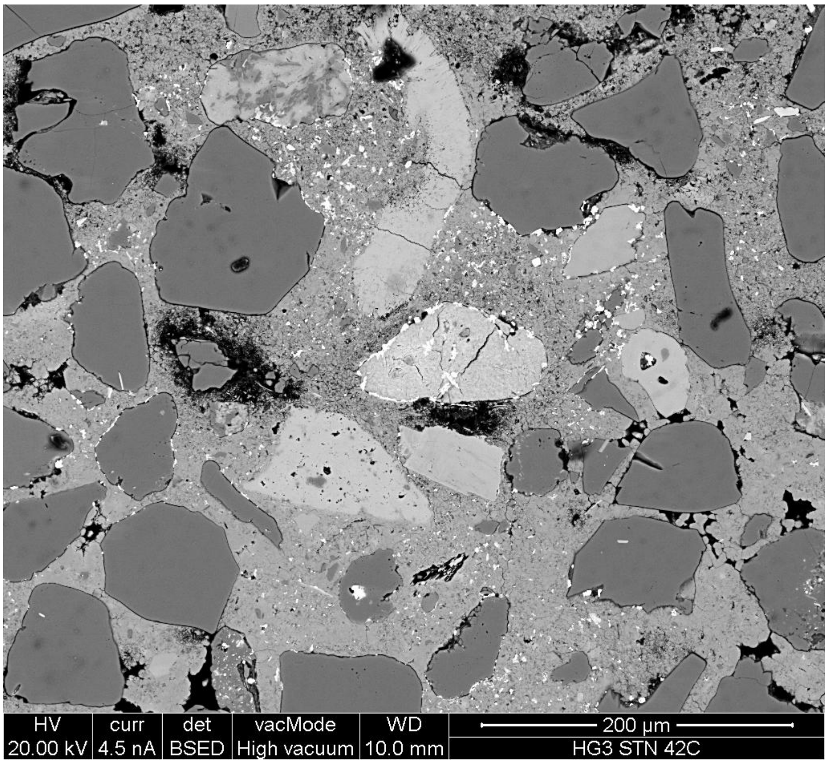

Figure 34. BSEM photomicrograph showing fine-grained sandstone composed of angular to sub-rounded grains of detrital quartz (darker-grey) and K-feldspar (light-grey) with an uncompacted fabric tightly-cemented by a micritic magnesian calcite matrix. Very fine-grained pyrite (white) is abundant, both as disseminations through the micrite matrix and as coatings on detrital grain surfaces. Sample HG3 STN 42C.

Pyrite is abundant throughout this sample. It occurs as finely disseminated pyrite similar to that described previously from sample HG3 STN 42B within the micritic matrix (see Section 3.3), or as films and coatings on detrital grains (Figure 34). Pyrite coatings also commonly delineate the ‘ghost’ outlines of micritic pelloidal grains (Figure 35). The coating of the detrital grains by films of pyrite and was subsequently enclosed within the micritic calcite cement, indicate that pyrite formed very early during the diagenesis of these rocks.

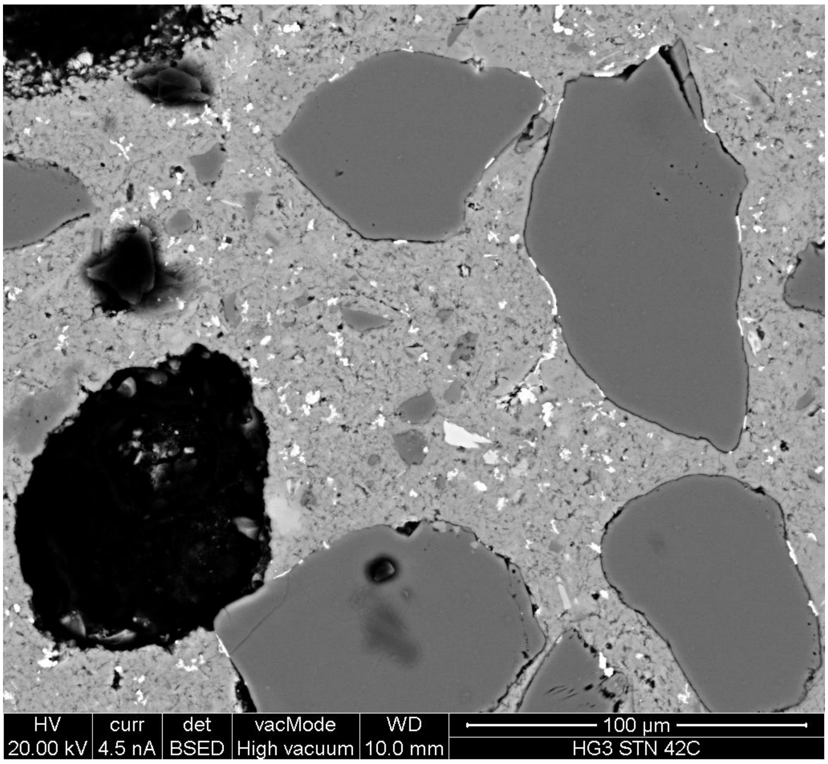

Figure 35. BSEM photomicrograph showing abundant fine grained pyrite (white) within the micritic matrix of the sandstone. In the centre of the image a fine 'fringe' of pyrite partly outlines the original grain boundary of an originally micritic carbonate pelloidal grain. Sample HG3 STN 42C.

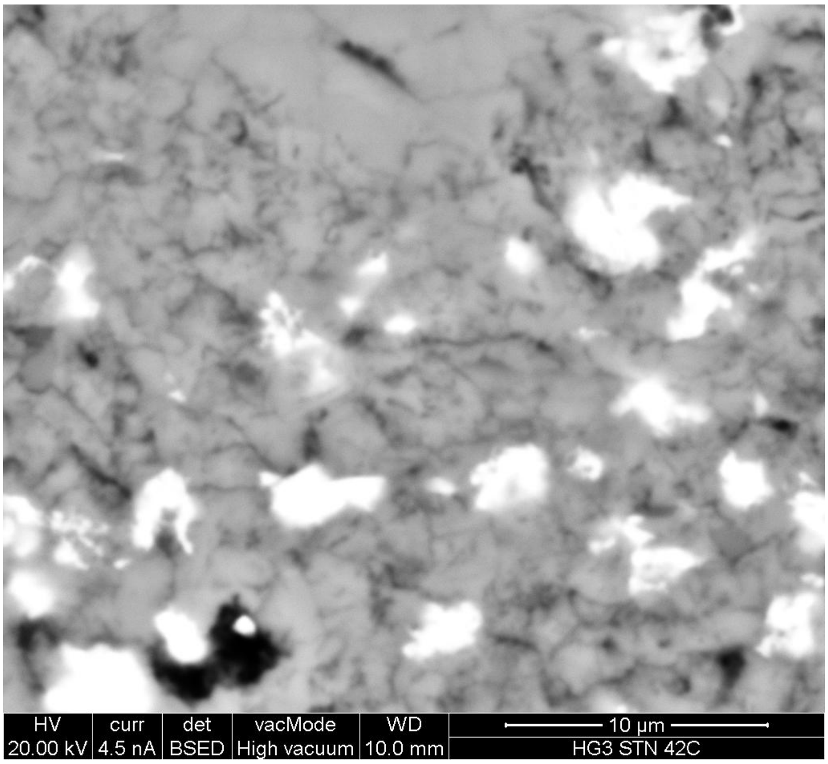

Figure 36. BSEM photomicrograph showing fine pyrite filling interstitial pores in micritic magnesian calcite. Small spheroidal or 'framboidal' aggregates of magnesian calcite consisting of fibrous microcrystals nucleated around a 'hollow core' can be seen in the lower right of the image. Sample HG3 STN 42C.

The micritic matrix is composed of very finely microcrystalline magnesian calcite. A spheroidal or 'framboidal' fabric consisting of fibrous microcrystals magnesian calcite nucleated around a 'hollow core' is locally preserved (Figure 35). This fabric is similar to that described from sample HG3 STN 42B and may be of microbial origin (see Section 3.3). EPMA analyses of the calcite are presented in Table 5 and are summarised in Figure 37. The magnesian calcite is very similar in composition to that described from the other samples studied. It is a high magnesian calcite with between 19-26 mole % $MgCO_3$ in solid-solution in the calcite lattice. Where minor recrystallisation to microsparry calcite has occurred the microsparry calcite is shown to have a lower magnesium content (about 9 mole % $MgCO_3$), as seen in the other samples studied from the Braemar Pockmark.

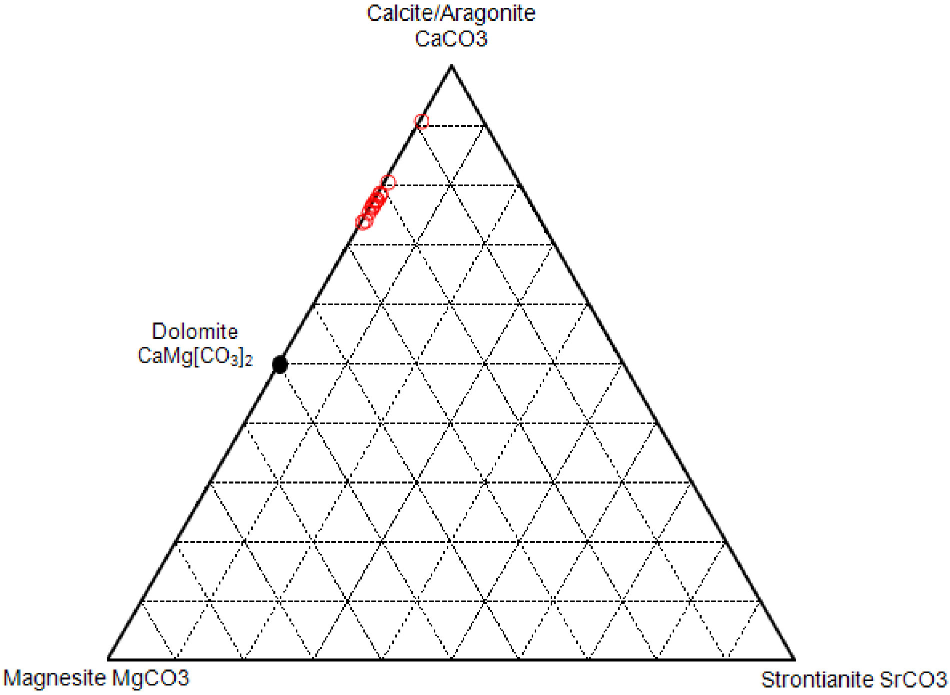

Figure 37. $CaCO_3$-$MgCO_3$-$SrCO_3$ molar ratio plot illustrating the composition of the micritic calcite cement (open red circles). MDAC sample HG3 STN 42C, relative to end-member carbonate minerals.

The sequence of sedimentary and post-depositional diagenetic events recorded from sample HG3 STN 42C can be summarised as follows:

1. Deposition of fine sand and silt sediment;
2. Microbial precipitation of micritic high-magnesian calcite within the near-surface of the sediment, and precipitation of authigenic pyrite associated with iron and sulphate reduction in sediment.
3. Syndepositional bioturbation and reworking associated with the production of pelloidal grains of micrite (possibly faecal pellets);
4. Ongoing microbial precipitation of micritic high-magnesian calcite and lithification, accompanied by further precipitation of authigenic pyrite;
5. Minor recrystallisation, replacement and overgrowth of micritic high-magnesian calcite by lower magnesian calcite;
6. Erosion and abrasion of eroded clasts. Boring of the clast surfaces by marine biota, and oxidation of pyrite near the clast surface.

Table 5. Electron microprobe analyses of carbonate cements in sample HG3 STN 42C.

No.	**WEIGHT % OXIDE (normalised)**							**IONIC RATIO [normalised to 3 [O]**						**COMMENTS**
	MgO	**CaO**	**MnO**	**FeO**	**SrO**	**CO_2 (calc)**	***Total wt%**	**Mg^{2+}**	**Ca^{2+}**	**Mn^{2+}**	**Fe^{2+}**	**Sr^{2+}**	**CO_3^{2-}**	
1	9.00	44.57	0.00	0.79	0.26	45.38	100.00	0.22	0.77	0.00	0.01	0.00	1.00	Micritic high magnesian calcite
2	9.51	41.48	0.00	3.56	0.23	45.21	100.00	0.23	0.72	0.00	0.05	0.00	1.00	Micritic high magnesian calcite
3	10.24	42.65	0.00	1.54	0.00	45.58	100.00	0.25	0.73	0.00	0.02	0.00	1.00	Micritic high magnesian calcite
4	9.51	43.64	0.00	1.19	0.21	45.44	100.00	0.23	0.75	0.00	0.02	0.00	1.00	Micritic high magnesian calcite
5	9.00	44.19	0.00	1.44	0.00	45.37	100.00	0.22	0.76	0.00	0.02	0.00	1.00	Micritic high magnesian calcite
6	8.62	44.94	0.00	0.89	0.23	45.32	100.00	0.21	0.78	0.00	0.01	0.00	1.00	Micritic high magnesian calcite
7	3.66	51.67	0.00	0.09	0.00	44.59	100.00	0.09	0.91	0.00	0.00	0.00	1.00	Recystallized microsparry magnesian calcite
8	8.59	45.80	0.00	0.00	0.21	45.40	100.00	0.21	0.79	0.00	0.00	0.00	1.00	Micritic high magnesian calcite
9	9.47	44.34	0.00	0.50	0.18	45.51	100.00	0.23	0.76	0.00	0.01	0.00	1.00	Micritic high magnesian calcite
10	9.46	44.61	0.00	0.20	0.19	45.53	100.00	0.23	0.77	0.00	0.00	0.00	1.00	Micritic high magnesian calcite
11	9.06	44.89	0.00	0.29	0.34	45.43	100.00	0.22	0.78	0.00	0.00	0.00	1.00	Micritic high magnesian calcite
12	10.84	42.97	0.00	0.17	0.26	45.76	100.00	0.26	0.74	0.00	0.00	0.00	1.00	Micritic high magnesian calcite
13	7.78	46.72	0.00	0.00	0.25	45.25	100.00	0.19	0.81	0.00	0.00	0.00	1.00	Micritic high magnesian calcite
14	9.13	44.85	0.00	0.33	0.24	45.46	100.00	0.22	0.77	0.00	0.00	0.00	1.00	Micritic high magnesian calcite

Note: **Analytical totals were low (<90%) because the cements were very microporous. Therefore all data were normalised to 100%*

3.5 SAMPLE HG6 STN 31C

This sample contained only 3 small fragments (up to 40 mm) of carbonate-cemented siltstone to very fine sandstone (Figure 38). The fragments are highly irregular in shape, varying from a very rough-surfaced flat plate to an elongate clast resembling a burrow infill. Some abrasion and rounding of the clast surfaces is apparent, and the surfaces of the clasts are slightly stained by orange-brown iron oxyhydroxide. The largest of these clasts was examined petrographically.

Figure 38. Photograph showing the morphology of carbonate-cemented rock fragments in sample HG6 STN 31C. Many fragments are highly irregular and the central clast displays open burrows produced by marine organisms.

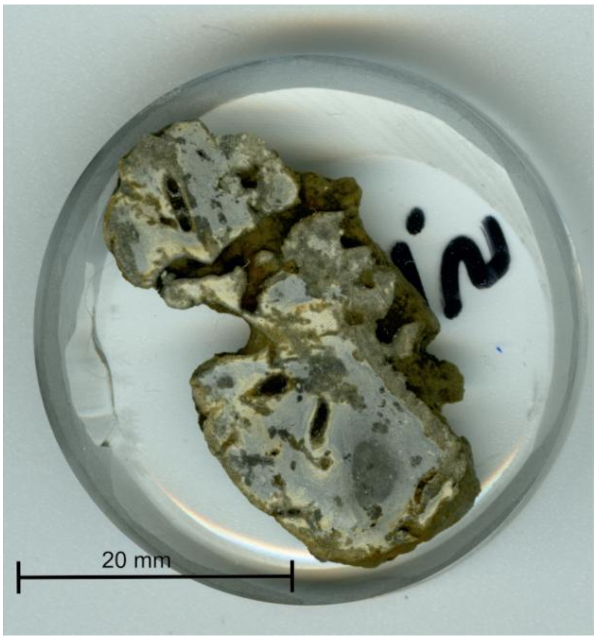

Figure 39. Polished section through a clast of dolomite-cemented siltstone to very fine sandstone. It shows the outer edges of the clast and the walls of borings and burrows are more porous and are stained by iron oxyhydroxide. Sample HG6 STN 31C.

In polished section the clast can be seen to be penetrated by several large branching burrow-like structures, up to10 mm long and up to 2 mm wide (Figure 39). These are only partially filled by porous dolomite-cemented fine sand. Smaller, more delicate borings penetrate the outer margin of the clast to a depth of about 4 mm. These borings can be seen all round the exterior surface of the clast (Figure 39). This demonstrates that this fragment of carbonate-cemented sandstone was an eroded pebble exposed and rolling around on the sea bed, rather than a fragment of in-situ carbonate-cemented sediment.

Petrographic analysis shows that the rock is composed predominantly of very fine sandstone to siltstone, with angular grains of major quartz, minor feldspars and lithic clasts, and traces of iron oxides. It is mostly strongly cemented by micritic dolomite, which preserved an uncompacted grain fabric (Figure 40). As with the other magnesian calcite and aragonite-cemented sediments, this fabric shows that dolomite cementation must have occurred shortly after deposition and before significant burial. The outer part of the clast and the sandy infill of the burrows penetrating into the clast, also preserve uncompacted grain fabrics but have a high intergranular porosity which is only partially-filled by microporous micritic dolomite (Figure 41).

High-resolution BSEM observations show that the micritic dolomite preserves a well-developed microcellular fabric, comprising aggregates of dolomite microcrystals typically less than 1 μm in size that have nucleated around or encrusting a central microcavity about 1-2 μm in diameter. These structures very closely resemble fossilised and mineralised bacterial cells described from experimental studies and other environments in the literature (cf. Martill and Wilby, 1994; Wilby and Whyte, 1995). Further support for this origin is provided by the observations that many of these cellular microstructures appear to be preserved in the process of cell division or mytosis (e.g. Figure 43). Denser areas of cementation have formed as these microcellular structures coalesce and become more compacted. Similar dolomite fabrics were observed by Milodowski et al. (2009) from MDAC samples studied from the Mid Irish Sea. However, the dolomite-mineralised microcellular structures are better preserved in the Braemar Pockmark samples.

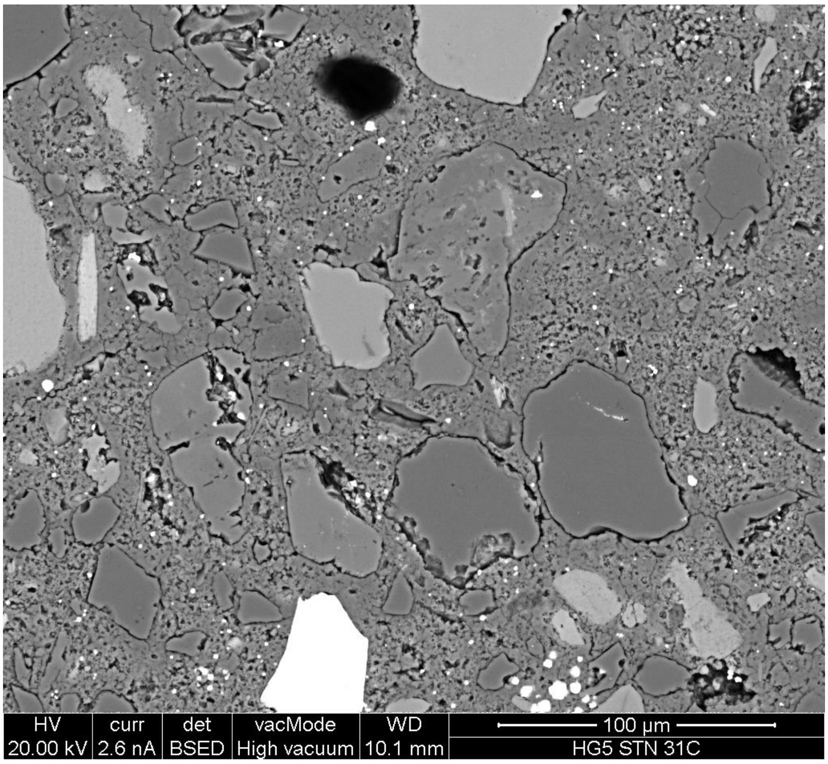

Figure 40. BSEM photomicrograph showing the uncompacted grain fabric of the sandstone and the microporous micritic dolomite cement near the margin of the clast. Sample HG6 STN 31C.

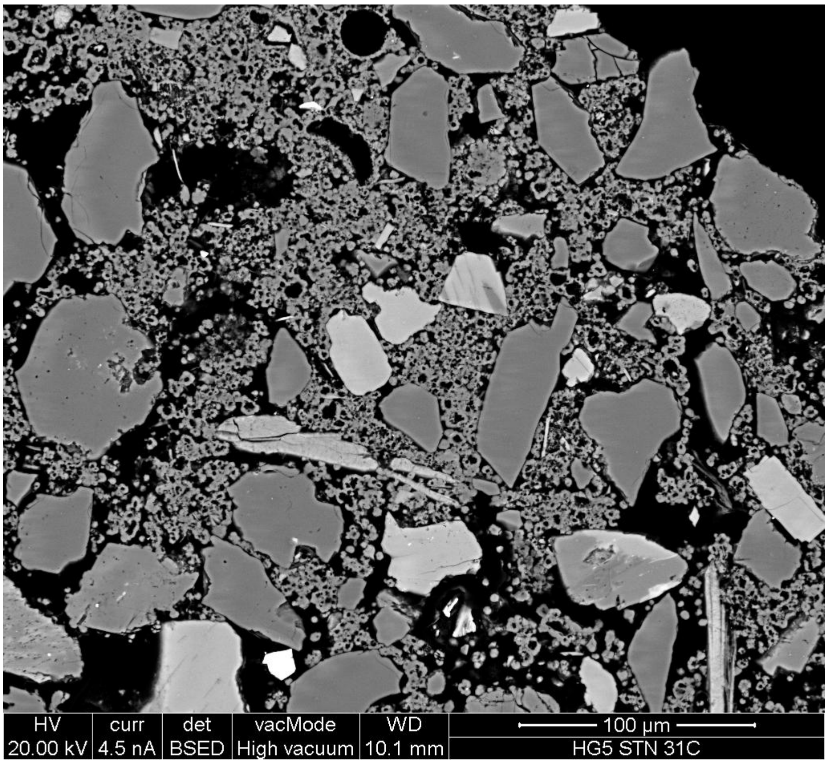

Figure 41. BSEM photomicrograph showing the uncompacted grain fabric of the sandstone and the microporous micritic dolomite cement near the margin of the clast. Sample HG6 STN 31C.

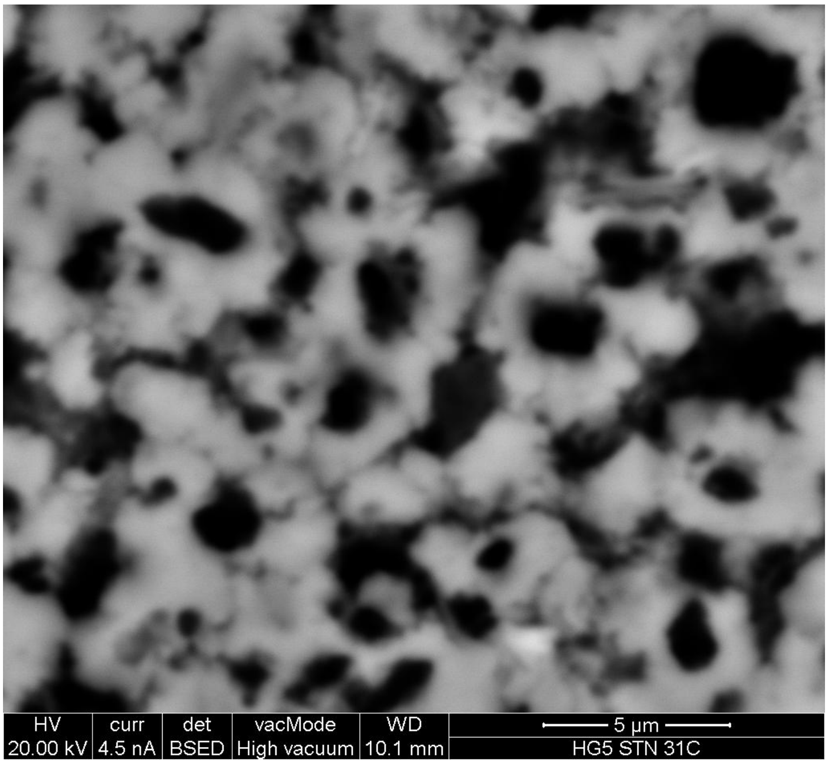

Figure 42. BSEM photomicrograph showing the detail of the micritic dolomite cement. The dolomite preserves a well-developed cellular microfabric that represents mineralised bacterial cells. Sample HG6 STN 31C.

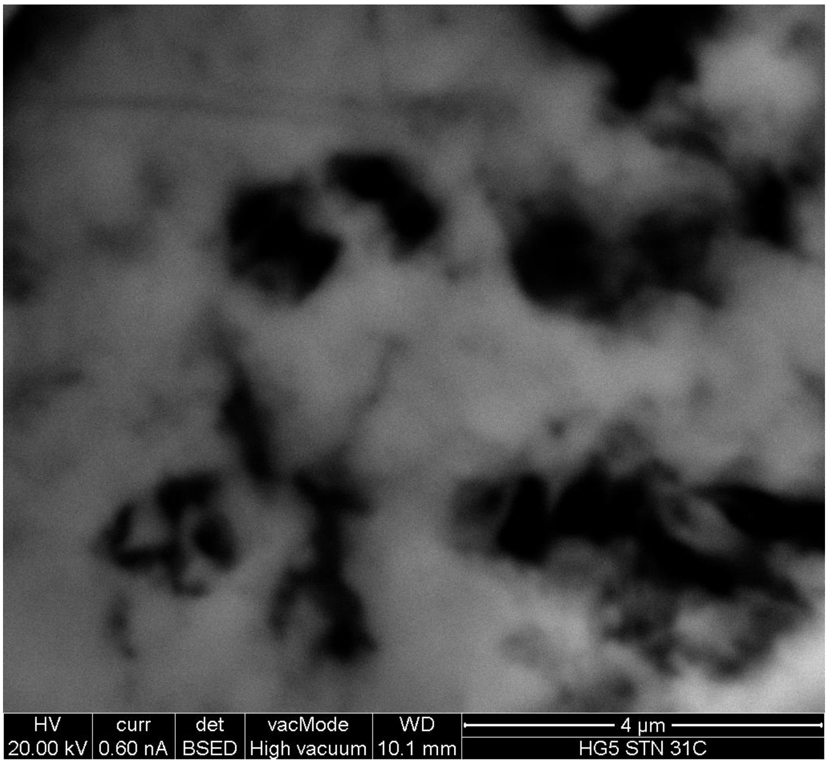

Figure 43. BSEM photomicrograph showing the detail of the micritic dolomite cement. The dolomite appears to preserve a microbial cellular microfabric. One cell-like feature appears to be in the process of dividing (mytosis) before being mineralised by dolomite. Sample HG6 STN 31C.

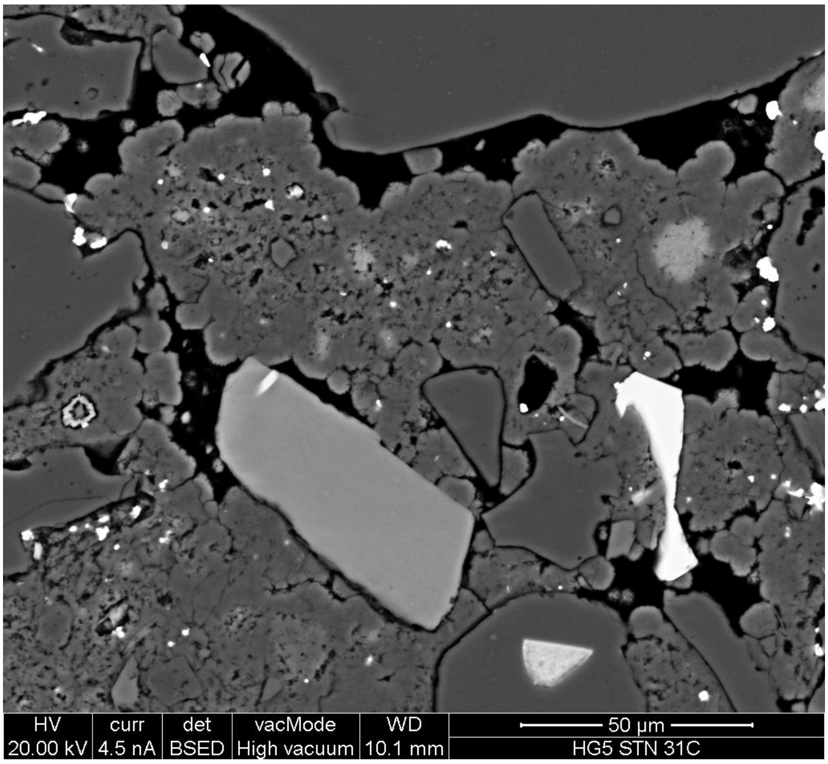

Figure 44. BSEM photomicrograph showing the development of micro-colloform dolomite cement nucleated on pelletized grains composed of compact dolomicrite, and filling the intergranular pores in the dolomite-cemented sandstone. Minor late calcite (light grey) replaces the dolomite in small patches. Sample HG6 STN 31C.

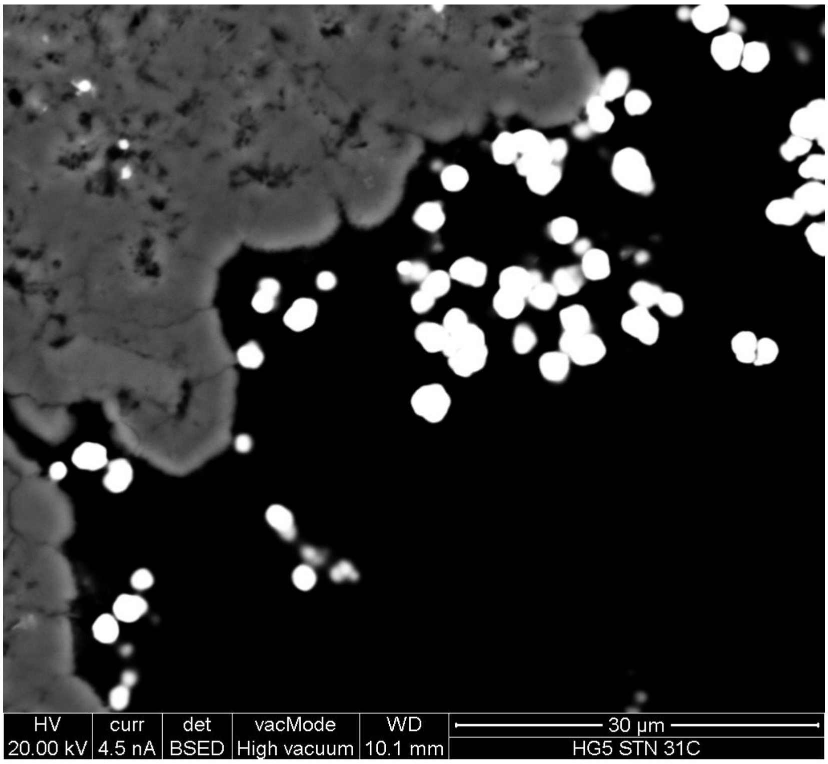

Figure 45. BSEM photomicrograph showing fine microcrystals of pyrite (bright) rests on micro-colloform dolomite which lines the walls of a burrow cavity the dolomite-cemented sandstone. Sample HG6 STN 31C.

Some of the denser areas of micritic dolomite cement also appear to be pelloidal in origin (Figure 44). A similar pelletized micrite fabric was also observed in some of magnesian calcite cemented samples. It comprises well-rounded compact grains of dolomicrite encrusted by subsequent microcolloform overgrowths of finely-crystalline dolomite (Figure 44). This fabric is particularly evident in the microporous sandy burrow fills. The pellet cores of the dolomicrite also exhibit minor replacement by microcrystalline (microsparry) low-magnesian calcite.

Authigenic pyrite is abundant in this rock. It occurs as microcrystals lining the walls of burrow cavities and open pores, where it rests on top of earlier-formed microcolloform dolomite cement (Figure 45). The dolomicrite pellets also contain abundant finely-disseminated pyrite. Pyrite also fills residual interstitial micropores in the dolomicrite (similar to the pyrite observed in samples HG3 STN 42B and HG3 STN 42C. The pyrite has been partially oxidised to secondary iron oxides around the porous margins of the clast and along burrows and borings.

EPMA analyses of the carbonate cements are presented in Table 6 and are summarised in Figure 46. The dolomite cements are all very similar in composition and are characterised by calcium-rich dolomite (composition of $Ca_{0.51-0.54}Mg_{0.46-0.49}CO_3$), with 1-4 mole % Ca in excess of the ideal stoichiometry for dolomite $Ca_{0.5}Mg_{0.5}CO_3$. This is very similar to the excess Ca dolomites (average composition $Ca_{0.53}Mg_{0.47}CO_3$) described by Jensen et al. (1992) from MDAC deposits in the Kattegat off the coast of Denmark, and dolomite described by Milodowski et al. (2009) in MDAC from the Mid Irish Sea. The presence of a significant excess in Ca in dolomite at low temperature may indicate that the dolomite is relatively poorly ordered and/or metastable, and may have precipitated rapidly (Vahrenkamp and Swart, 1994) possibly forming via a “protodolomite” precursor (cf. Deer et al., 1992). This would also be consistent with petrographic observations that provide strong evidence that the dolomite was produced by bacterial biomineralisation.

The minor calcite seen replacing the dolomicrite cement is magnesian, with up 2-4 1-4 mole % $MgCO_3$ in solid-solution. It is much less magnesian that the primary micritic magnesian calcite cements seen in the other samples from the Braemar Pockmark. However, its composition is close to that of the secondary microsparry calcite seen to replace the micritic calcite in these rocks.

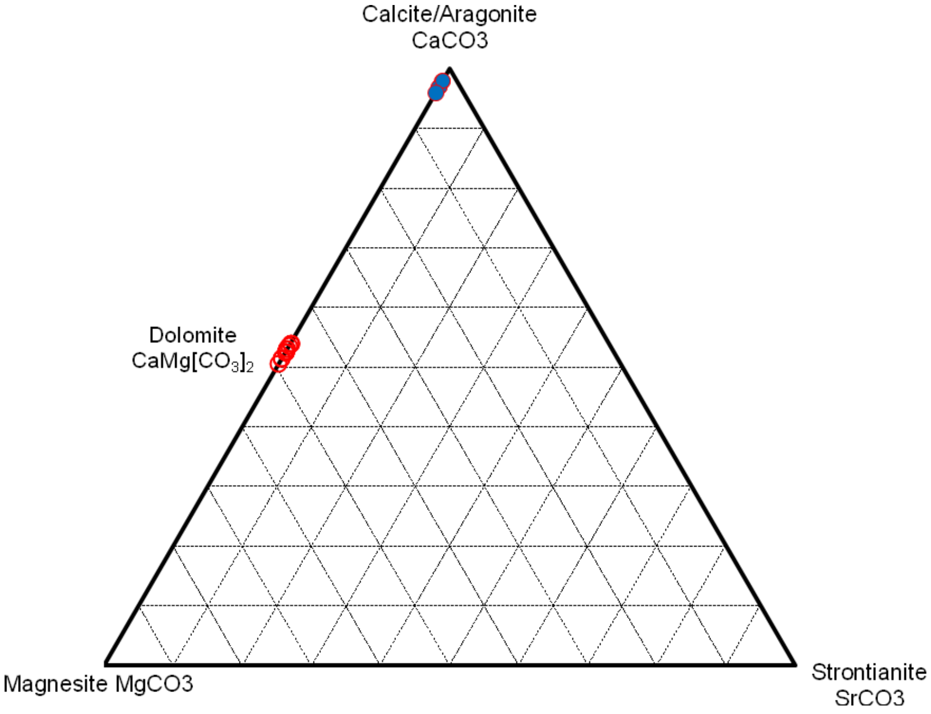

Figure 46. $CaCO_3$-$MgCO_3$-$SrCO_3$ molar ratio plot illustrating the compositions of the microsparry calcite cement (solid blue circles) replacing micritic microcolloform dolomite (open red circles). MDAC sample HG6 STN 31C, relative to end-member carbonate minerals.

The sequence of sedimentary and post-depositional diagenetic events recorded from sample HG6 STN 31C is very similar to that observed in the other samples from the Braemar Pockmark, and can be summarised as follows:

1. Deposition of fine sand and silt sediment;
2. Microbial precipitation of micritic dolomite within the near-surface of the sediment, and precipitation of authigenic pyrite associated with iron and sulphate reduction in sediment.
3. Syndepositional bioturbation and reworking of the dolomicritic sediment associated with the production of pelloidal grains of dolomicrite (possibly faecal pellets);
4. Ongoing microbial precipitation of micritic dolomicrite and lithification, accompanied by further precipitation of authigenic pyrite;
5. Minor recrystallisation, replacement and overgrowth of micritic dolomicrite by low magnesian calcite;
6. Erosion and abrasion of eroded clasts;
7. Boring of the clast surfaces by marine biota, and oxidation of pyrite near the clast surface.

Table 6. Electron microprobe analyses of carbonate cements in sample HG3 STN 42C.

No.	WEIGHT % OXIDE (normalised)							IONIC RATIO [normalised to 3 [O]						COMMENTS
	MgO	CaO	MnO	FeO	SrO	CO_2 (calc)	*Total wt%	Mg^{2+}	Ca^{2+}	Mn^{2+}	Fe^{2+}	Sr^{2+}	CO_3^{2-}	
1	1.12	54.29	0.00	0.48	0.00	44.11	100.00	0.03	0.97	0.00	0.01	0.00	1.00	microsparry calcite replacing dolomite
2	0.99	54.78	0.00	0.11	0.00	44.12	100.00	0.02	0.97	0.00	0.00	0.00	1.00	microsparry calcite replacing dolomite
3	1.01	54.69	0.00	0.18	0.00	44.12	100.00	0.03	0.97	0.00	0.00	0.00	1.00	microsparry calcite replacing dolomite
4	0.78	54.75	0.00	0.30	0.14	44.04	100.00	0.02	0.98	0.00	0.00	0.00	1.00	microsparry calcite replacing dolomite
5	1.58	54.02	0.00	0.19	0.00	44.22	100.00	0.04	0.96	0.00	0.00	0.00	1.00	microsparry calcite replacing dolomite
6	19.72	32.66	0.00	0.00	0.33	47.29	100.00	0.46	0.54	0.00	0.00	0.00	1.00	microcolloform dolomite
7	20.10	32.16	0.00	0.00	0.39	47.34	100.00	0.46	0.53	0.00	0.00	0.00	1.00	microcolloform dolomite
8	20.00	32.29	0.00	0.00	0.37	47.33	100.00	0.46	0.54	0.00	0.00	0.00	1.00	microcolloform dolomite
9	20.51	31.65	0.00	0.17	0.24	47.43	100.00	0.47	0.52	0.00	0.00	0.00	1.00	microcolloform dolomite
10	20.01	32.28	0.00	0.00	0.39	47.33	100.00	0.46	0.54	0.00	0.00	0.00	1.00	microcolloform dolomite
11	20.27	31.81	0.00	0.22	0.34	47.36	100.00	0.47	0.53	0.00	0.00	0.00	1.00	microcolloform dolomite
12	20.42	31.44	0.00	0.34	0.45	47.35	100.00	0.47	0.52	0.00	0.00	0.00	1.00	microcolloform dolomite
13	20.33	31.63	0.00	0.50	0.17	47.38	100.00	0.47	0.52	0.00	0.01	0.00	1.00	microcolloform dolomite
14	20.37	31.19	0.00	0.77	0.34	47.33	100.00	0.47	0.52	0.00	0.01	0.00	1.00	microcolloform dolomite
15	21.28	30.33	0.00	0.64	0.23	47.52	100.00	0.49	0.50	0.00	0.01	0.00	1.00	microcolloform dolomite
16	20.19	31.41	0.00	0.84	0.26	47.30	100.00	0.47	0.52	0.00	0.01	0.00	1.00	microcolloform dolomite
17	21.03	30.73	0.00	0.52	0.25	47.48	100.00	0.48	0.51	0.00	0.01	0.00	1.00	microcolloform dolomite
18	20.14	31.42	0.00	0.80	0.37	47.28	100.00	0.46	0.52	0.00	0.01	0.00	1.00	microcolloform dolomite
19	20.77	31.03	0.00	0.46	0.31	47.43	100.00	0.48	0.51	0.00	0.01	0.00	1.00	microcolloform dolomite
20	20.62	31.15	0.00	0.56	0.26	47.40	100.00	0.47	0.52	0.00	0.01	0.00	1.00	microcolloform dolomite

Note: **Analytical totals were low (<90%) because the cements were very microporous. Therefore all data were normalised to 100%*

3.6 SAMPLE HG8 STN 31B

Sample HG8 STN 31B is represented by a large slab of carbonate-cemented siltstone up to 130 mm across and about 10-15 mm thick (Figure 47). The edges of the slab appear to be rounded and abraded, which suggests that slab is a large eroded fragment or clast. The surfaces of the slab penetrated by numerous fine borings, and are also encrusted by calcareous tubes of serpulid worms.

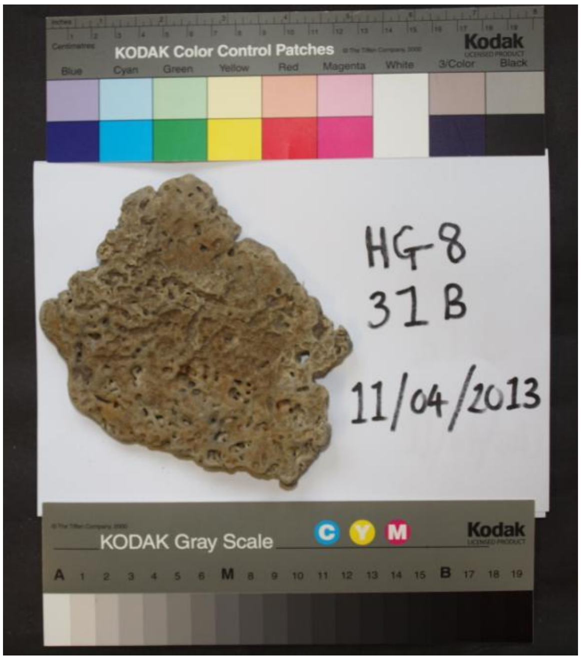

Figure 47. Photograph showing the slab-like morphology of carbonate-cemented rock fragment in sample HG8 STN 31B. The fragment is irregular and its surface has been bored marine organisms and encrusted by serpulid worm tubes.

Mineralogically and petrographically this sample is very similar to the magnesian calcite cemented sediments described earlier from samples HG2 STN 46B and HG2 STN 46C (see Sections 3.1and 3.2). However, this sample is finer grained and comprises largely magnesian calcite-cemented siltstone (Figure 48). As with the other samples, the detrital grain fabric the rock is uncompacted, indicating that cementation occurred very early in diagenesis and before any significant burial.

The rock is cemented largely by micritic high-magnesian calcite. This comprises a rigid matrix of finely fibrous crystallites of magnesian calcite that have growth between the clay and silt particles, pushing the detrital particles apart (Figure 49). The matrix is very microporous. In places the micrite has been altered and recrystallised to be replaced by finely crystalline patches of low-magnesian calcite (Figure 49). This later low-magnesian calcite also lines burrow and boring cavities in the rock (Figure 50)

Authigenic pyrite is common. It occurs as finely disseminated pyrite within the micrite matrix and intimately intergrown with the micritic carbonate. Pyrite also occurs as larger framboidal aggregates lining or partially filling burrow and boring cavities, where it rests on low-magnesian calcite coated surfaces (Figure 50).

Some of the pyrite is oxidised to very fine and disseminated secondary iron oxide or oxyhydroxide close to the outer surfaces of the slab. Pyrite oxidation and staining by secondary iron oxides or oxyhydroxides is evident within the burrow-like features.

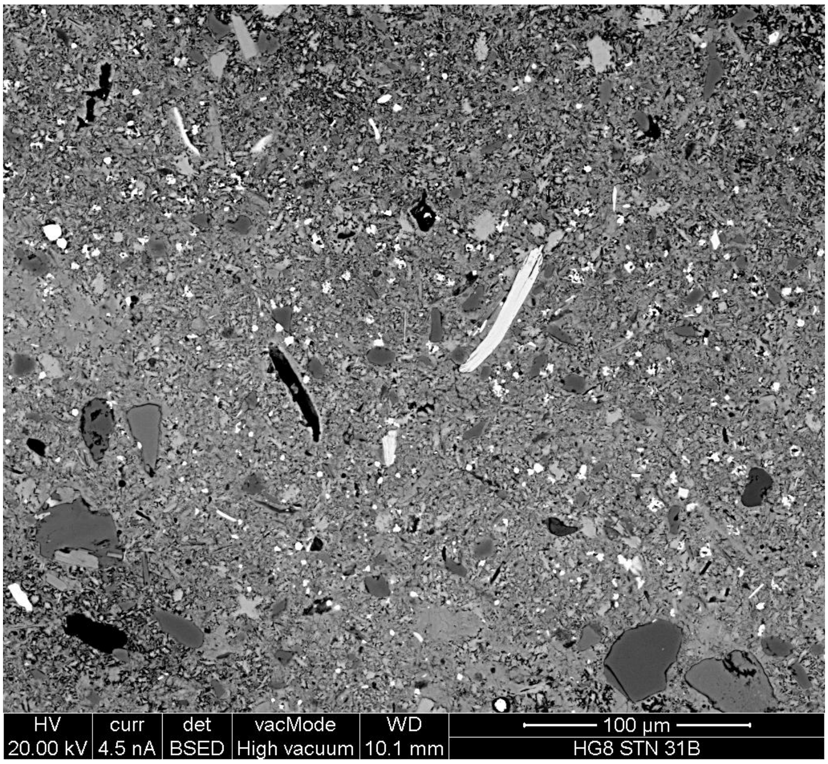

Figure 48. BSEM photomicrograph showing fine siltstone tightly cemented by very fine micritic magnesian calcite. Sample HG8 STN 31B.

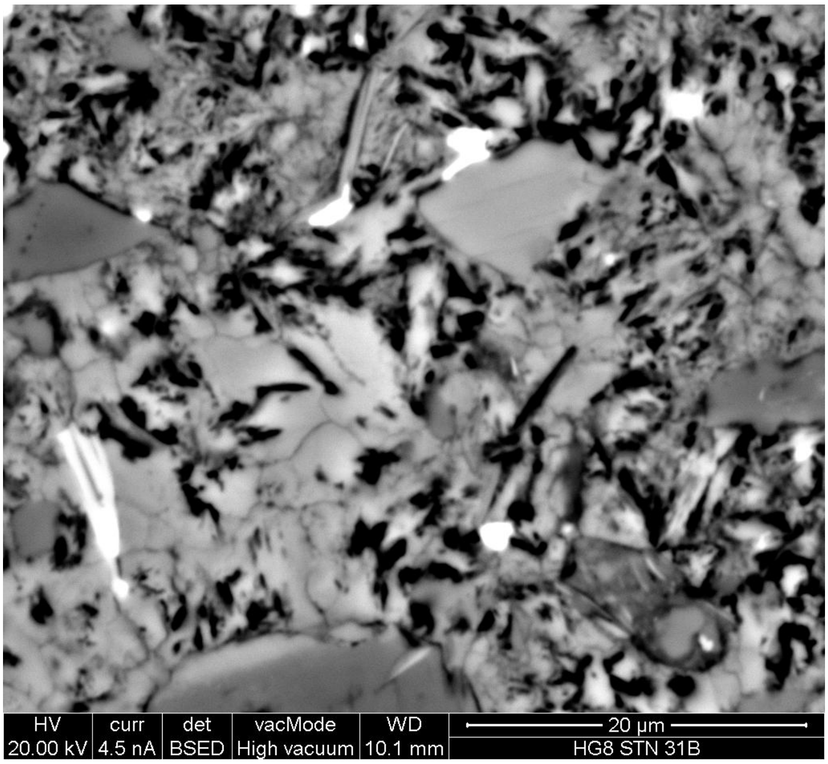

Figure 49. BSEM photomicrograph showing fine grained microporous and microfibrous fabric the micritic magnesian calcite cement. Sample HG8 STN 31B

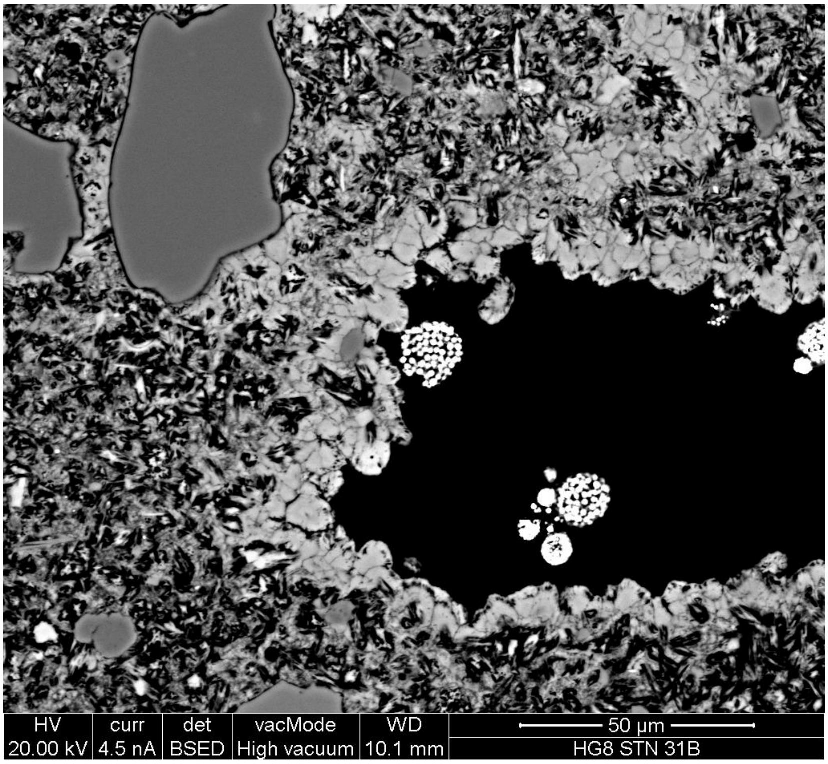

Figure 50. BSEM photomicrograph showing the fine grained microporous fabric the micritic magnesian calcite cement (dark areas). The micritic magnesian calcite has been locally overprinted around the walls of cavities in the rock by an equant crystal mosaics of microcrystalline low-magnesian calcite. Framboids of pyrite line the cavity and abundant fine pyrite is also disseminated within the micrite matrix. Sample HG8 STN 31B

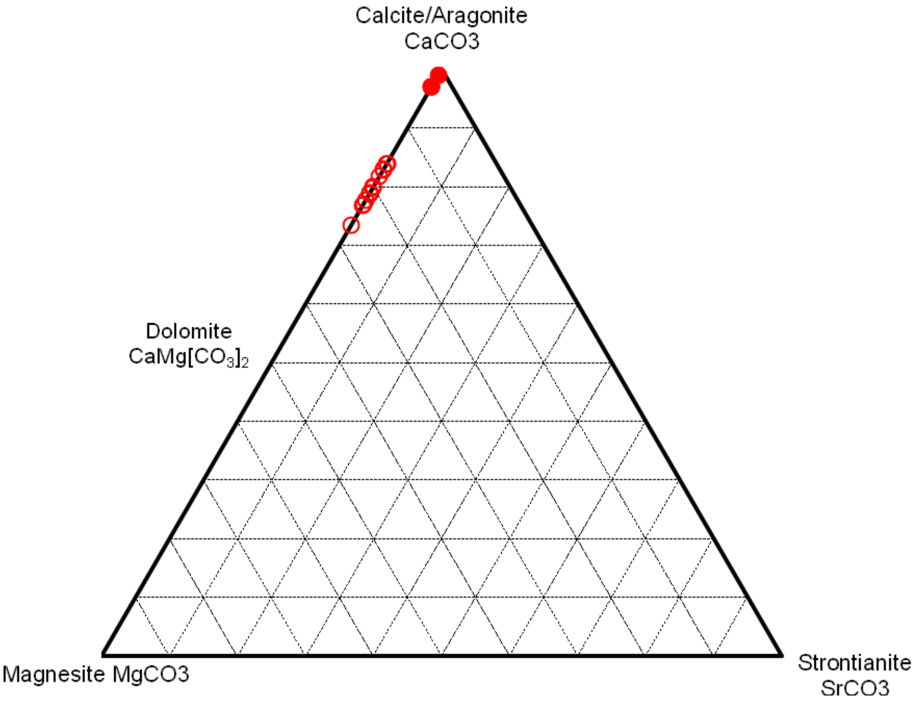

Figure 51. $CaCO_3$-$MgCO_3$-$SrCO_3$ molar ratio plot illustrating the compositions of the microsparry calcite cement (solid red circles) replacing micritic high-magnesium calcite (open red circles). MDAC sample HG8 STN 31B, relative to end-member carbonate minerals.

The EPMA data for the micritic magnesian calcite show it to contain between 16 to 26 mole % $MgCO_3$ in solid-solution (Table 7 and Figure 51) within the calcite lattice (i.e. the structural formula of the calcite can be represented as $Ca_{0.74-0.84}Mg_{0.26-0.16}CO_3$). Most analyses of the micritic calcite cluster towards the higher end of this range and are similar to the micritic high magnesium cement found in the other samples. These cements are at high-magnesian calcite end of the calcite ($CaCO_3$)-magnesite ($MgCO_3$) solid-solution series (cf. Deer et al., 1962a,b; Mackenzie et al., 1983). However, SEM-EDXA observations indicate that the recrystallisation of the micrite to coarser microsparry calcite cement produced calcite with a much lower magnesium content (Figure 51) with only between 1-3 mole % $MgCO_3$ in sold solution (i.e. $Ca_{0.97-0.99}Mg_{0.03-0.01}CO_3$).

The sequence of sedimentary and diagenetic events is summarised below

1. Deposition of very fine sand and silt sediment;
2. Bioturbation;
3. Precipitation of micritic high-magnesian calcite within the near-surface of the sediment, simultaneously associated with iron and sulphate reduction in the anoxic sediment and the precipitation of fine authigenic pyrite;
4. Partial recrystallisation of micritic high-magnesian calcite to fine grained lower magnesian calcite, associated with further lithification of the sediment;
5. Precipitation of framboidal pyrite in burrows and borings;
6. Erosion and burrowing of the lithified rock, and current rolling and abrasion of eroded clasts; Erosion of the magnesian calcite-cemented sediment, with local transport and abrasion of the eroded clasts of carbonate-cemented sandstone and siltstone, and oxidation of pyrite to form finely disseminated iron oxyhydroxide now staining the clasts.

Table 7. Electron microprobe analyses of carbonate cements in sample HG8 STN 31B.

No.	WEIGHT % OXIDE (normalised)							IONIC RATIO [normalised to 3 [O]						COMMENTS
	MgO	CaO	MnO	FeO	SrO	CO_2 (calc)	*Total wt%	Mg^{2+}	Ca^{2+}	Mn^{2+}	Fe^{2+}	Sr^{2+}	CO_3^{2-}	
1	6.45	48.33	0.00	0.16	0.00	45.06	100.00	0.16	0.84	0.00	0.00	0.00	1.00	micritic high magnesian calcite
2	6.60	47.86	0.00	0.24	0.29	45.02	100.00	0.16	0.83	0.00	0.00	0.00	1.00	micritic high magnesian calcite
3	7.15	47.48	0.00	0.00	0.23	45.15	100.00	0.17	0.83	0.00	0.00	0.00	1.00	micritic high magnesian calcite
4	7.14	47.32	0.00	0.23	0.18	45.13	100.00	0.17	0.82	0.00	0.00	0.00	1.00	micritic high magnesian calcite
5	8.53	45.91	0.00	0.00	0.17	45.40	100.00	0.21	0.79	0.00	0.00	0.00	1.00	micritic high magnesian calcite
6	8.93	45.36	0.00	0.00	0.26	45.45	100.00	0.21	0.78	0.00	0.00	0.00	1.00	micritic high magnesian calcite
7	8.36	46.12	0.00	0.00	0.15	45.37	100.00	0.20	0.80	0.00	0.00	0.00	1.00	micritic high magnesian calcite
8	8.44	45.97	0.00	0.00	0.22	45.37	100.00	0.20	0.79	0.00	0.00	0.00	1.00	micritic high magnesian calcite
9	8.16	46.31	0.00	0.00	0.20	45.33	100.00	0.20	0.80	0.00	0.00	0.00	1.00	micritic high magnesian calcite
10	8.68	45.60	0.00	0.16	0.15	45.41	100.00	0.21	0.79	0.00	0.00	0.00	1.00	micritic high magnesian calcite
11	9.18	44.86	0.00	0.19	0.30	45.46	100.00	0.22	0.77	0.00	0.00	0.00	1.00	micritic high magnesian calcite
12	10.97	42.23	0.00	0.82	0.25	45.72	100.00	0.26	0.72	0.00	0.01	0.00	1.00	micritic high magnesian calcite
13	1.24	54.47	0.00	0.13	0.00	44.16	100.00	0.03	0.97	0.00	0.00	0.00	1.00	micritic high magnesian calcite
14	1.15	54.60	0.00	0.10	0.00	44.15	100.00	0.03	0.97	0.00	0.00	0.00	1.00	micritic high magnesian calcite
15	9.46	44.46	0.00	0.33	0.24	45.51	100.00	0.23	0.77	0.00	0.00	0.00	1.00	micritic high magnesian calcite
16	7.57	46.74	0.00	0.25	0.25	45.19	100.00	0.18	0.81	0.00	0.00	0.00	1.00	micritic high magnesian calcite
17	9.79	44.26	0.00	0.34	0.00	45.61	100.00	0.23	0.76	0.00	0.00	0.00	1.00	micritic high magnesian calcite
18	1.24	54.47	0.00	0.13	0.00	44.16	100.00	0.03	0.97	0.00	0.00	0.00	1.00	late calcite replacing magnesian calcite
19	1.15	54.60	0.00	0.10	0.00	44.15	100.00	0.03	0.97	0.00	0.00	0.00	1.00	late calcite replacing magnesian calcite
20	0.60	55.12	0.00	0.24	0.00	44.04	100.00	0.01	0.98	0.00	0.00	0.00	1.00	late calcite replacing magnesian calcite
21	0.46	55.30	0.00	0.22	0.00	44.02	100.00	0.01	0.99	0.00	0.00	0.00	1.00	late calcite replacing magnesian calcite

Note: **Analytical totals were low (<90%) because the cements were very microporous. Therefore all data were normalised to 100%*

3.7 SAMPLE HG8 STN 37B

This sample consists of moderately-flat pebble-sized clast up to 80 mm across (Figure 52). It is composed of fine grained sandstone to siltstone, cemented largely by high-magnesian magnesian calcite. The clast is extensively bored all around its external surfaces (Figure 53), consistent with the clast being a pebble exposed on the sea bed to boring marine organisms. The boring must post-date lithification of the sediment.

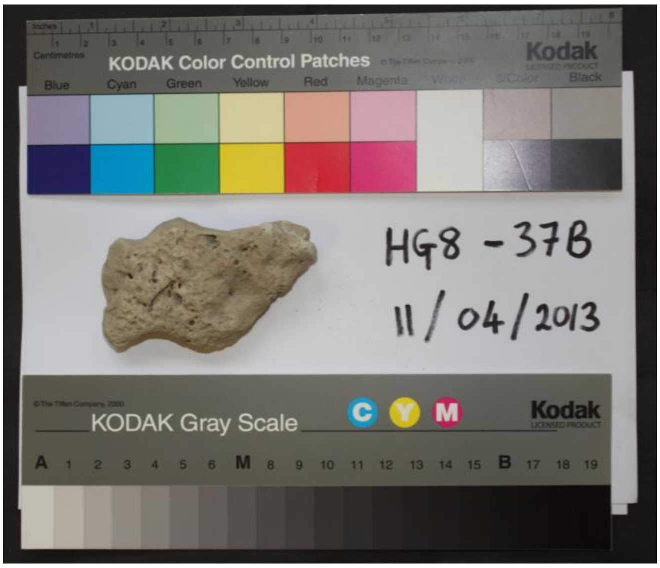

Figure 52. Photograph showing the well-rounded and slightly irregular morphology of the pebble of carbonate-cemented rock fragment in sample HG8 STN 37B. The surface of the clast is pitted and has been bored marine organisms.

Figure 53. Polished section through the pebble of magnesian calcite-cemented siltstone to very fine sandstone. It shows the outer edges of the clast have been extensively bored and burrowed. The bulk of the clast has been stained by orange-brown iron oxyhydroxide, which has been bleached around the burrows or borings HG8 STN 37B.

In the polished section, the matrix of the pebble can be seen to be heavily-stained by finely-disseminated iron oxyhydroxide (Figure 53), indicating it has been exposed to an oxidizing environment. However, later bleaching of the iron oxyhydroxide pigmentation is evident adjacent to borings, which implies that localised reduction around these features has subsequently occurred. This is probably related to the decomposition of organic matter present within these borings.

The petrology of this sample is very similar to that of HG8 STN 31B and of the other carbonate-cemented samples dominated by high magnesian calcite cement. Detrital grains are dominated by silt- to very fine sand-grade angular quartz, with minor to trace amounts of K-feldspar, plagioclase lithic clasts, and flakes of muscovite, with traces of altered iron-titanium oxides (Figure 54). The rock is characterised by an uncompacted detrital grain fabric, in which the detrital silicate grains show minimal grain contacts, and ‘float’ in an intergranular matrix of micritic carbonate (Figure 54). This uncompacted grain fabric indicates that cementation by the micritic carbonate occurred early in diagenesis, and prior to any significant burial.

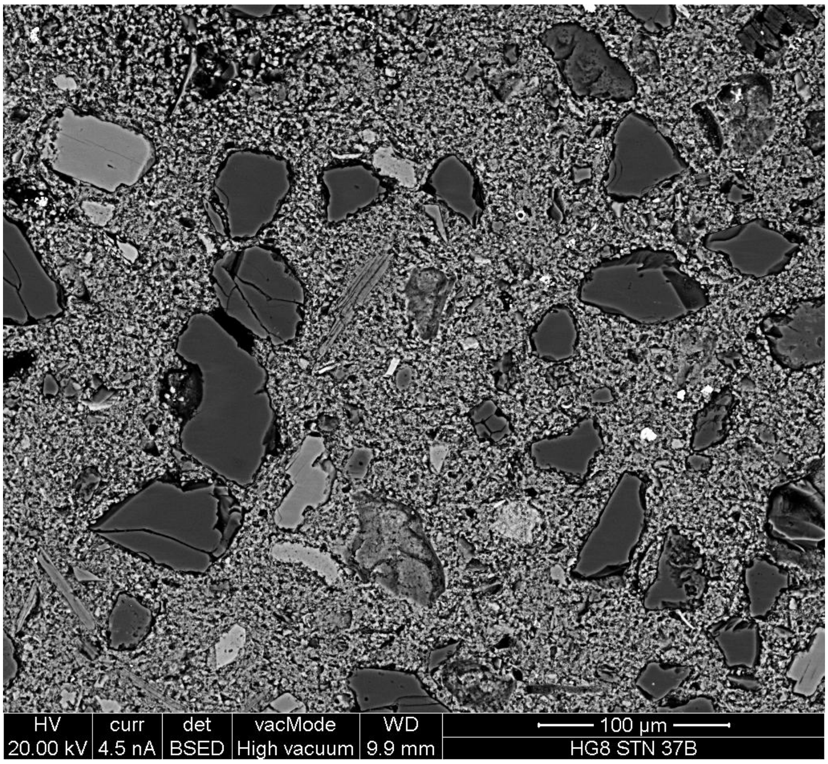

Figure 54. BSEM photomicrograph of the uncompacted detrital grain fabric of the siltstone, containing angular grains of quartz (dark-grey), K-feldspar (light-grey) and flakes of mica, ‘floating’ in a matrix of micritic high-magnesian calcite. The micrite can be seen to fill relatively large areas compared to the detrital grain size. Sample HG8 STN 37B.

The micritic matrix comprises very fine grained high-magnesium calcite cement (Figure 55). This is highly microporous and preserves some relicts of an original microcellular fabric that is similar to the microfabric seen in the other samples described previously, and is probably of microbial origin. A significant proportion of this matrix material occupies discrete large intergranular volumes that are oversized relative to the detrital grain size and state of compaction of the rock (Figure 54). This suggests that these volumes of micrite were originally deposited as discrete, well-rounded, sand-grade ‘pelloidal grains composed of micritic carbonate, rather than as fine-grained micritic sediment. These micritic pelloidal grains may represent faecal pellets. This would imply that the precipitated micritic carbonate sediment was reworked by marine benthic organisms prior to lithification.

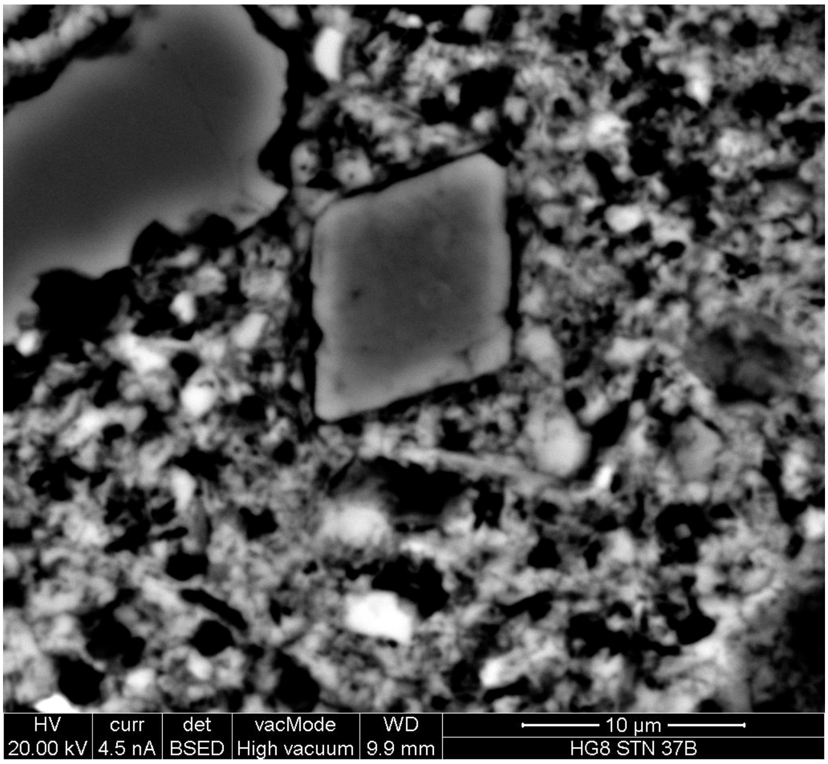

Figure 55. BSEM photomicrograph of the very fine grained matrix of micritic high-magnesian calcite. The micrite preserves a relict microcellular fabric possibly of biogenic origin. A relatively coarse idiomorphic rhomb of later dolomite can be seen to have nucleated within the micrite. Sample HG8 STN 37B.

The micrite displays localised minor recrystallisation, coarsening and replacement by coarser microsparry calcite. This is closely associated with minor growth of idiomorphic rhombs of dolomite, very similar to that seen in sample HG3 STN 42B. Again, this close association of recrystallisation of high-magnesian calcite, and its partial replacement by low magnesian calcite may have released magnesium into the sediment porewaters, thereby promoting minor dolomitisation of the micrite cement.

Authigenic pyrite is common in this sample, and is closely associated with the micritic magnesian calcite. Pyrite occurs as minor microcrystalline fills within the interstitial microporosity in the micrite. It also occurs as framboidal pyrite, which is characteristic of low-temperature and early diagenetic sulphide formation within the sulphide reduction zone of marine sediments (Berner, 1969; 1980; Rickard, 1970; 1975; Sweeney & Kaplan, 1973). Some of this pyrite has been oxidised to iron oxide or oxyhydroxide which accounts for the secondary iron oxide accounts for the orange and red-brown staining seen on these carbonate-cemented rock fragments. Disseminated fine pyrite is also abundant in the matrix of the wallrock immediately adjacent to the borings and would account for the bleaching of the iron oxyhydroxide staining from around these features.

Electron microprobe analyses of the calcite and dolomite cement are presented in Table 8. These data are summarised in Figure 56 in terms of molar proportions of end-member $CaCO_3$-$MgCO_3$-$FeCO_3$. The limited number of analyses obtained from the early micritic magnesian calcite cement show that it is high-magnesian calcite with between 22 to 31 mole % $MgCO_3$ in solid-solution (Figure 56). This suggests that the micrite in this sample may be slightly more magnesium-rich than the micritic magnesian calcite analysed from the other samples from the Braemar Pockmark. The very limited number of analyses for the later calcite indicate that the minor recrystallisation of the magnesian calcite micrite to coarser microsparry calcite produced a relatively-low magnesium calcite (Figure 56) with between 7-9 mole % $MgCO_3$ in sold solution (i.e. $Ca_{0.95-0.99}Mg_{0.05-0.01}CO_3$). This process will potentially have liberated magnesium into the porewaters of the sediment, and this may have promoted the formation of the small amount of dolomite closely associated with these calcite cements.

The EPMA data show that the dolomite associated with the micritic calcite is calcium-rich with between 4-8 mole % Ca in excess of the ideal stoichiometry for dolomite $Ca_{0.5}Mg_{0.5}CO_3$. This is very similar to the excess Ca dolomites (average composition $Ca_{0.53}Mg_{0.47}CO_3$) described from the other samples of carbonate-cemented sediment examined in this study.

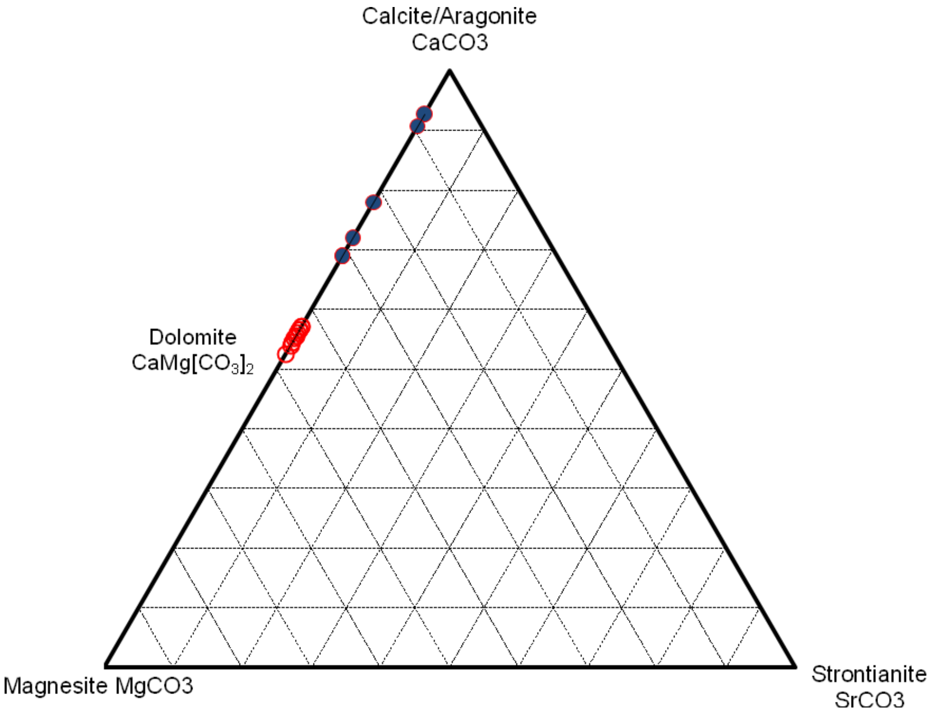

Figure 56. $CaCO_3$-$MgCO_3$-$SrCO_3$ molar ratio plot illustrating the compositions of the micritic high magnesian calcite cement (solid blue circles) and later replacive dolomite microspar cement (open red circles). MDAC sample HG8 STN 37B, relative to end-member carbonate minerals.

The sequence of sedimentary and post-depositional diagenetic events recorded from sample HG8 STN 37B can be summarised as follows:

1. Deposition of fine sand and silt sediment;
2. Microbial precipitation of micritic high-magnesian calcite within the near-surface of the sediment, accompanied by the precipitation of authigenic pyrite.
3. Syndepositional bioturbation and reworking of the sediment, and redeposition of micrite as sand-grade faecal pellets prior to lithification;
4. Partial recrystallisation and replacement of micritic high-magnesian calcite by lower magnesian calcite. The magnesium released to the porewaters during this process may have given rise to very minor dolomitisation of the early micritic calcite;
5. Erosion of the lithified sediment, with abrasion of eroded clasts. and oxidation of pyrite;
6. Boring of the clast surfaces by marine biota;
7. Decay of organic matter remaining in the borings, accompanied by the reduction of iron oxide to pyrite in the walls of borings.

Table 8. Electron microprobe analyses of carbonate cements in sample HG8 STN 37B.

No.	WEIGHT % OXIDE (normalised)							IONIC RATIO [normalised to 3 [O]						COMMENTS
	MgO	CaO	MnO	FeO	SrO	CO_2 (calc)	*Total wt%	Mg^{2+}	Ca^{2+}	Mn^{2+}	Fe^{2+}	Sr^{2+}	CO_3^{2-}	
1	19.78	32.59	0.11	0.09	0.09	47.33	100.00	0.46	0.54	0.00	0.00	0.00	1.00	Dolomite rhomb replacing magnesian calcite
2	20.64	31.60	0.09	0.18	0.01	47.49	100.00	0.47	0.52	0.00	0.00	0.00	1.00	Dolomite rhomb replacing magnesian calcite
3	19.61	32.65	0.02	0.36	0.09	47.28	100.00	0.45	0.54	0.00	0.00	0.00	1.00	Dolomite rhomb replacing magnesian calcite
4	18.71	33.46	0.11	0.39	0.26	47.08	100.00	0.43	0.56	0.00	0.01	0.00	1.00	Dolomite rhomb replacing magnesian calcite
5	18.94	32.87	0.00	1.08	0.00	47.12	100.00	0.44	0.55	0.00	0.01	0.00	1.00	Dolomite rhomb replacing magnesian calcite
6	18.94	33.25	0.00	0.65	0.00	47.16	100.00	0.44	0.55	0.00	0.01	0.00	1.00	Dolomite rhomb replacing magnesian calcite
7	18.50	33.71	0.00	0.70	0.00	47.08	100.00	0.43	0.56	0.00	0.01	0.00	1.00	Dolomite rhomb replacing magnesian calcite
8	18.52	33.47	0.00	0.95	0.00	47.06	100.00	0.43	0.56	0.00	0.01	0.00	1.00	Dolomite rhomb replacing magnesian calcite
9	18.06	33.49	0.00	1.52	0.00	46.92	100.00	0.42	0.56	0.00	0.02	0.00	1.00	Dolomite rhomb replacing magnesian calcite
10	17.99	33.36	0.00	1.75	0.00	46.89	100.00	0.42	0.56	0.00	0.02	0.00	1.00	Dolomite rhomb replacing magnesian calcite
11	18.51	33.20	0.00	1.25	0.00	47.03	100.00	0.43	0.55	0.00	0.02	0.00	1.00	Dolomite rhomb replacing magnesian calcite
12	19.10	32.61	0.00	1.15	0.00	47.14	100.00	0.44	0.54	0.00	0.01	0.00	1.00	Dolomite rhomb replacing magnesian calcite
13	12.91	40.91	0.00	0.00	0.00	46.18	100.00	0.31	0.69	0.00	0.00	0.00	1.00	Micritic high magnesian calcite
14	11.61	42.43	0.00	0.00	0.00	45.96	100.00	0.28	0.72	0.00	0.00	0.00	1.00	Micritic high magnesian calcite
15	12.91	40.90	0.00	0.00	0.00	46.19	100.00	0.31	0.69	0.00	0.00	0.00	1.00	Micritic high magnesian calcite
16	9.32	45.12	0.00	0.00	0.00	45.57	100.00	0.22	0.78	0.00	0.00	0.00	1.00	Micritic high magnesian calcite
17	2.91	50.67	0.43	1.71	0.03	44.25	100.00	0.07	0.90	0.01	0.02	0.00	1.00	Later microsparry calcite
18	3.58	49.90	0.40	1.51	0.27	44.34	100.00	0.09	0.88	0.01	0.02	0.00	1.00	Later microsparry calcite

Note: **Analytical totals were low (<90%) because the cements were very microporous. Therefore all data were normalised to 100%*

3.8 SAMPLE HG8 STN 37C

Sample HG8 STN 37C comprises pebbles of well-cemented fine-grained sandstone. The clasts are well-rounded and the surfaces show some 'weathering' with minor staining by finely-disseminated iron oxyhydroxide (Figure 57). In polished section, the sandstone is dark-grey due to the presence of finely-disseminated pyrite and probable organic matter. Fine sedimentary lamination can be seen and is contorted and disturbed (Figure 57).

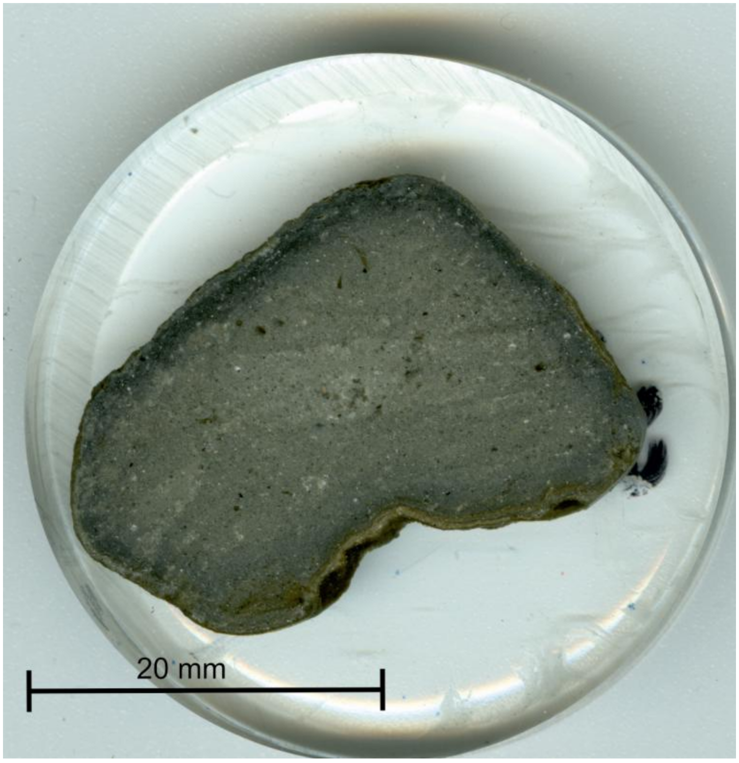

Figure 57. Polished section through a well-rounded clast of magnesian calcite-cemented fine sandstone. The section shows contorted fine sedimentary lamination with darker-grey and lighter grey banding reflecting probable variations in pyritic and organic-rich sandstone. The outer margins of the clast are stained by orange-brown iron oxyhydroxide. Sample HG8 STN 37C.

The petrology of this sample is very similar to that of samples HG8 STN 31B and HG8 STN 37B, and to that seen in many of the other carbonate-cemented samples dominated by high magnesian calcite cement. The detrital grains are dominated by silt- to fine sand-grade angular quartz, with minor to trace amounts of K-feldspar, plagioclase lithic clasts, and flakes of muscovite, with traces of iron and titanium oxides (Figure 58). The rock is characterised by an uncompacted detrital grain fabric, in which the detrital silicate grains show minimal grain contacts, with an intergranular matrix of micritic carbonate (Figure 58). As with the other samples, this uncompacted grain fabric indicates that cementation by the micritic carbonate occurred early in diagenesis, and prior to any significant burial.

The micritic matrix comprises fine grained high-magnesium calcite (Figure 58). This is generally tight but with patches of more porous sandstone retaining minor residual intergranular porosity (Figure 59). The porosity is lined or partly filled by microcolloform high magnesian calcite with morphology similar to that of the dolomite cement seen in sample HG6 STN 31C. The micritic calcite cement also preserves relicts of an original microcellular fabric that is similar to the microfabric seen in the other samples described previously, and is probably of microbial origin.

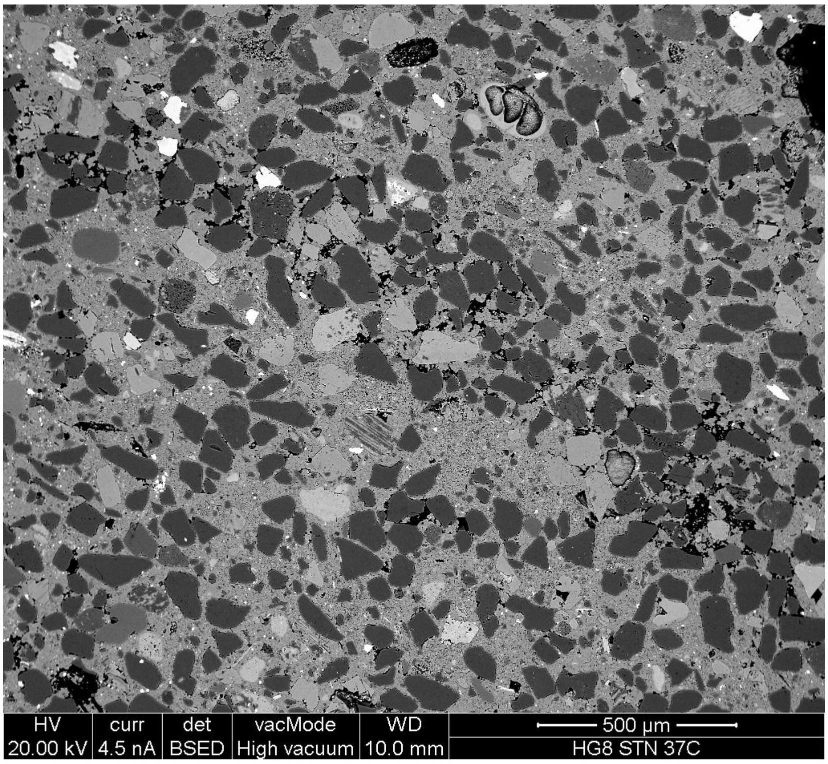

Figure 58. BSEM photomicrograph of the uncompacted detrital grain fabric of the fine sandstone, containing angular grains of quartz (dark-grey), K-feldspar (light-grey) and detrital iron oxide (white), 'floating' in a matrix of micritic high-magnesian calcite. The micrite can be seen to fill relatively large areas compared to the detrital grain size and probably represent faecal pellets. Sample HG8 STN 37C.

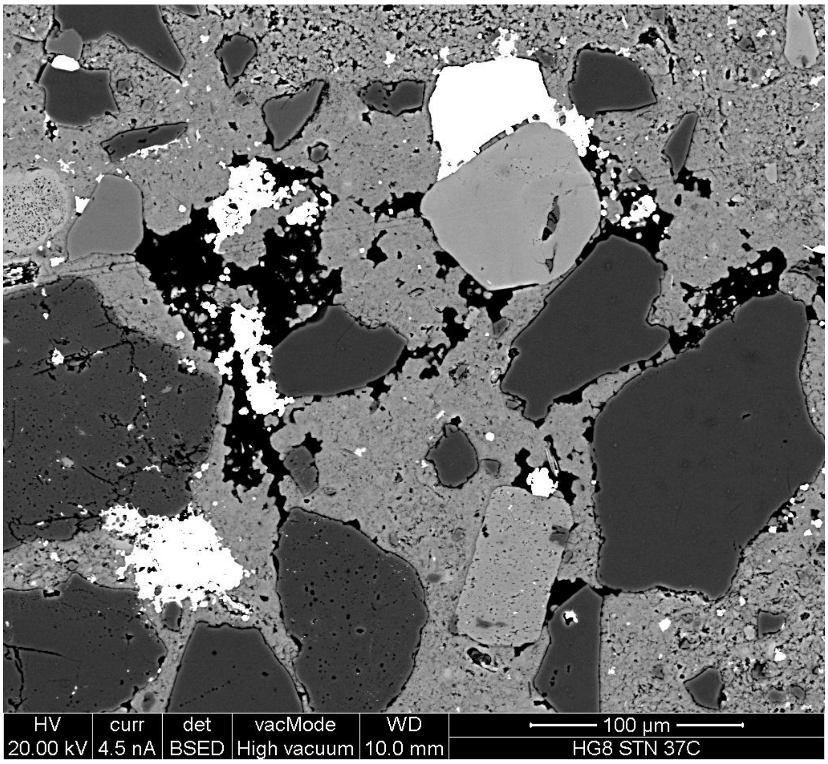

Figure 59. BSEM photomicrograph of showing residual intergranular porosity in sandstone partially cemented by microcolloform high-magnesian calcite. Microcrystalline and framboidal pyrite (white) line or partially-fill the porosity. Sample HG8 STN 37C.

A significant proportion of this matrix material occupies discrete large intergranular volumes that are oversized relative to the detrital grain size and state of compaction of the rock (Figure 58 and Figure 59). This suggests that these volumes of micrite were originally deposited as discrete, well-rounded, sand-grade ‘pelloidal grains composed of micritic carbonate, rather than as fine-grained micritic sediment. These micritic pelloidal grains may represent faecal pellets. This would imply that the precipitated micritic carbonate sediment was reworked by marine benthic organisms prior to lithification.

The micritic high-magnesian calcite was seen to be partially-replaced by later low magnesian calcite. The later calcite is coarser, and occurs in microsparry patches that overprint and obliterate the original micritic texture. It may also form fine crystals overgrowing the high-magnesian calcite lining residual pores.

Pyrite is abundant. It occurs finely disseminated through the micrite cement, and also as microcrystals and framboidal aggregates lining residual pores, where it rests on the colloform magnesian calcite on the pore walls (Figure 59).

Electron microprobe analyses of the calcite and dolomite cement are presented in Table 9. These data are summarised in Figure 60 in terms of molar proportions of end-member $CaCO_3$-$MgCO_3$-$FeCO_3$. The analyses of the early micritic magnesian calcite cement show that it is high-magnesian calcite with between 17 to 22 mole % $MgCO_3$ in solid-solution (Figure 60). This is similar to micritic magnesian calcite found in the other samples from the Braemar Pockmark. The analyses for the later calcite indicate that the minor recrystallisation of the magnesian calcite micrite to coarser microsparry calcite produced a relatively-low magnesium calcite (Figure 60) with between 3-9 mole % $MgCO_3$ in sold solution, which is again similar to the later calcite observed in other samples.

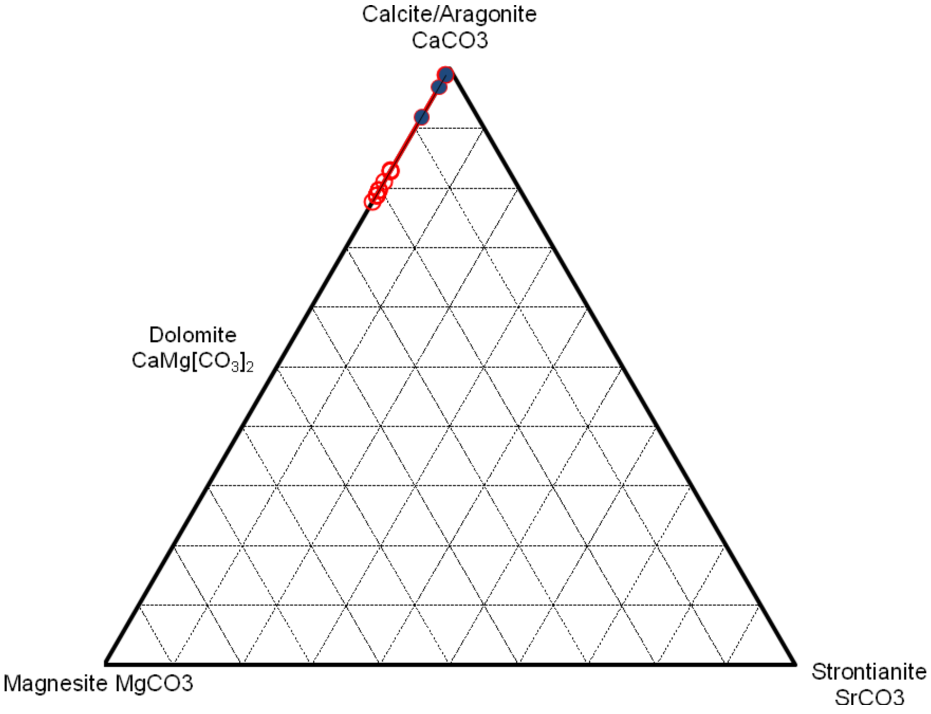

Figure 60. $CaCO_3$-$MgCO_3$-$SrCO_3$ molar ratio plot illustrating the compositions of the late calcite cement (solid blue circles) replacing the micritic high magnesian calcite (open red circles). MDAC sample HG8 STN 37C, relative to end-member carbonate minerals.

Table 9. Electron microprobe analyses of carbonate cements in sample HG8 STN 37C.

No.	WEIGHT % OXIDE (normalised)							IONIC RATIO [normalised to 3 [O]						COMMENTS
	MgO	CaO	MnO	FeO	SrO	CO_2 (calc)	*Total wt%	Mg^{2+}	Ca^{2+}	Mn^{2+}	Fe^{2+}	Sr^{2+}	CO_3^{2-}	
1	8.25	45.08	0.01	1.24	0.19	45.22	100.00	0.20	0.78	0.00	0.02	0.00	1.00	Micritic high magnesian calcite cement
2	6.88	47.33	-0.03	0.47	0.30	45.04	100.00	0.17	0.82	0.00	0.01	0.00	1.00	Micritic high magnesian calcite cement
3	8.75	45.27	0.03	0.45	0.08	45.41	100.00	0.21	0.78	0.00	0.01	0.00	1.00	Micritic high magnesian calcite cement
4	7.21	47.15	0.00	0.24	0.27	45.13	100.00	0.17	0.82	0.00	0.00	0.00	1.00	Micritic high magnesian calcite cement
5	7.72	46.72	-0.04	0.22	0.13	45.25	100.00	0.19	0.81	0.00	0.00	0.00	1.00	Micritic high magnesian calcite cement
6	8.92	45.08	0.03	0.36	0.19	45.42	100.00	0.21	0.78	0.00	0.00	0.00	1.00	Micritic high magnesian calcite cement
7	6.93	47.58	-0.02	0.24	0.17	45.10	100.00	0.17	0.83	0.00	0.00	0.00	1.00	Micritic high magnesian calcite cement
8	8.93	45.06	0.02	0.52	0.03	45.44	100.00	0.21	0.78	0.00	0.01	0.00	1.00	Micritic high magnesian calcite cement
9	8.94	45.18	0.00	0.17	0.28	45.43	100.00	0.21	0.78	0.00	0.00	0.00	1.00	Micritic high magnesian calcite cement
10	8.51	45.28	-0.02	0.65	0.28	45.31	100.00	0.20	0.78	0.00	0.01	0.00	1.00	Micritic high magnesian calcite cement
11	9.30	44.73	-0.01	0.27	0.21	45.50	100.00	0.22	0.77	0.00	0.00	0.00	1.00	Micritic high magnesian calcite cement
12	8.25	45.08	0.01	1.24	0.19	45.22	100.00	0.20	0.78	0.00	0.02	0.00	1.00	Micritic high magnesian calcite cement
13	6.88	47.33	-0.03	0.47	0.30	45.04	100.00	0.17	0.82	0.00	0.01	0.00	1.00	Micritic high magnesian calcite cement
14	0.48	54.45	0.05	0.96	0.14	43.92	100.00	0.01	0.97	0.00	0.01	0.00	1.00	Late calcite microspar replacing micritic calcite cement
15	3.45	51.74	0.03	0.07	0.19	44.51	100.00	0.08	0.91	0.00	0.00	0.00	1.00	Late calcite microspar replacing micritic calcite cement
16	0.58	54.27	0.06	1.00	0.17	43.93	100.00	0.01	0.97	0.00	0.01	0.00	1.00	Late calcite microspar replacing micritic calcite cement
17	1.12	53.71	0.06	0.82	0.27	44.02	100.00	0.03	0.96	0.00	0.01	0.00	1.00	Late calcite microspar replacing micritic calcite cement

***Note:** *Analytical totals were low (<90%) because the cements were very microporous. Therefore all data were normalised to 100%*

The sequence of sedimentary and post-depositional diagenetic events is similar to sample HG8 STN 37B, and can be summarised as follows:

1. Deposition of fine sand sediment;
2. Microbial precipitation of micritic high-magnesian calcite within the near-surface of the sediment, accompanied by the precipitation of authigenic pyrite.
3. Syndepositional bioturbation and reworking of the sediment, and redeposition of micrite as sand-grade faecal pellets prior to lithification;
4. Partial recrystallisation and replacement of micritic high-magnesian calcite by lower magnesian calcite;
5. Precipitation of pyrite in residual pores and cavities in the rock
6. Erosion of the lithified sediment, with abrasion of eroded clasts. and minor oxidation of pyrite near the surface of the clast.

3.9 SAMPLE HG9 STN 30A

Sample HG9 STN 30A comprised a series of fragments of dark grey to light brownish grey carbonate-cemented fine sandstone and siltstone ranging in size from 10-120 mm diameter. The fragments were typically irregular in form, varying from lenticular subrounded plates to subrounded and sub-angular elongate forms that appear to be cemented sediment-filled burrow-like structures (Figure 61). Some of the fragments are abraded and rounded, and the surfaces of the fragments are commonly bored by marine organisms.

Figure 61. Photograph showing the range of shapes and sizes of the fragments of carbonate cemented sandstone and siltstone in sample HG9 STN 30A. The fragments are highly irregular but some are moderately well rounded, and may also be bored by marine biota.

The rounded pebble examined in polished section is very similar to HG8 STN 37C. It is a moderately dark-grey fine sandstone with porous margins oxidised and stained orange-brown by finely disseminated iron oxyhydroxide. Traces of fine sedimentary lamination can also be seen but are discontinuous and have been disturbed by bioturbation (burrowing). This must have occurred prior to lithification when the sediment was still soft. The sandstone is very similar to the other magnesian-calcite-cemented samples (described above) in regard to its detrital mineralogy. It also has an uncompacted grain fabric (Figure 62), which indicates that cementation and lithification must have occurred early in diagenesis and before any significant burial.

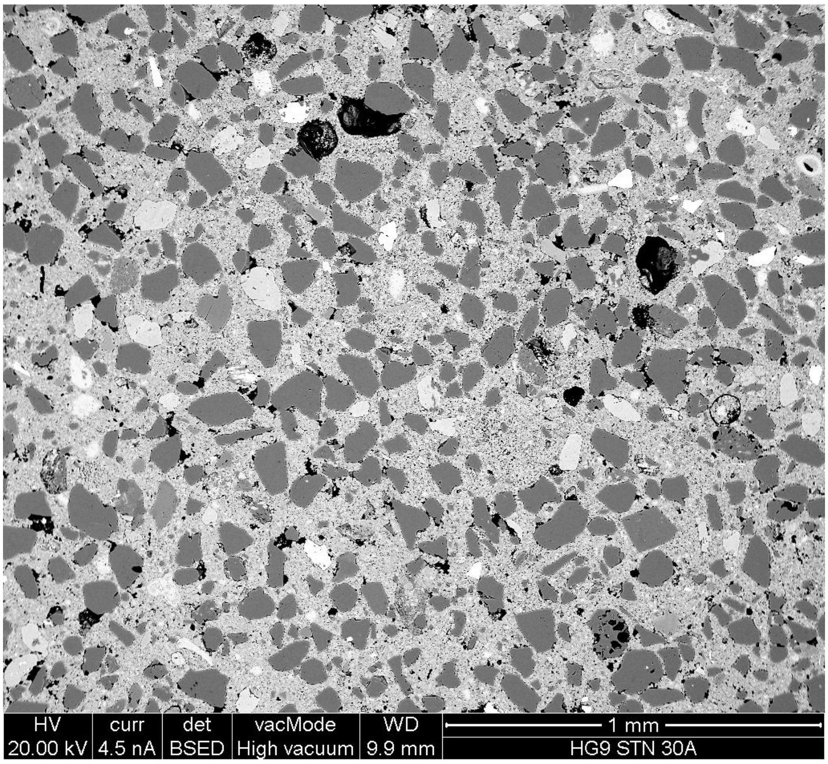

Figure 62. BSEM photomicrograph showing typical uncompacted grain fabric with angular detrital grains of fine sand, which are tightly-cemented by partially recrystallised interstitial micritic high-magnesian calcite (light-grey). Oversized areas of micritic high-magnesian calcite represent pelloidal grains. Sample HG9 STN 30A.

The micritic matrix comprises fine grained high-magnesium calcite (Figure 63). This comprises microcolloform, microglobular or microspheroidal aggregates of very fine grained calcite, which have coalesced to form a microporous cement with fine residual microporosity. The micritic calcite cement also preserves relicts of an original microcellular fabric similar to that described in some of the other samples, and which is probably of microbial origin.

A significant proportion of this matrix material occupies discrete large intergranular volumes that are oversized relative to the detrital grain size and state of compaction of the rock (Figure 62). This suggests that some of the micrite was originally deposited as discrete, well-rounded, sand-grade ‘pelloidal grains composed of micritic carbonate, rather than as fine-grained micritic sediment. These micritic pelloidal grains may represent faecal pellets. As described previously, this implies that the micritic carbonate sediment was reworked by marine benthic organisms prior to lithification.

The micritic high-magnesian calcite is partially-replaced by later low-magnesian calcite. Although fine grained, this later calcite is coarser than the magnesian calcite and occurs in microsparry patches that locally overprint and obliterate the original micritic texture. The late calcite also occurs overgrowing the high-magnesian calcite lining residual pores.

Pyrite is abundant. It occurs finely disseminated through the micrite cement, and also as microcrystals and framboidal aggregates lining residual pores, where it rests on the colloform magnesian calcite on the pore walls (Figure 63).

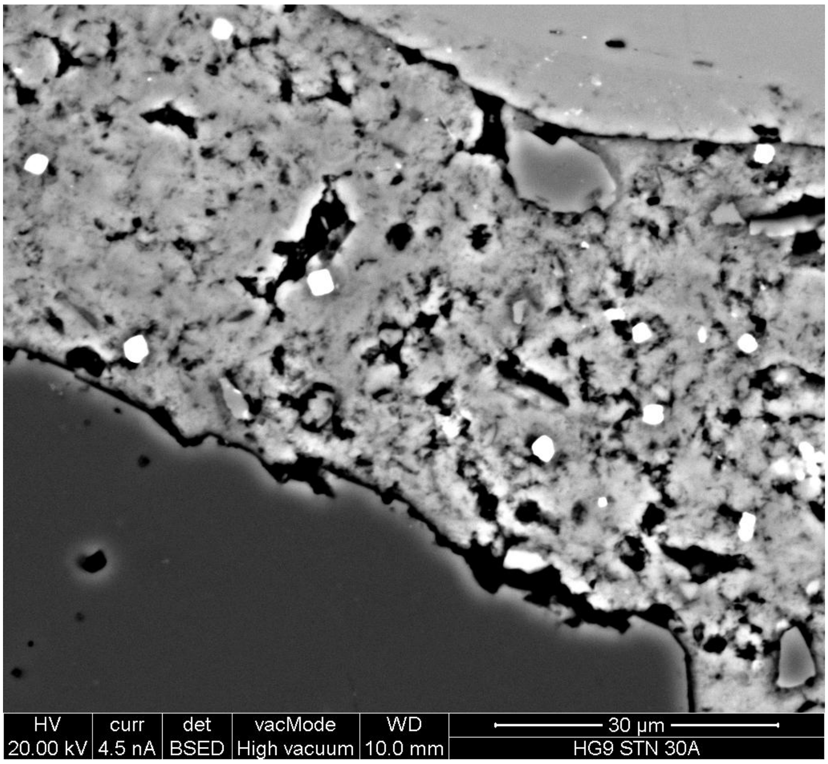

Figure 63. BSEM photomicrograph of the micritic high-magnesian calcite showing fabric of coalescing microglobular or microspheroidal calcite, with fine residual microporosity (black). Microcrystalline pyrite (white) is disseminated through the micritic carbonate. Sample HG8 STN 37C.

Electron microprobe analyses of the calcite and dolomite cement are presented in Table 10. These data are summarised in Figure 64 in terms of molar proportions of end-member $CaCO_3$-$MgCO_3$-$FeCO_3$. The analyses of the early micritic magnesian calcite cement show that it is high-magnesian calcite with between 16 to 26 mole % $MgCO_3$ in solid-solution (Figure 64). This is similar to micritic magnesian calcite found in the other samples from the Braemar Pockmark. The analyses for the later calcite indicate that the minor recrystallisation of the magnesian calcite micrite to coarser microsparry calcite produced a relatively-low magnesium calcite (Figure 64) with between 1-2 mole % $MgCO_3$ in sold solution, which is again similar to the later calcite observed in other samples.

The sequence of sedimentary and post-depositional diagenetic events can be summarised as follows:

1. Deposition of fine sand sediment;
2. Microbial precipitation of micritic high-magnesian calcite within the near-surface of the sediment, accompanied by the precipitation of authigenic pyrite.
3. Syndepositional bioturbation and reworking of the soft sediment, and redeposition of micrite as sand-grade faecal pellets prior to lithification;

4. Partial recrystallisation and replacement of micritic high-magnesian calcite by lower magnesian calcite;
5. Precipitation of pyrite in residual pores and cavities in the rock
6. Erosion of the lithified sediment, with abrasion of eroded clasts. and minor oxidation of pyrite near the surface of the clast.

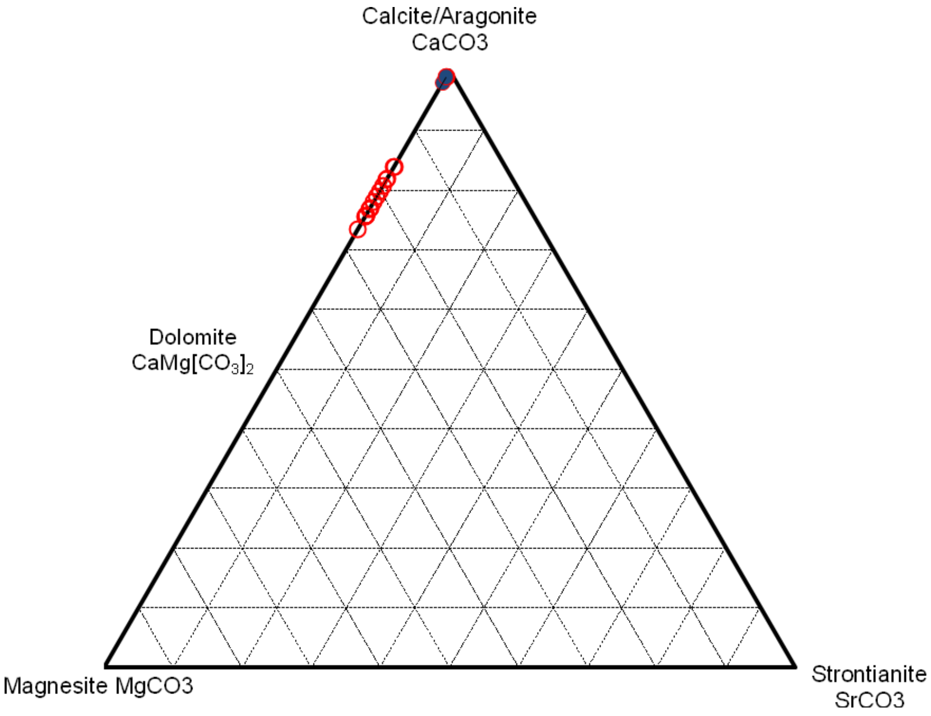

Figure 64. $CaCO_3$-$MgCO_3$-$SrCO_3$ molar ratio plot illustrating the compositions of the late calcite cement (solid blue circles) replacing the micritic high magnesian calcite (open red circles). MDAC sample HG9 STN 30A, relative to end-member carbonate minerals.

Table 10. Electron microprobe analyses of carbonate cements in sample HG9 STN 30A

No.	WEIGHT % OXIDE (normalised)							IONIC RATIO [normalised to 3 [O]						COMMENTS
	MgO	CaO	MnO	FeO	SrO	CO_2 (calc)	*Total wt%	Mg^{2+}	Ca^{2+}	Mn^{2+}	Fe^{2+}	Sr^{2+}	CO_3^{2-}	
1	8.66	45.66	0.00	0.00	0.27	45.40	100.00	0.21	0.79	0.00	0.00	0.00	1.00	micritic high magnesian calcite
2	6.76	47.92	0.00	0.00	0.24	45.08	100.00	0.16	0.83	0.00	0.00	0.00	1.00	micritic high magnesian calcite
3	10.20	43.64	0.00	0.33	0.18	45.65	100.00	0.24	0.75	0.00	0.00	0.00	1.00	micritic high magnesian calcite
4	10.23	43.48	0.00	0.62	0.00	45.66	100.00	0.24	0.75	0.00	0.01	0.00	1.00	micritic high magnesian calcite
5	9.43	44.24	0.00	0.62	0.22	45.48	100.00	0.23	0.76	0.00	0.01	0.00	1.00	micritic high magnesian calcite
6	9.93	43.55	0.00	0.79	0.18	45.56	100.00	0.24	0.75	0.00	0.01	0.00	1.00	micritic high magnesian calcite
7	10.71	42.09	0.00	1.24	0.33	45.62	100.00	0.26	0.72	0.00	0.02	0.00	1.00	micritic high magnesian calcite
8	10.14	43.28	0.00	0.77	0.23	45.59	100.00	0.24	0.74	0.00	0.01	0.00	1.00	micritic high magnesian calcite
9	9.48	44.75	0.00	0.00	0.22	45.55	100.00	0.23	0.77	0.00	0.00	0.00	1.00	micritic high magnesian calcite
10	10.19	43.85	0.00	0.00	0.30	45.66	100.00	0.24	0.75	0.00	0.00	0.00	1.00	micritic high magnesian calcite
11	7.57	46.72	0.00	0.24	0.29	45.19	100.00	0.18	0.81	0.00	0.00	0.00	1.00	micritic high magnesian calcite
12	8.09	46.37	0.00	0.00	0.24	45.31	100.00	0.19	0.80	0.00	0.00	0.00	1.00	micritic high magnesian calcite
13	9.27	44.98	0.00	0.00	0.23	45.51	100.00	0.22	0.78	0.00	0.00	0.00	1.00	micritic high magnesian calcite
14	8.50	45.84	0.00	0.00	0.30	45.37	100.00	0.20	0.79	0.00	0.00	0.00	1.00	micritic high magnesian calcite
15	6.44	48.23	0.00	0.00	0.33	45.01	100.00	0.16	0.84	0.00	0.00	0.00	1.00	micritic high magnesian calcite
16	7.34	47.13	0.00	0.00	0.37	45.15	100.00	0.18	0.82	0.00	0.00	0.00	1.00	micritic high magnesian calcite
17	9.62	44.60	0.00	0.00	0.21	45.58	100.00	0.23	0.77	0.00	0.00	0.00	1.00	micritic high magnesian calcite
18	0.64	55.28	0.00	0.00	0.00	44.08	100.00	0.02	0.98	0.00	0.00	0.00	1.00	Later calcite replacing high magnesian calcite
19	0.56	55.30	0.00	0.08	0.00	44.05	100.00	0.01	0.98	0.00	0.00	0.00	1.00	Later calcite replacing high magnesian calcite
20	0.25	55.40	0.00	0.10	0.31	43.94	100.00	0.01	0.99	0.00	0.00	0.00	1.00	Later calcite replacing high magnesian calcite

***Note:** *Analytical totals were low (<90%) because the cements were very microporous. Therefore all data were normalised to 100%*

3.10 SAMPLE HG10 STN 29A

Sample HG10 STN 29A comprised a series of fragments of dark grey to light brownish grey, and cream-coloured clasts of carbonate-cemented fine sandstone and siltstone ranging in size from 30-90 mm diameter. The fragments were typically irregular in form and often ‘clinker-like’ (Figure 65). Some of the fragments are abraded and well-rounded, and the surfaces of the fragments are commonly bored by marine organisms. Red-brown iron oxide staining is seen in some fragments, indicating that they have suffered oxidative weathering following erosion.

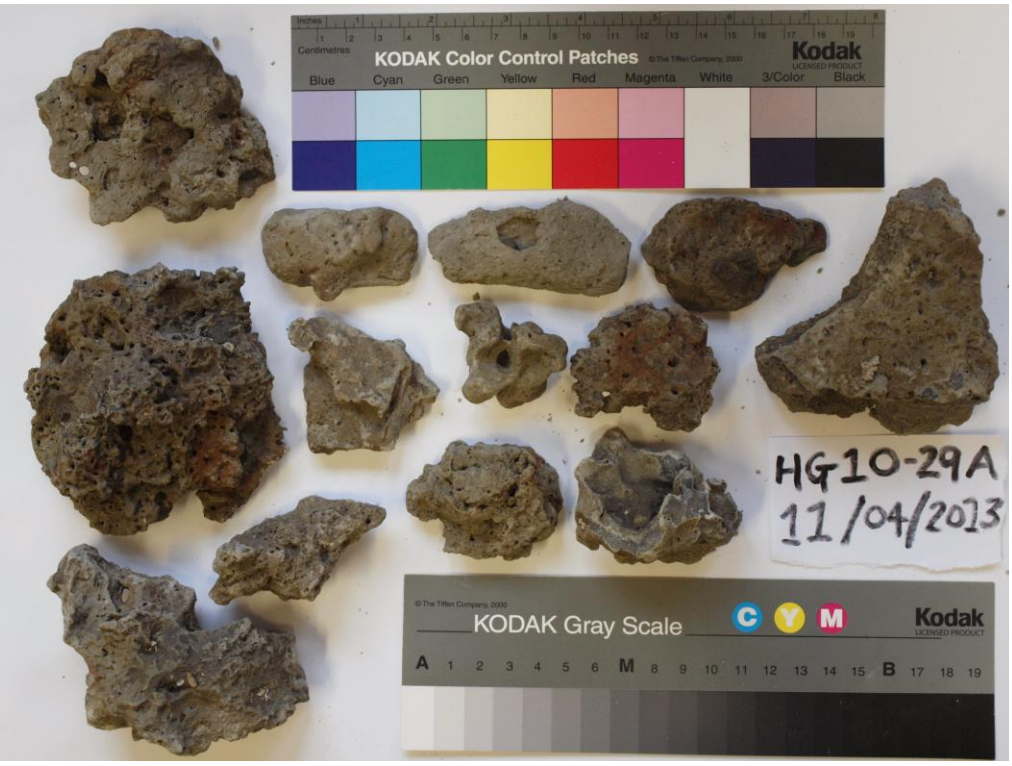

Figure 65. Photograph showing the range of shapes and sizes of the fragments of carbonate cemented sandstone and siltstone in sample HG10 STN 29A. The fragments are highly irregular but some are moderately well rounded, and may also be bored by marine biota.

The detrital mineralogy of the sandstone is similar to that described in the previous samples. The rock has an uncompacted grain fabric (Figure 66) indicative of very early diagenetic lithification prior to significant burial. The quartz grains also display some etching and corrosion (Figure 66). This rock is cemented by micritic dolomite rather than micritic high-magnesian calcite (Figure 66).

The micritic dolomite matrix is very similar to that seen in sample HG6 STN 31C (Section 3.5). High-resolution BSEM observations show that the micritic dolomite preserves a well-developed microcellular fabric, comprising aggregates of dolomite microcrystals typically less than 1 μm in size that have nucleated around or encrusting a single central microcavity or clusters of microcavities about 1-2 μm in diameter (Figure 67 and Figure 68). These structures very closely resemble fossilised and mineralised bacterial cells described from experimental studies and other environments in the literature (cf. Martill and Wilby, 1994; Wilby and Whyte, 1995). Denser areas of cementation have formed as these microcellular structures coalesce and become more compacted. Similar dolomite fabrics were also observed by Milodowski et al. (2009) from MDAC samples studied from the Mid Irish Sea. However, the dolomite-mineralised microcellular structures are better preserved in the Braemar Pockmark samples.

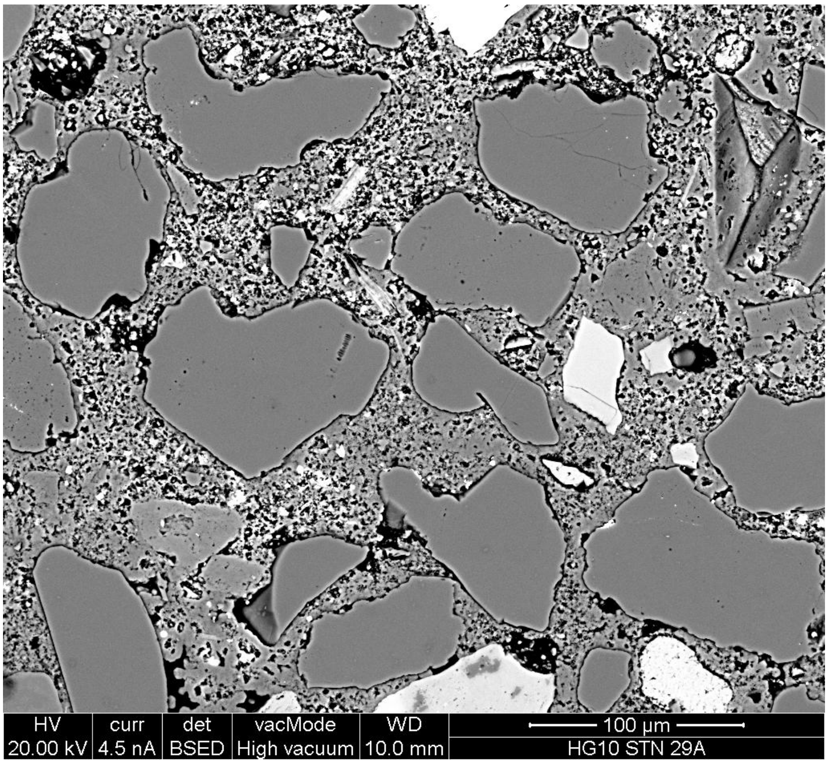

Figure 66. BSEM photomicrograph showing typical uncompacted grain fabric with angular detrital grains of fine sand, which are well-cemented by interstitial microporous micritic dolomite (light-grey). Oversized intergranular areas of micritic dolomite may represent pelloidal grains. Sample HG10 STN 29A.

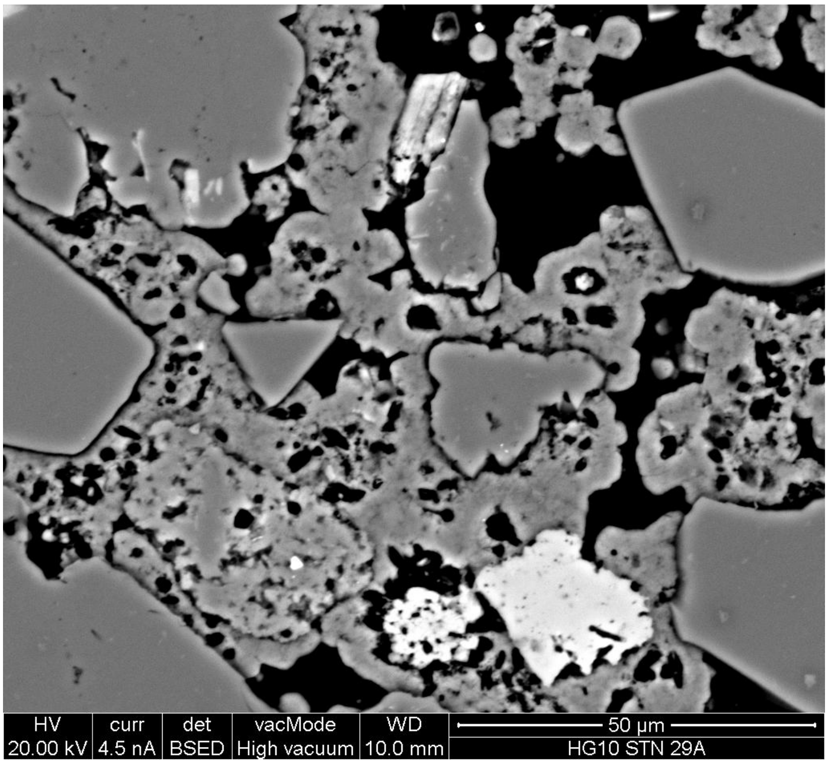

Figure 67. BSEM photomicrograph showing the detail of the micritic dolomite cement. The dolomite preserves a well-developed cellular microfabric that represents mineralised bacterial cells. Pyrite (white) occurs in some of the dolomite-mineralised cells and also partially fills residual micropores. Sample HG10 STN 29A.

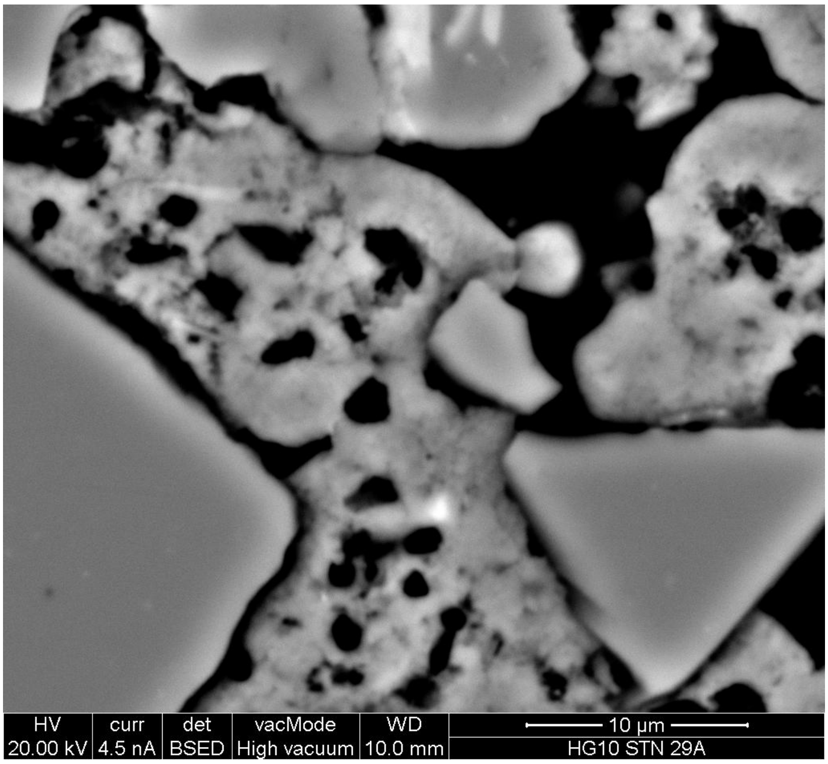

Figure 68. BSEM photomicrograph showing the detail of the micritic dolomite cement. The dolomite preserves a well-developed cellular microfabric that represents mineralised bacterial cells. Sample HG10 STN 29A.

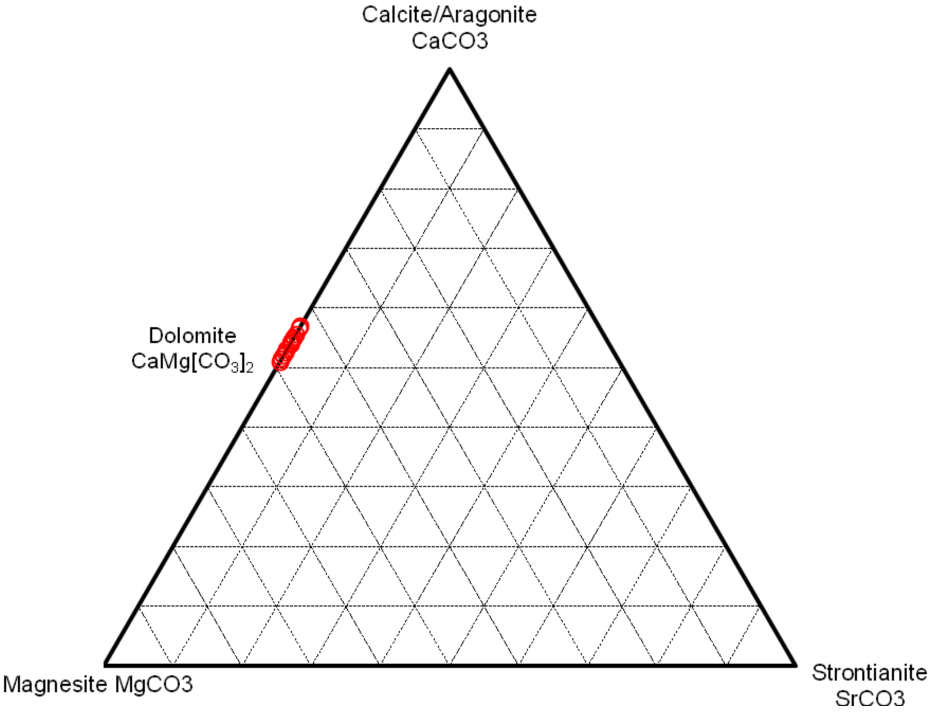

Figure 69. $CaCO_3$-$MgCO_3$-$SrCO_3$ molar ratio plot illustrating the compositions of the micritic dolomite cement (open red circles). MDAC sample HG10 STN 29A, relative to end-member carbonate minerals.

Authigenic pyrite is intimately associated with the dolomite. It occurs as microcrystals within the cavities in dolomite micrite, enclosed with the dolomicrite cement, and as framboidal aggregates lining the residual microporosity between the microcellular aggregates of dolomite (Figure 67). This suggests that dolomite formation was occurring at the same time as sulphate and iron reduction was taking place in the original sediment.

EPMA analyses of the carbonate cements are presented in Table 11 and are summarised in Figure 69. The dolomite cement is characterised by calcium-rich dolomite (composition of $Ca_{0.59-0.53}Mg_{0.01-0.07}CO_3$), with 1-7 mole % Ca in excess of the ideal stoichiometry for dolomite $Ca_{0.5}Mg_{0.5}CO_3$. This composition is very similar to that of the dolomite described from sample HG6 STN 31C.

The sequence of sedimentary and post-depositional diagenetic events recorded from sample HG10 STN 29A is very similar to that observed in the other samples from the Braemar Pockmark, and can be summarised as follows:

1. Deposition of fine sand and silt sediment;
2. Microbial precipitation of micritic dolomite within the near-surface of the sediment, and precipitation of authigenic pyrite associated with iron and sulphate reduction in sediment.
3. Syndepositional bioturbation and reworking of the dolomicritic sediment associated with the production of pelloidal grains of dolomicrite (possibly faecal pellets);
4. Ongoing microbial precipitation of micritic dolomicrite and lithification, accompanied by further precipitation of authigenic pyrite;
5. Erosion of the lithified sediment and abrasion of the eroded clasts;
6. Boring of the clast surfaces by marine biota, and oxidation of pyrite near the clast surface.

Table 11. Electron microprobe analyses of carbonate cements in sample HG10 STN 29A

No.	WEIGHT % OXIDE (normalised)							IONIC RATIO [normalised to 3 [O]						COMMENTS
	MgO	CaO	MnO	FeO	SrO	CO_2 (calc)	*Total wt%	Mg^{2+}	Ca^{2+}	Mn^{2+}	Fe^{2+}	Sr^{2+}	CO_3^{2-}	
1	20.31	31.81	0.00	0.26	0.23	47.39	100.00	0.47	0.53	0.00	0.00	0.00	1.00	micritic dolomite
2	19.56	31.60	0.00	1.25	0.47	47.11	100.00	0.45	0.53	0.00	0.02	0.00	1.00	micritic dolomite
3	19.97	32.39	0.00	0.00	0.30	47.34	100.00	0.46	0.54	0.00	0.00	0.00	1.00	micritic dolomite
4	19.73	32.58	0.00	0.13	0.28	47.29	100.00	0.46	0.54	0.00	0.00	0.00	1.00	micritic dolomite
5	18.75	33.40	0.00	0.45	0.32	47.08	100.00	0.43	0.56	0.00	0.01	0.00	1.00	micritic dolomite
6	19.23	32.89	0.00	0.39	0.31	47.17	100.00	0.45	0.55	0.00	0.01	0.00	1.00	micritic dolomite
7	18.33	33.92	0.00	0.71	0.00	47.05	100.00	0.43	0.57	0.00	0.01	0.00	1.00	micritic dolomite
8	19.31	32.95	0.00	0.24	0.30	47.20	100.00	0.45	0.55	0.00	0.00	0.00	1.00	micritic dolomite
9	20.53	31.39	0.11	0.53	0.00	47.43	100.00	0.47	0.52	0.00	0.01	0.00	1.00	micritic dolomite
10	20.72	31.00	0.14	0.50	0.21	47.43	100.00	0.48	0.51	0.00	0.01	0.00	1.00	micritic dolomite
11	20.66	31.20	0.19	0.50	0.00	47.45	100.00	0.48	0.52	0.00	0.01	0.00	1.00	micritic dolomite
12	19.67	32.73	0.00	0.00	0.31	47.29	100.00	0.45	0.54	0.00	0.00	0.00	1.00	micritic dolomite
13	19.05	33.01	0.20	0.56	0.00	47.17	100.00	0.44	0.55	0.00	0.01	0.00	1.00	micritic dolomite
14	21.14	30.69	0.15	0.47	0.00	47.54	100.00	0.49	0.51	0.00	0.01	0.00	1.00	micritic dolomite
15	19.84	32.56	0.00	0.00	0.27	47.32	100.00	0.46	0.54	0.00	0.00	0.00	1.00	micritic dolomite
16	19.87	32.50	0.00	0.00	0.31	47.32	100.00	0.46	0.54	0.00	0.00	0.00	1.00	micritic dolomite

Note: **Analytical totals were low (<90%) because the cements were very microporous. Therefore all data were normalised to 100%*

3.11 SAMPLE HG10 STN 29B

This sample contained only a few small fragments (up to 45 mm) of carbonate-cemented siltstone to very fine sandstone (Figure 70). The fragments are highly irregular in shape, varying from a very rough-surfaced flat plate to an elongate clast resembling a burrow infill. Some abrasion and rounding of the clast surfaces is apparent, and the surfaces of the clasts are slightly stained by orange-brown iron oxyhydroxide. The largest of these clasts was examined petrographically.

Figure 70. Photograph showing the morphology of carbonate-cemented rock fragments in sample HG10 STN 29B. Many fragments are highly irregular and the central clast displays open burrows produced by marine organisms.

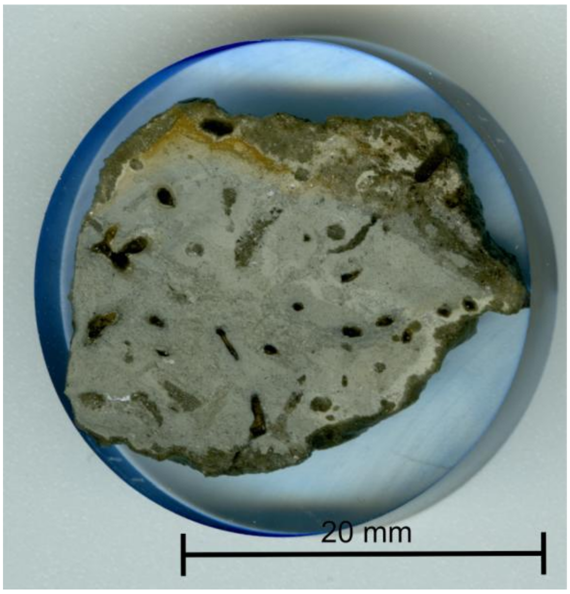

Figure 71. Polished section though a rounded clast from sample HG10 STN 29B. The clast can be seen to be extensively bored with fine open borings penetrating from the external surfaces. The rock displays a bioturbated fabric with irregular patches of more darker-grey porous sandy sediment filling burrows and wisps of lighter-grey, more muddy sediment.

The sedimentary fabric of the clast examined in polished section was seen to be disturbed by bioturbation, with sandy sediment filling burrow structures and discontinuous wisps of muddier sediment within (Figure 71). This bioturbation must have occurred before lithification while the sediment was still soft. Later boring structures are also present. These are represented by fine tubes with sharply defined walls that penetrate the clast from the surface all around its margins (Figure 71). These borings clearly post-date the lithification of the sediment and the subsequent erosion of the cemented rock. The outer margins of the clast are also weathered and stained yellow-brown by finely-disseminated iron oxyhydroxide (Figure 71).

The petrography of the sample is generally very similar to that described from the other dolomite-cemented samples HG6 STN 31C (Section 3.5) and HG10 STN 29A (Section 3.10). The rock is generally very well cemented largely by dolomite. The dolomite is micritic, with a fabric comprised mainly of tightly-coalescing microspheroidal or globular aggregates of dolomicrite (Figure 72). The dolomicrite is microporous and is intimately associated with abundant finely-disseminated pyrite.

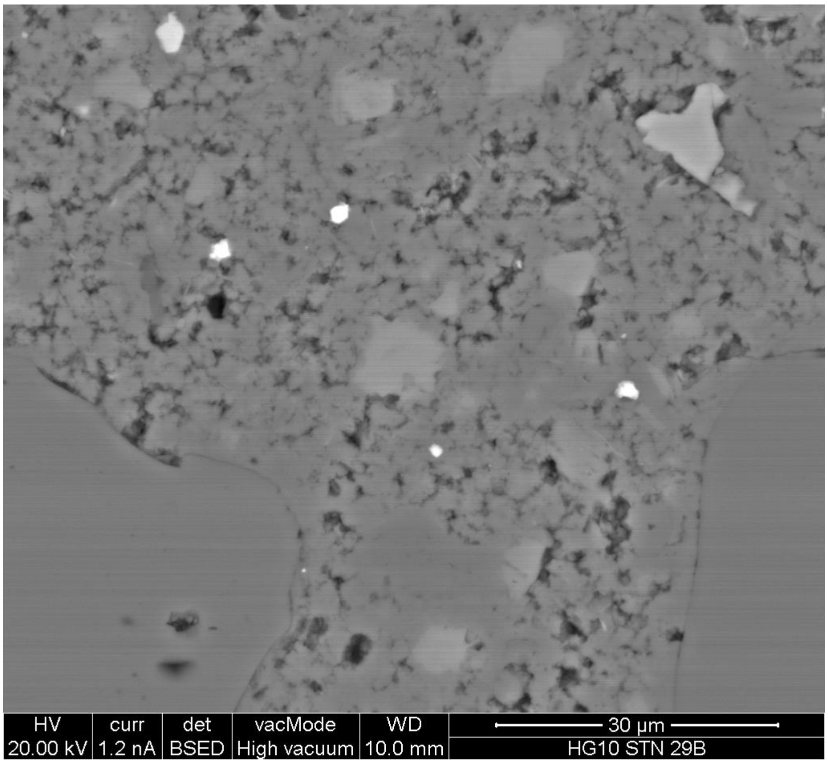

Figure 72. BSEM photomicrograph showing typical fabric of the interstitial microporous micritic dolomite (light-grey) within well-cemented parts of the dolomite-cemented sandstone. It shows tightly coalescing microspheroidal or globular aggregates of dolomicrite. Coarser rhombs of late-stage low-magnesian calcite (light-grey) have nucleated within the dolomite matrix, and replace the dolomite. Sample HG10 STN 29B.

The more porous areas of the sandstone correspond to burrow fills partially cemented by micritic dolomite. In these areas, the original dolomicrite fabric is best preserved, and is represented by fine globules or spheroidal aggregates of dolomite, which coat the walls of the intergranular pores (Figure 73). High-resolution BSEM observations show that many of these spheroidal microstructures have hollow ‘cores’ and the dolomite appears to have nucleated around microcavities about 1-2 µm in diameter (Figure 73). These structures are very similar to those described from samples HG6 STN 31C and HG10 STN 29 and resemble fossilised and mineralised bacterial cells.

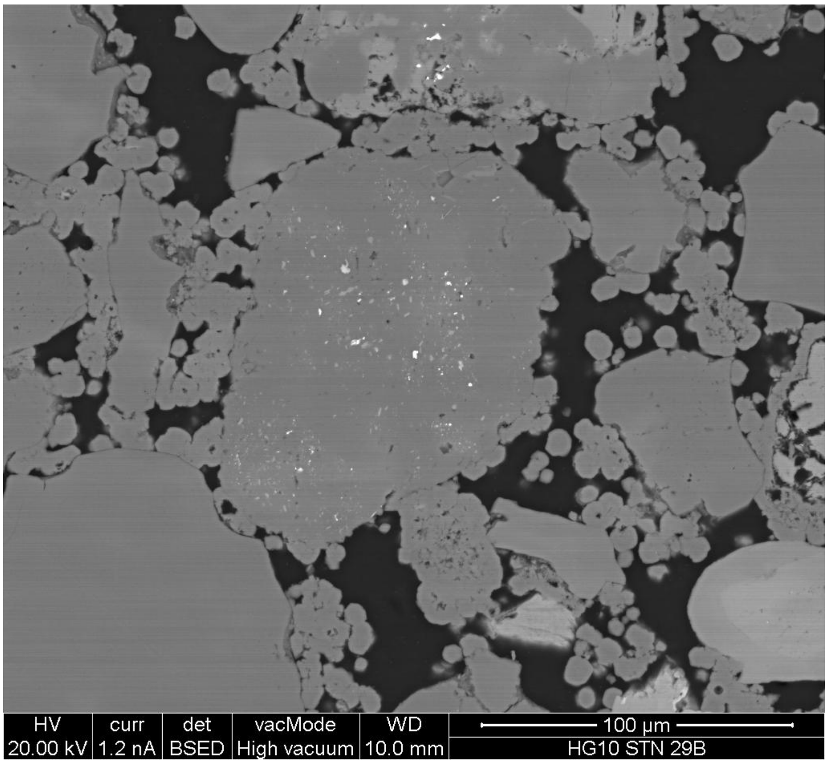

Figure 73. BSEM photomicrograph showing the detail of the micritic dolomite cement within porous sandy parts of the sample. The dolomite preserves a well-developed colloform, globular or spheroidal microfabric, with the dolomite encrusting intergranular pore walls. Some of the spheroids display cellular structures that possibly represent mineralised bacterial cells. Sample HG10 STN 29B.

The dolomite has been partially replaced by later low-magnesian calcite. This occurs as small rhombs which have nucleated within the dolomite and locally overprint the original dolomite fabric.

EPMA analyses of the carbonate cements are presented in Table 12 and are summarised in Figure 74. The dolomite cements are all very similar in composition and are characterised by calcium-rich dolomite (composition of $Ca_{0.50\text{-}0.54}Mg_{0.50\text{-}0.46}CO_3$), with 0-4 mole % Ca in excess of the ideal stoichiometry for dolomite $Ca_{0.5}Mg_{0.5}CO_3$. This is very similar to the excess Ca dolomites described from samples HG6 STN 31C and HG10 STN 29A.

The minor calcite seen replacing the dolomicrite cement is magnesian, with up 2-8 mole % $MgCO_3$ in solid-solution. It is much less magnesian that the primary micritic magnesian calcite cements seen in the other samples from the Braemar Pockmark. However, its composition is close to that of the secondary microsparry calcite seen to replace the micritic calcite in these rocks.

The sequence of sedimentary and post-depositional diagenetic events recorded from sample HG10 STN 29B is very similar to that observed in sample HG6 STN 31C, and can be summarised as follows:

1. Deposition of fine sand and silt sediment;
2. Microbial precipitation of micritic dolomite within the near-surface of the sediment, and precipitation of authigenic pyrite associated with iron and sulphate reduction in sediment.
3. Syndepositional bioturbation and reworking of the dolomicritic sediment associated with the production of pelloidal grains of dolomicrite (possibly faecal pellets);

4. Ongoing microbial precipitation of micritic dolomicrite and lithification, accompanied by further precipitation of authigenic pyrite;
5. Partial recrystallisation of the dolomicrite and replacement by low-magnesian calcite;
6. Erosion of the lithified sediment and abrasion of the eroded clasts;
7. Boring of the clast surfaces by marine biota, and oxidation of pyrite near the clast surface.

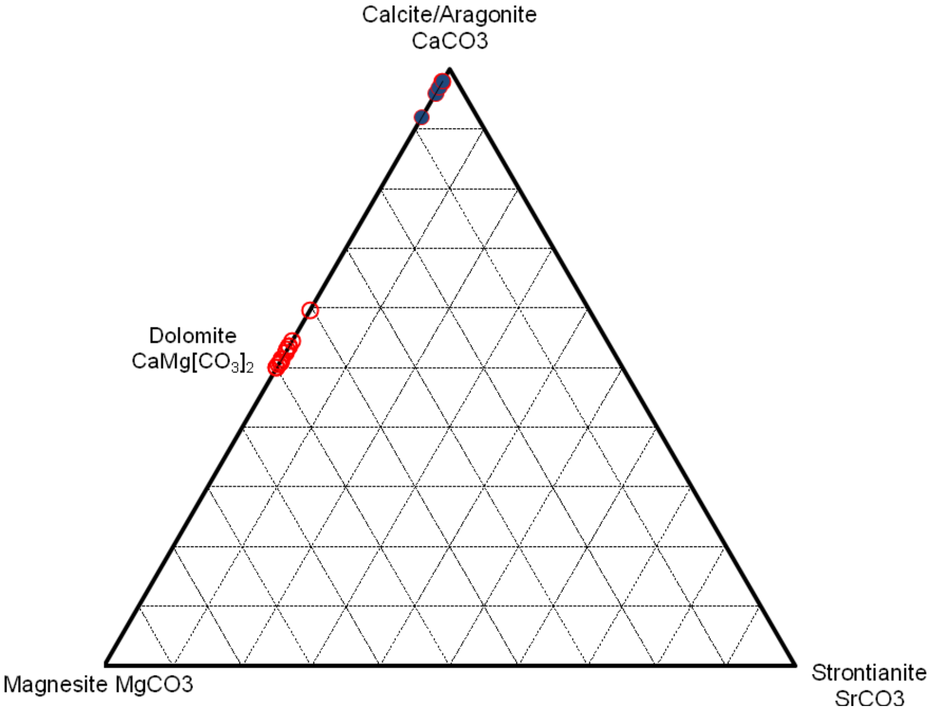

Figure 74. $CaCO_3$-$MgCO_3$-$SrCO_3$ molar ratio plot illustrating the compositions of the micritic dolomite cement (open red circles) and later replacive microsparry calcite (solid blue circles). MDAC sample HG10 STN 29B, relative to end-member carbonate minerals.

Table 12. Electron microprobe analyses of carbonate cements in sample HG10 STN 29B

No.	WEIGHT % OXIDE (normalised)							IONIC RATIO [normalised to 3 [O]						COMMENTS
	MgO	CaO	MnO	FeO	SrO	CO_2 (calc)	*Total wt%	Mg^{2+}	Ca^{2+}	Mn^{2+}	Fe^{2+}	Sr^{2+}	CO_3^{2-}	
1	20.46	31.30	0.00	0.85	0.00	47.40	100.00	0.47	0.52	0.00	0.01	0.00	1.00	micritic dolomite
2	19.78	32.09	0.00	0.85	0.00	47.29	100.00	0.46	0.53	0.00	0.01	0.00	1.00	micritic dolomite
3	19.96	31.88	0.00	0.84	0.00	47.32	100.00	0.46	0.53	0.00	0.01	0.00	1.00	micritic dolomite
4	20.68	31.05	0.00	0.84	0.00	47.44	100.00	0.48	0.51	0.00	0.01	0.00	1.00	micritic dolomite
5	17.37	35.27	0.00	0.46	0.00	46.91	100.00	0.40	0.59	0.00	0.01	0.00	1.00	micritic dolomite
6	20.27	31.91	0.00	0.40	0.00	47.41	100.00	0.47	0.53	0.00	0.01	0.00	1.00	micritic dolomite
7	19.39	32.81	0.00	0.56	0.00	47.25	100.00	0.45	0.54	0.00	0.01	0.00	1.00	micritic dolomite
8	19.86	32.17	0.00	0.65	0.00	47.32	100.00	0.46	0.53	0.00	0.01	0.00	1.00	micritic dolomite
9	21.07	30.96	0.00	0.41	0.00	47.55	100.00	0.48	0.51	0.00	0.01	0.00	1.00	micritic dolomite
10	21.45	30.89	0.00	0.00	0.00	47.65	100.00	0.49	0.51	0.00	0.00	0.00	1.00	micritic dolomite
11	21.48	30.86	0.00	0.00	0.00	47.66	100.00	0.49	0.51	0.00	0.00	0.00	1.00	micritic dolomite
12	21.38	30.98	0.00	0.00	0.00	47.64	100.00	0.49	0.51	0.00	0.00	0.00	1.00	micritic dolomite
13	21.84	30.44	0.00	0.00	0.00	47.72	100.00	0.50	0.50	0.00	0.00	0.00	1.00	micritic dolomite
14	21.53	30.81	0.00	0.00	0.00	47.67	100.00	0.49	0.51	0.00	0.00	0.00	1.00	micritic dolomite
15	21.50	30.48	0.00	0.40	0.00	47.62	100.00	0.49	0.50	0.00	0.01	0.00	1.00	micritic dolomite
16	21.90	30.36	0.00	0.00	0.00	47.73	100.00	0.50	0.50	0.00	0.00	0.00	1.00	micritic dolomite
17	1.59	54.01	0.00	0.18	0.00	44.22	100.00	0.04	0.96	0.00	0.00	0.00	1.00	Late calcite replacing micritic dolomite
18	3.16	52.08	0.00	0.27	0.00	44.48	100.00	0.08	0.92	0.00	0.00	0.00	1.00	Late calcite replacing micritic dolomite
19	1.30	54.38	0.00	0.14	0.00	44.17	100.00	0.03	0.97	0.00	0.00	0.00	1.00	Late calcite replacing micritic dolomite
20	0.93	54.95	0.00	0.00	0.00	44.12	100.00	0.02	0.98	0.00	0.00	0.00	1.00	Late calcite replacing micritic dolomite
21	0.91	54.97	0.00	0.00	0.00	44.12	100.00	0.02	0.98	0.00	0.00	0.00	1.00	Late calcite replacing micritic dolomite

***Note:** *Analytical totals were low (<90%) because the cements were very microporous. Therefore all data were normalised to 100%*

4 Stable isotope characteristics

4.1 GENERAL

The results of the stable isotope ($\delta^{13}C$ and $\delta^{18}O$) analyses of the micro-sampled carbonate material from the Braemar Pockmark MDAC samples, determined by the 'small carbonate analysis method (Section 2.2.1), are given in Table 13. The data represent carbonate sampled from discrete parts of each sample that were micro-sampled to try to extract discrete carbonate components or specific generations of carbonate cement. Fifty four of the micro-samples analysed by this method were successfully analysed, with only one sample failing (sub-sample 11-5: HG10 STN 29B). The relative locations of the micro-drilled sub-samples taken from the polished blocks for each MDAC sample are shown in Figure 75.

A comparison of the differences in the results of the 'small carbonate sample' and the 'classical' carbonate stable isotope analysis methods for selected dolomite samples is shown in Table 14. There is generally good agreement between the $\delta^{13}C$ and $\delta^{18}O$ data for dolomite derived by the two different methods. This demonstrates that the 'small carbonate sample analysis method' can be applied to the analysis of dolomite as well as calcite and aragonite.

The variation in the $\delta^{13}C$ and $\delta^{18}O$ composition of the MDAC carbonates (based on the 'small carbonate sample' analysis method - Section 2.2.1) is summarised in Figure 76. Three distinct groups of carbonate mineralisation can be differentiated on the basis of their carbon and oxygen stable isotope composition (Figure 76) that also correspond closely to the mineralogy of the cement and the relationship of the cement within the sequence described in Section 3:

- Aragonite cements with values ranging between -54.1 and -46.8 $‰_{PDB}$ for $\delta^{13}C$ and 2.4 and 3.4 $‰_{PDB}$ for $\delta^{18}O$;
- High magnesian calcite cements: with values ranging between -50.0 and -41.0 $‰_{PDB}$ for $\delta^{13}C$ and 3.0 and 4.5 $‰_{PDB}$ for $\delta^{18}O$;
- Dolomite cements: with values ranging between -33.0 and -18.0 $‰_{PDB}$ for $\delta^{13}C$ and 3.7 and 4.6 $‰_{PDB}$ for $\delta^{18}O$. The dolomite cements can be further subdivided on the basis their state of diagenetic alteration. Unaltered micritic dolomite cements, with pristine, well-preserved primary early diagenetic microcolloform and/or 'microcellular' fabrics (represented by sample HG10 STN 29B) have distinctly heavier $\delta^{13}C$ values varying from -22.7 to -18.7 $‰_{PDB}$ than dolomite cements which have been partially, recrystallised and / or partially replaced and mineralised by minor later microsparry calcite (represented by samples HG10 STN 29A and HG6 STN 31C) with carbon as light as -33 $‰_{PDB}$ $\delta^{13}C$, and trending more closely towards the upper end of the range for high magnesian calcite cements (Figure 76).

Figure 77 illustrates the stable isotope composition of MDAC samples from the Mid Irish Sea that were studied previously by Milodowski et al. (2009). Comparison of this data with the data from the present study (Figure 77) shows that the high-magnesian calcites and aragonites from the Braemar Pockmark have broadly similar stable isotope compositions to those encountered in the Mid Irish Sea. However, the dolomite cements from the Braemar Pockmark have considerably heavier $\delta^{13}C$ and slightly heavier $\delta^{18}O$ than dolomite cements from the Mid Irish Sea.

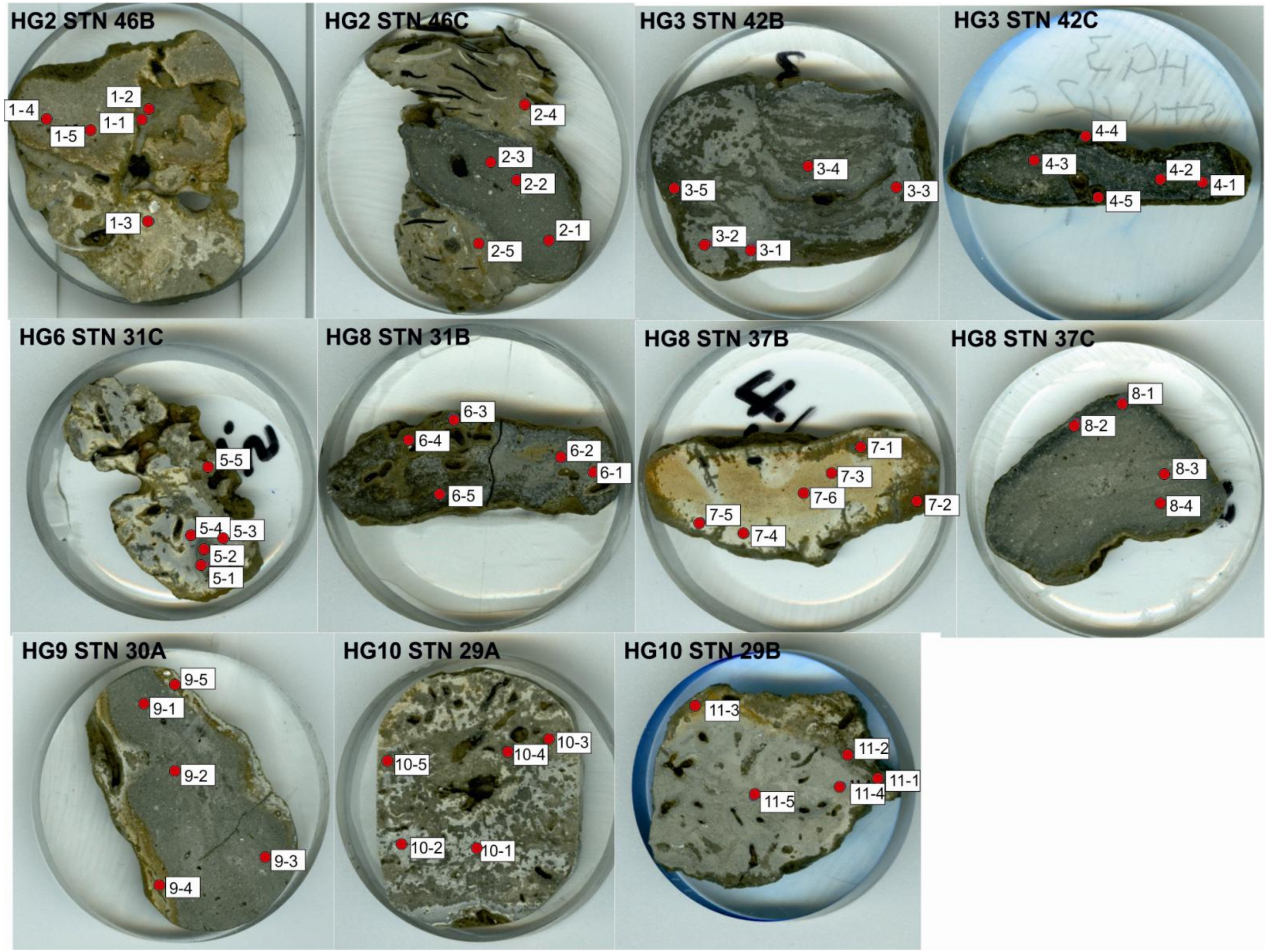

Figure 75. Position of micro-drilled material taken for stable isotope analysis from the polished blocks for each MDAC sample

Table 13. Stable isotope analyses ($\delta^{13}C$ and $\delta^{18}O$) for micro-sampled carbonate components from the MDAC samples (small carbonate analysis method)

Sample	Sub-sample	$\delta^{13}C_{PDB}$ (‰)	$\delta^{18}O_{PDB}$ (‰)	Mineral	Description
HG2 STN 46B	1-1	-52.24	+3.15	Aragonite	Acicular aragonite cement in boring or burrow in high Mg-calcite-cemented fine sandstone
HG2 STN 46B	1-2	-53.24	+3.39	Aragonite	
HG2 STN 46B	1-3	-54.10	+2.61	Aragonite	
HG2 STN 46B	1-3*	-53.95	+2.45	Aragonite	Acicular aragonite cemented silt resting eroded Mg-calcite-cemented fine sandstone
HG2 STN 46B	1-4	-48.77	+3.09	Mg-calcite	Micritic high Mg-calcite-cemented matrix of fine sandstone near centre of clast
HG2 STN 46B	1-5	-49.35	+4.01	Mg calcite	Micritic high Mg-calcite-cemented matrix of fine sandstone from oxidised margin of clast
HG2 STN 46C	2-1	-47.58	+3.76	Mg-calcite	Micritic high Mg-calcite-cemented matrix of well-rounded fine sandstone-siltstone clast enclosed within later aragonite-cemented shelly siltstone
HG2 STN 46C	2-2	-47.02	+3.93	Mg-calcite	
HG2 STN 46C	2-3	-46.63	+4.01	Mg-calcite	
HG2 STN 46C	2-4	-46.87	+3.32	Aragonite	Acicular to micritic aragonite cement forming the matrix of very shelly siltstone enclosing well-rounded clasts of high Mg-calcite cemented fine sandstone-siltstone
HG2 STN 46C	2-5	-47.35	+3.39	Aragonite	
HG3 STN 42B	3-1	-45.52	+3.81	Mg-calcite	Dense micritic carbonate cement within slightly oxidised margin of carbonate-cemented clast
HG3 STN 42B	3-2	-45.43	+3.63	Mg-calcite	
HG3 STN 42B	3-3	-46.03	+3.89	Mg-calcite	
HG3 STN 42B	3-4	-45.99	+3.66	Mg-calcite	Very porous micritic carbonate cement within centre of carbonate-cemented clast
HG3 STN 42B	3-5	-45.89	+3.55	Mg-calcite	Very porous micritic carbonate cement within margin of carbonate-cemented clast

Note: * replicate analysis

Table 13 (continued). Stable isotope analyses ($\delta^{13}C$ and $\delta^{18}O$) for micro-sampled carbonate components from the MDAC samples (small carbonate analysis method)

Sample	Sub-sample	$\delta^{13}C_{PDB}$ (‰)	$\delta^{18}O_{PDB}$ (‰)	Mineral	Description
HG3 STN 42C	4-1	-45.96	+4.01	Mg calcite	Dense micritic carbonate cement from central region of a lenticular carbonate-cemented fine sandstone-siltstone clast
HG3 STN 42C	4-2	-46.01	+4.01	Mg calcite	
HG3 STN 42C	4-3	-46.16	+4.00	Mg calcite	
HG3 STN 42C	4-4	-45.53	+4.18	Mg calcite	Porous micritic carbonate cement in oxidised (iron oxide stained) porous bored sandstone margin of carbonate-cemented fine sandstone-siltstone clast
HG3 STN 42C	4-4*	-45.77	+3.84	Mg calcite	
HG3 STN 42C	4-5	-44.87	+4.05	Mg calcite	
HG6 STN 31C	5-1	-19.43	+4.36	Dolomite	Very tightly cemented dolomicrite from the dark core of a carbonate-cemented siltstone clast
HG6 STN 31C	5-2	-18.81	+4.54	Dolomite	
HG6 STN 31C	5-3	-19.98	+4.23	Dolomite	Tightly-cemented light-grey dolomicrite surrounding the dark core of the carbonate cemented fine sandstone-siltstone clast
HG6 STN 31C	5-4	-18.51	+4.33	Dolomite	
HG6 STN 31C	5-5	-23.56	+4.33	Dolomite	Very micro-porous micritic dolomite matrix from the oxidised and iron oxyhydroxide-stained, bored and burrowed outer margins of the carbonate-cemented fine sandstone- siltstone clast
HG6 STN 31C	5-5*	-24.02	+4.66	Dolomite	
HG8 STN 31B	6-1	-42.69	+3.28	Mg calcite	Light grey dense micritic cement from the centre of a lenticular carbonate-cemented clast
HG8 STN 31B	6-2	-42.05	+3.47	Mg calcite	
HG8 STN 31B	6-3	-43.68	+3.40	Mg calcite	Buff-coloured porous micritic cement from the partially oxidised rim of a lenticular carbonated-cemented clast
HG8 STN 31B	6-4	-41.27	+3.30	Mg calcite	
HG8 STN 31B	6-5	-50.34	+3.24	Mg calcite	Dark grey micro- porous micritic cement from unoxidised rim of a lenticular carbonated-cemented clast
HG8 STN 31B	6-5*	-50.29	+3.44	Mg calcite	

Note: * replicate analysis

Table 13 (continued). Stable isotope analyses ($\delta^{13}C$ and $\delta^{18}O$) for micro-sampled carbonate components from the MDAC samples (small carbonate analysis method)

Sample	**Sub-sample**	**$\delta^{13}C_{PDB}$ (‰)**	**$\delta^{18}O_{PDB}$ (‰)**	**Mineral**	**Description**
HG8 STN 37B	7-1	-41.05	+3.57	Mg calcite	Micro-porous micritic cement within weakly oxidised bored rim of carbonate-cemented clast
HG8 STN 37B	7-2	-42.57	+3.57	Mg calcite	
HG8 STN 37B	7-3	-43.24	+3.76	Mg calcite	Dense micritic cement in buff-coloured iron oxyhydroxide-stained core of carbonate-cemented clast
HG8 STN 37B	7-4	-44.85	+3.80	Mg calcite	Dense micritic cement in light grey unoxidised rim of carbonate-cemented clast
HG8 STN 37B	7-5	-46.06	+3.88	Mg calcite	
HG8 STN 37B	7-6	-43.99	+3.77	Mg calcite	Dense micritic cement in iron oxyhydroxide-stained core of carbonate-cemented clast
HG8 STN 37C	8-1	-46.65	+3.77	Mg calcite	Dense micritic cement in weakly-oxidised rim of carbonate-cemented clast
HG8 STN 37C	8-2	-46.40	+3.48	Mg calcite	
HG8 STN 37C	8-3	-46.41	+3.65	Mg calcite	Dense micritic cement from central region of carbonate-cemented clast
HG8 STN 37C	8-4	-46.45	+3.55	Mg calcite	
HG9 STN 30A	9-1	-42.22	+4.17	Mg calcite	Dense micritic cement from central region of carbonate-cemented clast
HG9 STN 30A	9-2	-42.65	+4.45	Mg calcite	
HG9 STN 30A	9-3	-42.31	+4.15	Mg calcite	
HG9 STN 30A	9-4	-43.43	+4.18	Mg calcite	Micritic cement from oxidised and iron oxyhydroxide stained rim of carbonate-cemented clast
HG9 STN 30A	9-5	-44.67	+4.09	Mg calcite	

Note: * replicate analysis

Table 13 (continued). Stable isotope analyses ($\delta^{13}C$ and $\delta^{18}O$) for micro-sampled carbonate components from the MDAC samples (small carbonate analysis method)

Sample	Sub-sample	$\delta^{13}C_{PDB}$ (‰)	$\delta^{18}O_{PDB}$ (‰)	Mineral	Description
HG10 STN 29A	10-1	-32.96	+4.54	Dolomite	Dense dolomicrite cement from irregular light-grey non-porous patches of carbonate-cemented clast
HG10 STN 29A	10-2	-32.31	+4.34	Dolomite	
HG10 STN 29A	10-3	-27.76	+4.25	Dolomite	Dolomicritic cement from irregular porous and weakly iron oxyhydroxide-stained layers of silty sediment within carbonate-cemented clast
HG10 STN 29A	10-3*	-27.87	+4.23	Dolomite	
HG10 STN 29A	10-4	-31.21	+3.91	Dolomite	
HG10 STN 29A	10-5	-31.42	+4.08	Dolomite	
HG10 STN 29B	11-1	-22.63	+4.15	Dolomite	Dolomicrite cement from oxidised and strongly iron oxyhydroxide-stained margins of carbonate-cemented clast
HG10 STN 29B	11-2	-18.76	+3.93	Dolomite	
HG10 STN 29B	11-2*	-18.87	+3.79	Dolomite	
HG10 STN 29B	11-3	-22.57	+4.39	Dolomite	
HG10 STN 29B	11-3*	-22.62	+4.62	Dolomite	
HG10 STN 29B	11-4	-18.89	+4.25	Dolomite	Dense dolomicrite cement from light-grey, unoxidised central part of carbonate-cemented clast.
HG10 STN 29B	11-5	FAIL	FAIL	Dolomite	

Note: * replicate analysis

Table 14. Comparison of stable isotope analyses ($\delta^{13}C$ and $\delta^{18}O$) for selected micro-sampled dolomite components from the MDAC samples by the classical and small carbonate sample analysis methods

. Sample	Sub-sample	Mineral	Small carbonate sample method			Classical method	
			$\delta^{13}C_{PDB}$ (‰)	$\delta^{18}O_{PDB}$ (‰)		$\delta^{13}C_{PDB}$ (‰)	$\delta^{18}O_{PDB}$ (‰)
HG6 STN 31C	5-1	Dolomite	-19.43	+4.36		-18.86	+5.74
HG6 STN 31C	5-2	Dolomite	-18.81	+4.54		-20.50	+4.18
HG6 STN 31C	5-3	Dolomite	-19.98	+4.23		-21.38	+3.69
HG6 STN 31C	5-4	Dolomite	-18.51	+4.33		-19.47	+4.38
HG6 STN 31C	5-5	Dolomite	-23.56	+4.33		-24.70	+3.83
HG10 STN 29A	11-1	Dolomite	-32.96	+4.54		-35.03	+4.18
HG10 STN 29A	11-2	Dolomite	-32.31	+4.34		-33.31	+4.39
HG10 STN 29A	11-3	Dolomite	-27.76	+4.25		-28.37	+3.73
HG10 STN 29A	11-4	Dolomite	-31.21	+3.91		-31.52	+3.50
HG10 STN 29A	11-5	Dolomite	-31.42	+4.08		-32.36	+4.11

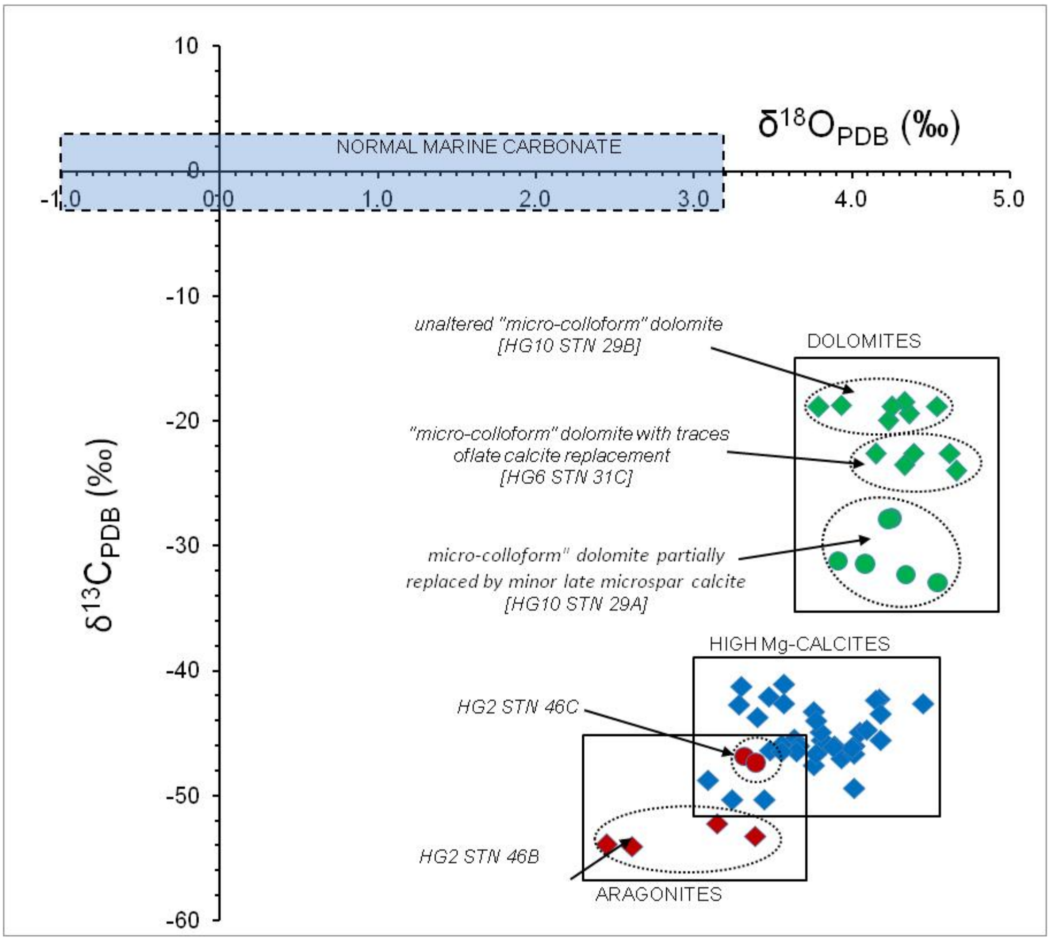

Figure 76. Cross-plot of $\delta^{13}C$ and $\delta^{18}O$ illustrating the variation in stable isotopic composition for the MDAC samples from the Braemar Pockmark area, northern North Sea.

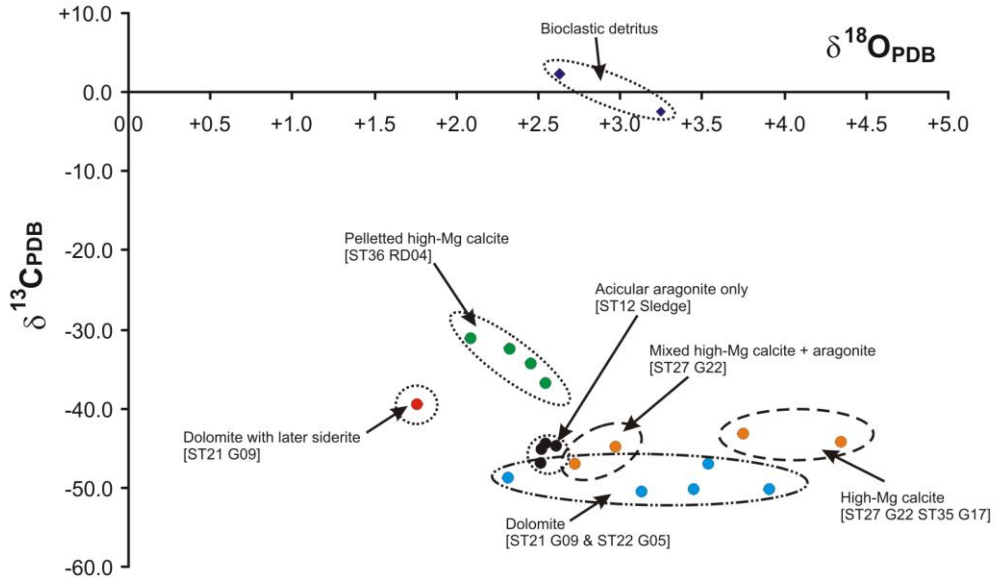

Figure 77. Cross-plot of $\delta^{13}C$ and $\delta^{18}O$ illustrating the variation in stable isotopic composition for MDAC samples from the Mid Irish Sea (Milodowski et al., 2009).

4.2 CARBON ISOTOPE COMPOSITION

The carbon isotopic composition of diagenetic cements varies significantly depending on the process producing the carbonate/bicarbonate ions in the porewater from the breakdown of organic matter. Negative $\delta^{13}C$ values, typically between 0 to -20 ‰ (relative to PDB), are generated by the bacterial reduction of iron, manganese and sulphate (Claypool and Kaplan, 1974; Coleman, 1985; Mozley and Burns, 1993). More positive $\delta^{13}C$ values are produced during methanogenesis with deeper burial below the zone of bacterial reduction (Claypool and Kaplan, 1974; Coleman, 1985; Mozley and Burns, 1993). Carbonates with $\delta^{13}C$ values lighter than -25‰ (relative to PDB) are characteristic of sediments where methane oxidation has produced CO_2 depleted in ^{13}C (Pirrie and Marshall, 1991; Mozley and Burns, 1993).

All of the aragonite and magnesian calcite cements display highly depleted ^{13}C composition, with $\delta^{13}C_{PDB}$ values between -41 to -55 ‰ (Table 13 and Figure 76). These values are strongly indicate of carbonate cements precipitated as a result of methane oxidation, and are characteristic of MDAC deposits described previously from other areas (Jensen et al., 1992; Sakai et al., 1992; Bohrmann et al., 1998; Peckmann et al., 2001; Muralidhar et al., 2006; Milodowski et al., 2009 and Figure 77) therefore lend strong support to the hypothesis that the aragonite- and magnesian calcite-cemented sandstones and siltstones recovered from the Braemar Pockmark area of the North Sea also represent MDAC.

In contrast to the aragonite and high-magnesian calcite cements, the dolomite cements (samples HG10 STN29A, HG10 STN29B and HG6 STN 31C) are characterised by $\delta^{13}C_{PDB}$ values between -33.0 and -18.0 $‰_{PDB}$. The unaltered dolomite (sample HG10 STN29B) has the heaviest $\delta^{13}C_{PDB}$ values (>-22.7 $‰_{PDB}$), which are closer to that expected for carbonates produced during bacterial reduction processes (Claypool and Kaplan, 1974; Coleman, 1985; Mozley and Burns, 1993). The dolomite cements in these samples are all very closely associated with the preservation of cellular fabrics that closely resemble mineralised bacterial structures, and syngenetic formation of early diagenetic framboidal pyrite (Section 3). Framboidal pyrite is characteristic of low-temperature sulphide formation (Berner, 1969; 1980; Rickard, 1970; 1975; Sweeney & Kaplan, 1973). Sulphate reduction at low temperatures (i.e. below 100 to 140 ˚C) implies a bacterially-mediated process, since abiotic sulphide reduction is kinetically unfavourable (Machel, 1987 and references therein). This typically results in the formation of early diagenetic pyrite framboids within sediments (Berner, 1969). The presence of pyrite framboids within these Pockmark Braemar carbonate-cemented sediments is consistent with an early diagenetic origin. The framboidal pyrite most probably formed by microbial iron and sulphate reduction in near-surface sediment porewaters (i.e. the sulphate reduction zone) where a supply of sulphate from the overlying seawater could readily diffuse into the sediment to be reduced by bacterial processes (Berner, 1980). The stable isotope data coupled with the petrological observations from the dolomite-cemented Braemar Pockmark are therefore consistent with the early diagenetic dolomite precipitation within the sulphide-reduction zone close to the sediment surface, or with a significant input of carbonate/bicarbonate ions produced from bacterial sulphide reduction.

4.3 OXYGEN ISOTOPE COMPOSITION

The temperature at which the carbonate cement precipitated can be estimated from the temperature-dependant equilibrium oxygen isotope fractionation ($\delta^{18}O$) between the carbonate mineral and the water from which it has precipitated, assuming the carbonate is in equilibrium with the water. The calcite-water system is the best understood carbonate mineral system and is most widely used in palaeotemperature studies, and there are a number of published empirical palaeotemperature equations for the equilibrium precipitation of calcite from solution (Leng and Marshall, 2004). Two such equations were used in this study, to estimate the temperature for the formation of the MDAC from the Braemar Pockmark area of the North Sea:

Equation 1: Hays and Grossman's (1991) equation based on their revised 'fit' of O'Neil et al.'s (1969) experimental data. This gives very similar results to most other equations.

$$T = 15.7 - 4.36(c\text{-}w) + 0.12(c\text{-}w)^2$$

Equation 2: Leng and Marshall's (2004) expression of Kim and O'Neil's (1997) more recent equation. This gives slightly lower calculated palaeotemperatures than Equation 1 and other published equations.

$$T = 13.8 - 4.58(c\text{-}w) + 0.08\,(c\text{-}w)^2$$

In both cases, T is the temperature (°C), c is $\delta^{18}O$ of calcite relative to the Pee Dee Belemnite (PDB) international standard, and w is the $\delta^{18}O$ of the water relative to the Standard Mean Ocean Water (SMOW) international standard. The calculations made in this report have assumed the oxygen isotope composition of the seawater on the bed of the North Sea to be the same as SMOW (i.e. $\delta^{18}O = 0‰$).

These equations are based on the empirical relationship between temperature, the isotopic composition of calcite, and the composition of the water from which it formed. Aragonite and magnesium calcites precipitated at equilibrium are generally isotopically heavier than pure or low-magnesium calcites. Review of published literature indicates that aragonite $\delta^{18}O$ values are typically around +0.6‰ higher than the equivalent calcite (Leng and Marshall, 2004). The $\delta^{18}O$ values of magnesium calcites typically increase by 0.06‰ per mol% of $MgCO_3$ in solid-solution in the calcite (Tarutani et al., 1969, cited in Leng and Marshall, 2004). These offsets in $\delta^{18}O$ appear to be independent of temperature (cf. Kim and O'Neil, 1997). Dolomite similarly tends to be isotopically heavier than calcite precipitated under the same environment. Land (1980), also cited by Leng and Marshall (2004), indicates that $\delta^{18}O$ values for dolomite are generally around +3‰ heavier than the equivalent calcite mineralisation, at normal surface temperatures.

The isotopic composition of carbonates that should precipitate in equilibrium with the seawater, at present-day seabed temperatures in the North Sea, was also calculated using quadratic solution of Equation 1, for comparison to the MDAC carbonates (taking into account the offset in $\delta^{18}O$ values between that for pure calcite and for aragonite, high-magnesium calcite and dolomite, discussed above). For these calculations, the present-day seabed temperature within the area of study was estimated to be between 6 and 10°C (Knight et al., 1993; Defra, 2010).

Based on these calculations, the $\delta^{18}O$ of the aragonite cements predicted to be in equilibrium with seawater under present-day northern North Sea sea-bed temperatures (6-10 °C) is estimated to be between 2 and 3 $‰_{PDB}$. This is broadly similar to the observed $\delta^{18}O$ composition of the aragonite cements in the carbonate cemented sediments from the Braemar Pockmark area (Table 13 and Figure 76), although some of the observed aragonite $\delta^{18}O$ values are slightly heavier than predicted, suggesting that they may have formed under slightly cooler conditions. However, the high-magnesium calcite cements (Table 13 and Figure 76) appear to be significantly heavier that that predicted to be in equilibrium with seawater at the present-day seabed (i.e. $\delta^{18}O$ is predicted to be between 1.4 to 2.4 $‰_{PDB}$ for calcite). Even allowing an increase in $\delta^{18}O$ for high magnesium calcite, these data suggest that carbonate cements have precipitated under significantly colder conditions than present-day (calculations suggest approximately 3 to 10°C colder, depending on which equation (above) is used), or from seawater with a significantly heavier $\delta^{18}O$ than SMOW.

Cooling during glacial episodes increases the mass-dependent fractionation of oxygen isotopes between water and carbonate minerals, resulting in higher $\delta^{18}O$ values of marine carbonates formed during these times. The growth of large continental ice sheets also increases the $\delta^{18}O$ of seawater, because the lighter oxygen isotopes are preferentially enriched and locked-up in snow precipitation that leads to the formation of the ice sheets, and thereby depletes the marine reservoir of ^{16}O (e.g. Schrag et al., 2002; Lisieki and Raymo, 2005). Both colder marine temperatures and ^{18}O-enriched marine water in the North Sea during the last glacial maximum (and earlier glaciations) could therefore have produced the heavy $\delta^{18}O$ observed in the magnesian calcite cements (and to a lesser extent, the aragonite cements) in these MDAC samples from the Braemar Pockmark area.

5 Summary and conclusions

Eleven samples of carbonate-cemented sediment recovered from the seabed in the Braemar Pockmark area of the North Sea have been characterised mineralogically and petrographically, and the stable isotope ($\delta^{13}C$ and $\delta^{18}O$) composition of their component carbonate cements has been analysed to describe the nature and evaluate the origin of the carbonate cement.

5.1 TYPES OF CARBONATE-CEMENTED SEDIMENT

The carbonate-cemented sediments can be categorised into 3 principal end-member lithologies:

Aragonite-dominated cements

This is exemplified by samples HG2 STN 46B and HG2 STN 46C, which are a sandy sediment cemented by aragonite cements comprising:

1) Early isopachous grain-coating aragonite fringes coating detrital grains
2) Precipitation of “clots”, or framboidal microbotryoidal aggregates of micritic of microcrystalline aragonite. These may coalesce to form a locally dense micritic ‘crystal mush’ matrix.
3) Coarse acicular aragonite overgrowths on molluscan shell fragments.

The aragonite is strontium-rich with up to 2 mole% $SrCO_3$ in solid-solution.

In both samples the aragonite-cemented rock can be demonstrated to have formed later than the magnesian-calcite-cemented lithologies. The aragonite-cemented sediments rest on eroded earlier magnesian-calcite cemented sandstones or include eroded clasts of magnesian-calcite-cemented sandstone, and also infill borings into magnesian-calcite-cemented sandstone surfaces.

High-magnesium calcite-dominated cements

This is exemplified by samples HG3 STN 42B, HG3 STN 42C, HG8 STN 31B, HG8 STN37Band HG9 STN 30A and included fragments of magnesian-calcite cemented sandstone within HG2 STN 46B and HG2 STN 46C. These rocks display:

1) Early globular, spheroidal aggregates of very fine grained high-magnesium calcite coating detrital grains
2) Precipitation of “clots”, or spheroidal aggregates of micritic or microcrystalline high-magnesium calcite. These micrite aggregates may coalesce to form a locally dense micritic matrix.
3) Well-developed microcellular fabrics, comprising aggregates of magnesian calcite microcrystals typically less much than 1 μm in size that have nucleated around or encrust a central microcavity about 1-2 μm in diameter. These structures very closely resemble fossilised and mineralised bacterial cells described from experimental studies and other environments in the literature (cf. Martill and Wilby, 1994; Wilby and Whyte, 1995). Further support for this origin is provided by the observations that many of these cellular microstructures appear to be preserved in the process of cell division or mytosis (e.g. Figure 43). Denser areas of cementation have formed as these microcellular structures coalesce and become more compacted.

The magnesian calcites typically have a composition ranging from about 10-35 mole % $MgCO_3$ in solid-solution, which is within the range of compositions observed from other MDAC deposits.

Dolomite-dominated cements

This is exemplified by samples HG6 STN 31C, HG10 STN 29A and HG10 STN 29B. The carbonate fabrics are very similar to those encountered in the magnesian-calcite-dominated samples, with:

1) Early grain-coating dolomite fringes formed of microcolloform globules.
2) Well-developed microcellular fabrics, comprising aggregates of dolomite microcrystals typically less much than 1 µm in size that have nucleated around or encrust a central microcavity about 1-2 µm in diameter. These structures very closely resemble fossilised and mineralised bacterial cells described from experimental studies and other environments in the literature (cf. Martill and Wilby, 1994; Wilby and Whyte, 1995). Denser areas of cementation have formed as these microcellular structures coalesce and become more compacted. The fabric is similar to that observed in some of the magnesian-calcite-cemented samples but is better-preserved in the dolomitic rocks. Similar dolomite fabrics have been observed by Milodowski et al. (2009) from MDAC samples studied from the Mid Irish Sea. However, the dolomite-mineralised microcellular structures are generally much better preserved in the Braemar Pockmark samples.

The dolomite is a high-calcium dolomite which contains up to 10 mole% excess $CaCO_3$ relative to ideal stoichiometric dolomite. This may indicate that the dolomite is relatively poorly ordered and/or metastable, and may have precipitated rapidly (Vahrenkamp and Swart, 1994) possibly forming via a “protodolomite” precursor (cf. Deer et al., 1992).

Minor amounts of late-stage calcite replaces both early micritic magnesian calcite and micritic dolomitic in some of the samples. This calcite is much lower in magnesium content than the original magnesian calcite that it replaces. It typically forms fine microspar patches of tightly-interlocking equant anhedral crystal aggregates that replace and overprint the original micrite fabrics. It also occurs as isolated rhombs nucleated within the dolomicrite or micritic magnesian calcite matrix, and as fine crystals lining open pores in some samples.

The recrystallisation of high-magnesian calcite and its partial replacement by lower magnesian calcite, is closely associated with minor late dolomite precipitation, which similarly occurs as isolated rhombs nucleated within the micritic magnesian calcite matrix. The formation of this dolomite was probably promoted by the increased concentration of magnesium ions in the sediment porewater as a result of this replacement process, leading to localised minor dolomitisation of the carbonate sediment.

Petrographic observations also show that the micritic carbonate sediments were being reworked by benthic marine organisms, prior to lithification and then redeposited as sand-grade faecal pellets composed of micrite. Much of the evidence of burrowing preserved in these carbonate-cemented was probably associated with this process. The petrographic evidence suggests that these micritic sediments were produced by and associated with abundant bacteria, which probably provided the base of a food chain for larger, higher-order prior to lithification of these sediments.

5.2 ORIGIN OF THE CARBONATE-CEMENTED SEDIMENTS

All of the aragonite and magnesian calcite cements display highly depleted ^{13}C composition, with $\delta^{13}C_{PDB}$ values between -41 to -55 ‰. This is consistent with a diagenetic origin in which carbonate precipitation is related to methane oxidation , and is characteristic of MDAC deposits described previously from other areas (Jensen et al., 1992; Sakai et al., 1992; Bohrmann et al., 1998; Peckmann et al., 2001; Muralidhar et al., 2006; Milodowski et al., 2009). Therefore, this provides strong evidence to the hypothesis that the aragonite- and magnesian calcite-cemented sandstones and siltstones recovered from the Braemar Pockmark area of the North Sea represent MDAC.

In contrast to the aragonite and high-magnesian calcite cements, the dolomite cements (samples HG10 STN29A, HG10 STN29B and HG6 STN 31C) are characterised by $\delta^{13}C_{PDB}$ values between -33.0 and -18.0 ‰$_{PDB}$. The unaltered dolomite (sample HG10 STN29B) has the heaviest $\delta^{13}C_{PDB}$ values (>-22.7 ‰$_{PDB}$), which are closer to that expected for carbonates produced during bacterial reduction processes (Claypool and Kaplan, 1974; Coleman, 1985; Mozley and Burns, 1993). The dolomite cements in these samples are all very closely associated with the preservation of cellular fabrics that closely resemble mineralised bacterial structures, and with the syngenetic formation of early diagenetic framboidal pyrite. Framboidal pyrite most probably formed by microbial iron and sulphate reduction in near-surface sediment porewaters (i.e. the sulphate reduction zone) where a supply of sulphate from the overlying seawater could readily diffuse into the sediment to be reduced by bacterial processes (Berner, 1980). The stable isotope data coupled with the petrological observations from the dolomite-cemented Braemar Pockmark are therefore consistent with the early diagenetic dolomite precipitation within the sulphide-reduction zone close to the sediment surface, or with a significant input of carbonate/bicarbonate ions produced from bacterial sulphide reduction.

The observed $\delta^{18}O$ signature of the aragonite-cemented MDAC materials carbonate cements is broadly similar to the $\delta^{18}O$ of the aragonite cements predicted to be in equilibrium with seawater under present-day northern North Sea sea-bed temperatures (6-10 °C). Although some of the observed aragonite $\delta^{18}O$ values are slightly heavier than predicted, suggesting that they may have formed under slightly cooler conditions

In contrast to the aragonite MDAC cements, the high-magnesium calcite MDAC cements are significantly heavier that that predicted to be in equilibrium with seawater at the present-day seabed (i.e. $\delta^{18}O$ is predicted to be between 1.4 to 2.4 ‰$_{PDB}$ for calcite). Even allowing an increase in $\delta^{18}O$ for high magnesium calcite, these data suggest that carbonate cements have precipitated under significantly colder conditions than present-day (calculations suggest approximately 3 to 10°C colder), or from seawater with a significantly heavier $\delta^{18}O$ than SMOW. Both colder marine temperatures and ^{18}O-enriched marine water in the North Sea during the last glacial maximum could therefore have produced the heavy $\delta^{18}O$ observed in the magnesian calcite cements (and to a lesser extent, the aragonite cements) in these MDAC samples from the Braemar Pockmark area.

The more complex MDAC samples represented by HG2 STN 46B and HG2 STN 46C, in which magnesian-calcite cemented MDAC is superceded by aragonite –cemented MDAC indicates that in area where these samples formed, there have been at least two distinct phases of MDAC formation: (i) an earlier phase during cooler conditions (possibly during the last glacial maximum) when high-magnesian calcite was precipitated, and; (ii) a later phase of MDAC formation under warmer conditions closer to present-day marine temperatures, when aragonite was precipitated. These two phases were, separated by a hiatus, during which there was erosion of the earlier-formed magnesian-calcite MDAC deposit.

The dolomitic carbonate cements are similarly heavier than expected with regard to $\delta^{18}O$ for precipitates from present day seawater. These too could have been formed during cooler marine temperatures than the present-day. However, the lighter $\delta^{13}C$ values suggests that these formed with a significant input of carbonate derived from the bacterial iron and sulphate reduction in the sediment, rather than dominantly from bacterial methane oxidation.

5.3 IN-SITU OR REWORKED ORIGINS

Virtually all of the samples carbonate-cemented sediment examined in this study display abraded and well-worn and rounded surfaces. This indicates that most of the pebble- to cobble-sized fragments are clasts of re-worked carbonate-cemented sediment that have eroded from their original sediment source. Therefore, they do represent in situ carbonate-cemented rocks. Observations show that the clasts have also been exposed to oxidising conditions on the sea floor during this process.

References

Andrews, I. J., Long, D., Richards, P. C, Thomson, A. R., Brown, S., Chesher, J. A. and McCormac, M. 1990: The Geology of the Moray Firth. *United Kingdom Offshore Regional Report, British Geological* Survey

Berner, R.A. 1969. The synthesis of framboidal pyrite. *Economic Geology*, **64**, 383-384.

Berner, R.A. 1980. *Early Diagenesis: A Theoretical Approach*. Princeton University Press, Princeton, New Jersey, USA, 241pp.

Bohrmann, G., Greinert, J., Suess, E. and Torres, M. 1998. Authigenic carbonates from the Cascadia subduction zone and their relation to gas hydrate stability. *Geology*, **26**, 647-650.

Burke, R.A., Jn. 1992. Factors responsible for variations in stable isotope ratios of microbial methane from shallow aquatic sediments. In: Vially, R. (Editor) *Bacterial Gas*. Éditions Technip, Paris, France, 47-62.

Claypool, G.E. and Kaplan, I.R. 1974. The origin and distribution of methane in marine sediments. In: Kaplan, I.R. (editor) *Natural Gasesin Marine Sediments*, Plenum Press, New York, 99-140

Coleman, M.L. 1985. Geochemistry of diagenetic non-silicate minerals: kinetic considerations. In: Eglinton, G., Curtis, C.D. McKenzie, D.P. and Murchison, D.G. (editors). *Geochemistry of Buried Sediments*. The Royal Society, London, 39-54

Croker , P.F., Kozachenko, M. and Wheeler, A.J. 2005. Gas-related seabed structures in the Western Irish Sea (IRL-SEA6). *Technical Report of the Petroleum Affairs Division of Ireland, produced for Strategic Environmental Assessment – SEA6*

Dando, P.R., Austen, M.C., Burke, R.A., Kendall, M.A., Kennicutt II, M.C., Judd, A.G., Moore, D.C., O'Hara, S.C.M., Schmaljohann, R. and Southward, A.J. 1991. Ecology of a North Sea pockmark with active methane seep. *Marine Ecology Progress Series*, **70**, 49-63.

Dando, P.R. 2001. A review of pockmarks in the UK part of the North Sea, with particular respect to their biology. *DTI Strategic Environmental Assessment – SEA2, Technical Report*, **TR-001**, 21pp.

Deer, W.A., Howie, R.A. and Zussman, J. 1962a. *Rock Forming Minerals. Volume 5: Non-Silicates*. Longmans, London.

Deer, W.A., Howie, R.A. and Zussman, J. 1992b. *An Introduction to the Rock Forming Minerals (2nd edition)*. Pearson Education Limited, Harlow, London.

Defra. 2010. Charting *Progress 2: An assessment of the state of UK seas. Feeder Report: Ocean Processes*. UK Marine Monitoring and Assessment Strategy (UKMMAS) Community, Defra, United Kingdom. http://chartingprogress.defra.gov.uk.

Forsberg, C.F., Planke, S., Tjelta, T.I., Svano, G., Strout, J.M. and Svensen, H. 2007. Formation of pockmarks in the Norwegian Channel. *Proceedings of the 6th International Offshore Site Investigation and Geotechnics Conference: Confronting New Challenges and Sharing Knowledge, 11-12 September 2007, London, UK*, 221-230.

Goldstein, J.I., Newbury, D.E., Echlin, P., Joy, D.C., Fiori, C. and Lifshin, E. 1981. *Scanning Electron Microscopy and X-Ray Microanalysis*. Plenum Press, New York.

Hays, P.D. and Grossman, E.L. 1991. Oxygen isotopes in meteoric calcite cements as indicators of continental paleoclimate. *Geology*, **19**, 441-444.

Hovland, M. and Irwin, H. 1989: Habitat of methanogenic carbonate cemented sediments in the North Sea. *Abstracts of the Bacterial Gas Conference Milan, September, 25-26 September 1989*.

Hovland, M. and Sommerville, J.H. 1985. Characteristics of two natural gas seepages in the North Sea. *Marine and Petroleum Geology*, **2**, 319-326.

Hovland, M. and Talbot, M.R. 1987. Hydrocarbon seeps in northern marine waters; their occurrence and effects. *Journal of Sedimentary Research*, **57**,

Hovland, M. Judd, A. G. 1988. *Seabed Pockmarks and Seepages*. Graham and Trotman Ltd, London.

Jansen, J. H F. 1976. Late Pleistocene and Holocene history of the northern North Sea, based on acoustic reflection records. Netherlands. Journal of Sea Resources. **10**, 1-43

Jensen, P., Aagaard, I., Burke Jr., R.A., Dando, P.R., Jøgensen, N.O., Kuijpers, A., Laier, T., O'Hara, S.C.M. and Schmaljohann, R. 1992. 'Bubbling reefs' in the Kattegat: submarine landscapes of carbonate-cemented rocks support a diverse ecosystem at methane seeps. *Marine Ecology Progress Series*, **83**, 103-112.

JNCC. 2008. *Offshore Special Area of Conservation: Scanner Pockmark SAC Selection Assessment* (Version 4.0),*July 2008*. Joint Nature Conservation Committee (JNCC) Report. http://jncc.defra.gov.uk/pdf/ScannerPockmark_SelectionAssessment_4.0.pdf

JNCC. 2012. *Offshore Special Area of Conservation: BraemarPockmarks. SAC Selection Assessment* (Version 4.1), *9th January 2012*. Joint Nature Conservation Committee (JNCC) Report. http://jncc.defra.gov.uk/pdf/BraemarPockmarks_SelectionAssessment_4.1.pdf

JOHNSON, H., RICHARDS, P.C., LONG, D. AND GRAHAM, C.C. 1993. The geology of the northern North Sea. *United Kingdom Offshore Regional Report, British Geological Survey*. HMSO, 110pp.

JORGENSEN, N.O. 1992. Methane derived carbonate cementation of Holocene marine sediments from Kattegat, Denmark. *Continental Shelf Research*, **12**, 1209-1218.

JUDD, A., LONG, D. AND SANKEY, M. 1994. Pockmark formation and activity, U.K. block 15/25, North Sea. *Bulletin of the Geological Society of Denmark*, **41**, 34-49.

JUDD, A.G. 2001. Pockmarks in the UK sector of the North Sea. *Technical Report produced for Strategic Environmental Assessment SEA2*. Department of Trade and Industry, UK.

JUDD, A.G. 2005. The distribution and extent of methane-derived authigenic carbonate. *DTI Strategic Environmental Assessment, Area 6 (SEA6)*. United Kingdom Department of Trade and Industry (Dti)

KIM, S.T. AND O'NEIL, J.R., 1997. Equilibrium and non-equilibrium oxygen isotope effects in synthetic carbonates. *Geochimica et Cosmochimica Acta*, **61**, 3461–3475.

KNIGHT, P.J., WILKINSON, M. AND GLORIOSO, P. 1993. Current profile and sea-bed pressure and temperature records from the northern North Sea Challenger cruises 84 and 85:September 1991 – November 1991. *Proudman Oceanic Laboratory Report*, **28 (1993)**, 417pp.

LAND, L.S., 1980. The isotopic and trace element geochemistry of dolomite: the state of the art. In: ZENGER, D.H., ET AL. (Editor.), Concepts and Models of Dolomitisation, Society of Economic *Paleontologists and Mineralogists (SEPM), Special Publication*, **28**, 87–110, Tulsa, Oklahoma.

LONG, D. 1986. *Seabed Sediments, Fladen Sheet 58°N 00°.* British Geological Survey, Edinburgh.

LENG, M.J. AND MARSHALL, J.D. 2004. Palaeoclimate interpretation of stable isotope data from lake sediment archives. *Quaternary Science Reviews*, **23**, 811-831.

LIESKI, L.E. AND RAYMO, M.E. 2005. A Pliocene-Pleistocene stack of 57 globally distributed benthic $\delta^{18}O$ records. *Paleooceanography*, **20**, PA1003, 17pp, .doi:10.1029/2004PA001071

MACKENZIE, F.T., BISCHOFF, W.D.,BISHOP, F.C., LOIJENS, /M., SCHOONMAKER, J. AND WOLLAST, R. 1983. Chapter 4. Magnesian calcites: low-temperature occurrence, solubility and solid-solution behaviour. In/: REEDER, R.J. (editor). *Carbonates: Mineralogy and Chemistry. Reviews in Mineralogy,* Volume 11, Mineralogical Society of America, Virginia, pp. 97-144.

MACHEL, H.G. 1987. Some aspects of diagenetic sulphate-hydrocarbon redox reactions. In: Marshall, J.D. (editor) *Diagenesis of Sedimentary Sequences.* Geological Society of London, Special Publication, **36**, 15-28.

MARSHALL, J.D. 1988. *Cathodoluminescence of Geological Materials*. Allen & Unwin Inc., USA.

MARTILL, D.M. AND WILBY, P.R. 1994. Lithified prokaryotes associated with fossil soft tissies from the Santana Formation (cretaceous) of Brazil. *Kaupia*. **4**, 71-77.

MCCREA, J.M. 1950. On the isotopic chemistry of carbonates and a paleotemperature scale. *Journal of Chemical Physics*, **18**, 849-857.

MILODOWSKI, A.E. TULLBORG, E.-L., BUIL, B., GÓMEZ, P., TURRERO, M.-J., HASZELDINE, S., ENGLAND, G., GILLESPIE, M.R., TORRES, T., ORTIZ, J.E., ZACHARIÁŠ, SILAR, J., CHVÁTAL, M., STRNAD, L., ŠEBEK, O. BOUCH, J.E., CHENERY, S.R., CHENERY, C., SHEPHERD, T.J. AND MCKERVEY, J.A. 2005. Application of Mineralogical, Petrological and Geochemical tools for Evaluating the Palaeohydrogeological Evolution of the PADAMOT Study Sites. PADAMOT PROJECT - EU FP5 CONTRACT NO. FIKW-CT2001-20129. *PADAMOT Project Technical Report, WP2*. 228pp +digital appendices.

MILODOWSKI, A.E. LACINSKA, A. AND SLOANE, H. 2009. Petrography and stable isotope geochemistry of samples of methane-derived authigenic carbonates (MDAC) from the Mid Irish Sea. *British Geological Survey, Commissioned Report,* **CR/09/051**, 62pp.

MOZLEY, P. AND BURNS, S.J. 1993. Oxygen and carbon isotope comparison of marine carbonate concretions: an overview. *Journal of Sedimentary Petrology,* **63**, 73-83.

MURALIDHAR, K., MAZUMDAR, A., KARISIDDAIAH, S.M., BOROLE, D.V. AND RAO, B.R. 2006. evidences of methane-derived authigenic carbonates from the sediments of the Krishna-Godavari Basin, eastern continental margin of India. *Current Science,* **91**, 318-323.

O'NEIL, J.R., CLAYTON, R.N. AND MAYEDA, T.K. 1969. Oxygen isotope fractionation in divalent metal carbonates. Journal of *Chemical Physics*, **51**, 5547-5558.

OXFORD INSTRUMENTS ANALYTICAL LIMITED. 2009. INCA Microanalysis Suite Issue 18d + SP3, INCA Suite version 4.15. Copyright © Oxford Instruments Analytical Limited, High Wycombe, United Kingdom.

PECKMANN, J., REIMER, A., LUTH, U., HANSEN, B.T., HEINICKE, C., HOEFS, J. AND REITNER, J. 2001. Methane-derived carbonates and authigenic pyrite from the northwestern Black Sea. *Marine Geology*, **177**, 129-150.

PIRRIE, D AND MARSHALL, J.D. 1991. Field relationships and stable isotope geochemistry of concretions from James Ross Island, Antarctica. *Sedimentary Geology*, **71**, 137-150.

RICKARD, D.T. 1970. The origin of framboids. *Lithos*, **3**, 269-293.

RICKARD, D.T. 1975. Kinetics and mechanism of pyrite formation at low temperatures. *American Journal of Science*, **274**, 636-652.

ROSENBAUM, J. AND SHEPPARD, S.M.F. 1986. An isotopic study of siderites, dolomites and ankerites at high-temperatures. *Geochimica et Cosmochimica Acta*, **50**, 1147-1150.

SAKAI, H., GAMO, T., OGAWA, Y. AND BOULEGUE, J. 1992. Stable isotope ratios and origins of the carbonates associated with cold seepage at the eastern Nankai Trough: fluids in convergent margins. *Earth and Planetary Science Letters*, **3-4**, 391-404.

SCHRAG, D.P., ADKINS, J.F., MCINTYRE, K., ALEXANDER, J.L., HODELL, D.A., CHARLES, C.D. AND MCMANUS, J.F. 2002. The oxygen isotopic composition of seawater during the Last Glacial Maximum. *Quaternary Science Reviews*, **21**, 331–342.

SEJRUP, H.P., AASETH, I. AND HAFLIDASON, H. 1991. The Quaternary succession in the northern North Sea. Marine Geoloogy, **101**, 103-111.

SOLHEIM, A. AND ELVERHØI, A., 1993. Gas-related seafloor craters in the Barents Sea. *Geo-Marine Letters*, **13**, 235-243.

SWEENEY, R.E. AND KAPLAN, I.R. 1973. Pyrite framboid formation: laboratory synthesis and marine sediments. *Economic Geology*, **68**, 618-634.

TARUTANI, T., CLAYTON, R.N., AND MAYEDA, T. 1969. The effect of polymorphism and magnesium substitution on oxygen isotope fractionation between calcium carbonate and water. *Geochimica et Cosmochimica Acta*, **33**, 987–996.

VAHRENKAMP, V.C. AND SWART, P.K. 1994. Late Cenozoic dolomites of the Bahamas: metastable analogues for the genesis of ancient platform dolomites. *Special Publication of the International Association of Sedimentologists*, **21**, 133-153.

WILBY, P.R. AND WHYTE, M.A. 1995. Phosphatized soft tissues in bivalves from the Portland Roach of Dorset (Upper Jurassic). *Geological Magazine*, **132**, 117-120.

British Geological Survey
NATURAL ENVIRONMENT RESEARCH COUNCIL

British Geological Survey
Environmental Science Centre
Keyworth
Nottingham
United Kingdom
NG12 5GG

Tel +44 (0)115 936 3100
Email enquiries@bgs.ac.uk

REPORT APPROVAL FORM

Report title and authors

Petrography and stable isotope study of methane-derived authigenic carbonates (MDAC) from the Braemar Pockmark Area, North Sea.

A.E. Milodowski and H. Sloane

Client name and address

Cefas - Lowestoft Laboratory
Pakefield Road
Lowestoft
Suffolk
NR33 0HT
United Kingdom

Version control	**Final v.1.0**
BGS Report No.	**CR/13/078**
Client contract	**Cefas PO. 20017984**
Ref. BGS project code	**NEE8679**
Classification	**Commercial-in-confidence**

Version	Status	Prepared by	Checked by	Approved by	Date
1.0	**Final**		S.J.K		**14 Oct. 2013**

BGS/RAFv3.0; Jan 2013